



DEPARTMENT OF PHYSICS

TFY4510 - PHYSICS, SPECIALIZATION PROJECT

Proximity Effects and RKKY Interactions in *s*-wave and *p*-wave Superconducting Nanostructures

Author: Emil Spasov
Supervisors: Jabir Ali Ouassou
Jacob Linder

December, 2025

Abstract

Unconventional superconductors hold considerable potential for next-generation technologies. In particular, p -wave spin-triplet superconductors can host distinctive phenomena such as topological edge states and spin-polarized supercurrents, making them attractive for quantum and spintronic devices. However, a major practical limitation is that p -wave superconducting phases typically emerge only at very low critical temperatures T_c , which makes their experimental realization and technological integration challenging. To address this, we consider layered nanostructures constructed from materials with different properties. Such heterostructures provide a versatile platform in which different pairing symmetries, energy scales, and interfacial couplings can be engineered to realize phases and properties not available in bulk materials. The goal of the present thesis is to lay the theoretical and numerical foundation for a forthcoming master's thesis, in which we will investigate proximity systems with the aim of stabilizing the exotic triplet state at relatively high temperatures without polluting the p -wave superconductor with other symmetries.

We begin with a comprehensive review of the tight-binding model, the extended Hubbard model, and the fundamental mechanisms underlying ferromagnetism and superconductivity, and we implement these models numerically. Next, we introduce the Bogoliubov–de Gennes formalism, along with the corresponding self-consistent equations applicable to both conventional and unconventional superconducting systems. Focusing on on-site singlet pairing, we solve these equations iteratively to determine the superconducting band gap and critical temperature. We then explore the interplay between superconductivity and magnetism; in particular, we investigate magnetic frustration and the Ruderman–Kittel–Kasuya–Yosida (RKKY) interaction in a triangular lattice with symmetrically placed spins. To the best of our knowledge, this specific frustrated RKKY configuration has not been investigated previously and therefore constitutes a novel result. We finish by introducing the concept of proximity effects with some common examples of such systems, such as SN/SF junctions and Josephson junctions.

Preface

This thesis was submitted as a specialization project in condensed matter physics at the Norwegian University of Science and Technology under joint supervision of Assoc. Prof. Jabir Ali Ouassou and Prof. Jacob Linder. It is a part of a 5 year integrated Master's program in Applied Physics and Mathematics, and amounts to 15 ECTS credits in the 9th semester of the program.

Contents

1	Introduction	1
1.1	Superconductivity	1
1.2	Superconductivity and magnetism	1
1.3	Proximity systems	2
1.4	Objective and structure	2
2	Preliminaries	4
2.1	Mathematical notation	4
2.2	Natural units	4
2.3	The second quantization formalism	4
2.4	Representation of operators in second quantization	5
2.5	Nambu space	6
3	Tight-Binding Model and Lattice Structure	8
3.1	Wannier orbitals and atomic lattices	8
3.2	Tight-binding Hamiltonian for a metal	8
3.3	Diagonalizing the tight-binding Hamiltonian	9
3.4	Calculating physical observables	9
3.5	The extended Hubbard model	11
4	Ferromagnetism	13
4.1	Quantum exchange	13
4.2	The single-band Hubbard model	15
4.3	Magnetic phases and the Stoner criterion	16
4.4	Frustrated magnetism	17
5	Superconductivity	19
5.1	Introduction to the Bardeen–Cooper–Schrieffer (BCS) theory	19
5.2	Critical temperature T_c and the energy gap Δ in the BCS theory	22
5.3	Mean-field extended Hubbard model of superconductivity	23
5.4	Pairing symmetries and superconducting gap beyond on-site s -wave	24
5.5	Bogoliubov–de Gennes (BdG) formalism	26
5.6	Self-consistent solution for on-site s -wave pairing	28
5.7	Bogoliubov–de Gennes equations in the extended Hubbard model	29
5.8	Concluding remarks	32
6	Ruderman–Kittel–Kasuya–Yosida (RKKY) Interaction	33
6.1	Formalism of the RKKY interaction	33
6.2	Spin-spin interactions	34
6.3	Geometric frustration on a superconducting triangular lattice	35
6.4	Concluding remarks	39
7	Proximity Effect	41
7.1	Proximity effect in SN junctions	41
7.2	Josephson junctions (SNS/SIS)	42
7.3	Proximity effect in SF junctions	44
7.4	Concluding remarks	46
8	Conclusions and Outlook	48
A	Extended Hubbard Model in Mixed Real–Momentum Space	51
B	Bisection Algorithm for Critical Parameter Search	53
	Bibliography	54

1 Introduction

1.1 Superconductivity

Superconductivity is an exotic state of matter. It was first discovered in 1911 by Heike Kamerlingh Onnes, who observed that mercury's electrical resistance drops abruptly to (practically) zero at $T \approx 4.2\text{K}$ [1]. Through the 1910s–1930s, other elemental superconductors (Pb, Sn) were found [2], along with the Meissner–Ochsenfeld effect in 1933 [3], which showed superconductivity is not just zero resistance but a distinct thermodynamic phase expelling magnetic flux. A microscopic theory was missing until 1957, when Bardeen, Cooper, and Schrieffer proposed the BCS theory: electrons form Cooper pairs via an effective phonon-mediated attraction, producing an energy gap and dissipationless current [4]. This explained what we now know as “conventional” low- T_c superconductors. In the 1980s, Bednorz and Müller discovered cuprate high- T_c superconductors like $\text{Ba}_x\text{La}_{5-x}\text{Cu}_5\text{O}_{5(3-y)}$ [5], quickly followed by other materials [6]. This discovery enabled operation with liquid nitrogen and opening a new era of unconventional superconductivity research, where the pairing mechanism is likely not purely phononic. BCS theory has failed to explain these new results and there is still no widely accepted unified theory of unconventional superconductivity [7]. In the following years, different materials with higher critical temperatures have been discovered, but the ultimate goal of superconductivity at ambient conditions has not yet been reached [8]. This discovery showed Superconductivity can be split into two classes – conventional or unconventional – depending on the symmetry of the underlying order parameter¹.

A particularly interesting and elusive class of unconventional superconductors are the so-called spin-triplet superconductors. Motivated by the discovery of the superfluidity of ^3He and the Anderson-Brinkman-Morel model in the 1970s [9, 10, 11], Fay and Appel theoretically predicted the presence of the equal-spin triplet paring in the ferromagnet ZrZn_2 in 1980 [12]. Superconductivity was later observed to coexist with itinerant ferromagnetism in compounds such as UGe_2 , URhGe [13, 14], and UTe_2 [15] implying the existence of a spin-polarized triplet state. The chiral triplet p -wave ($p_x + ip_y$) superconducting order is of high interest due to its edge states and potential applications in quantum technology [16]. Previous work has shown that edge states of a p -wave superconductor can be topologically protected from decoherence [17]. One of the best studied candidates for topological superconductivity is the surface of Sr_2RuO_4 [18], but the exact superconducting order parameter is still debated [19, 20]. The unconventional pairing in superconductors is notoriously sensitive to disorder, and hence can only be observed in strictly controlled conditions [21]. It is therefore important to find a method to enhance the critical temperature of unconventional superconductors in order to easily access their physics.

1.2 Superconductivity and magnetism

Superconductivity and magnetism are, in general, competing orders. In a conventional spin-singlet s -wave superconductor, Cooper pairs form spin-antisymmetric states with total spin $\sigma = 0$. A homogeneous exchange field couples to the electron spin and lifts the spin degeneracy at the Fermi level, thereby breaking time-reversal symmetry and tending to destabilize singlet pairing. Microscopically, this manifests as a pair-breaking effect: even dilute magnetic impurities can suppress the superconducting order parameter and reduce the critical temperature T_c [22]. In systems where superconductivity coexists with ferromagnetism, such as the uranium-based compounds mentioned above, the simple antagonistic picture must be generalized. The exchange-split Fermi surfaces favor spin-triplet correlations, especially equal-spin pairing, which is less sensitive to the internal field. This provides a microscopic route to stabilize unconventional triplet Cooper pairs inside a ferromagnetic background [12].

A key mechanism underlying the effective magnetic interactions in metallic systems is the Ruderman–Kittel–Kasuya–Yosida (RKKY) interaction [23, 24, 25]. The RKKY interaction describes an indirect exchange coupling between localized magnetic moments \mathbf{s}_i mediated by itinerant conduction electrons.

¹An order parameter is a quantity that is zero in some thermodynamic phase but non-zero in others. Examples are the magnetization of a ferromagnet and the gap function in a superconductor.

tion electrons. For two localized spins, when one couples to the itinerant electrons, its lowest-energy spin orientation depends on the orientation of the other spin and their distance. The study of the RKKY interaction has proven to be important for the development of spin valves and tunneling magnetoresistance devices [26]. Beyond its relevance in purely metallic magnets, the same conduction electrons that mediate the RKKY interaction also carry superconducting correlations in hybrid structures. When two localized spins are placed on the surface of a superconductor, the RKKY interaction has been suggested as a tool for determining superconducting order parameter symmetries from spin measurements [27]. Moreover, it is a key step between pure superconductivity and more complex proximity systems.

1.3 Proximity systems

Particularly interesting are mesoscopic hybrid structures consisting of superconducting components conjoined with other materials. Cooper pairs generated in the superconductor can leak across an interface into a non-superconducting material, inducing new properties known as proximity effects. A paradigmatic example is a superconductor–normal-metal (SN) structure. Here, Andreev reflection [28] at the SN interface converts normal electrons and holes into Cooper pairs and vice versa, leading to an induced pair amplitude in the normal region over a characteristic coherence length. As a result, the normal metal can acquire a reduced low-energy density of states (a minigap), carry a supercurrent when embedded between two superconductors, and exhibit phase-coherent transport phenomena. The strength and spatial range of these effects are governed by the interface transparency, the transport regime, and the geometry of the mesoscopic conductor.

The Josephson effect² was first predicted by B. D. Josephson in 1962 [29] and soon experimentally verified [30]. This gave rise to an entire class of proximity devices based on Josephson junctions, where two superconducting electrodes are weakly coupled through a thin barrier [31]. Depending on the nature of this barrier we usually distinguish between superconductor–insulator–superconductor (SIS), superconductor–normal-metal–superconductor (SNS), and superconductor–ferromagnet–superconductor (SFS) junctions. In SIS junctions, a thin insulating layer allows coherent tunneling of Cooper pairs and yields a well-defined Josephson coupling. In SNS junctions, a normal metal serves as the weak link, and the supercurrent is carried by proximity-induced correlations in the normal region. In SFS junctions, a ferromagnetic barrier with an internal exchange field gives rise to an oscillatory and strongly damped proximity effect. Singlet correlations induced into the ferromagnet acquire a finite center-of-mass momentum and exhibit a damped oscillatory behavior as a function of distance from the interface, giving rise to qualitatively new effects such as $0\text{--}\pi$ transitions of the junction ground state and a strongly modified current–phase relation [32].

Proximity systems have been shown to increase the critical temperatures of superconductors. An example is an *s*-wave/*s*-wave bilayer, where a thin low- T_c *s*-wave metal (e.g., Al) in good contact with a higher- T_c *s*-wave superconductor (e.g., Pb) exhibits an enhanced superconducting transition temperature due to the proximity effect [33]. There have been a lot of development in the study of such phenomena in systems involving ferromagnets [34, 35]. For instance, recent theoretical work indicates that when a conventional *s*-wave superconductor is coupled to a triplet superconductor across a ferromagnetic interface, the *p*-wave component can be tuned and enhanced [36]. The ferromagnet in this case acts as a spin-active interface that enables singlet–triplet conversion, since singlet Cooper pairs do not otherwise couple directly to triplet pairs [37]. In fact, both ferromagnets [38] and materials with spin-orbit coupling [39] have been used to study the Josephson effect in a *s*-wave–*p*-wave proximity system.

1.4 Objective and structure

The main objective of this project is to develop the theoretical framework and numerical tools required for a forthcoming master’s thesis on proximity systems, with the goal of stabilizing uncon-

²The Josephson effect is the flow of a supercurrent between two superconductors separated by a thin barrier (insulating, normal, or ferromagnetic), sustained without an applied voltage. It arises because of the difference in the macroscopic superconducting phases on the two sides.

ventional triplet states by magnetic coupling to a high-temperature superconductor in a proximity system. To this end, we first provide in sections 2 and 3 a brief review of the necessary preliminaries and introduce the tight-binding model together with the underlying lattice structures. At the end of section 3, we also present the extended Hubbard model and outline its potential applications in describing correlated systems. In section 4, we turn to magnetism, formulating its theoretical description both in terms of an effective exchange field and within the Hubbard model. Conventional and unconventional superconductivity are then discussed in section 5. The Bogoliubov-de Gennes equations are derived, along with the associated self-consistency equations for the gap. These are implemented numerically for a BCS superconductor and solved for the gap and critical temperature. This section concludes with a study of edge effects in unconventional superconductors and brief discussion of the self-consistent schemes for unconventional superconductors and the challenges involved in their implementation. Next, section 6 introduces the Ruderman–Kittel–Kasuya–Yosida (RKKY) interaction in different host materials. We implement the interaction numerically on square and triangular lattices and analyze how the host material influences the effective magnetic interactions. We study magnetic frustration in the case of a triangular geometry and the resulting ground-state spin configurations. In the last section, we address proximity effects and Andreev reflection, and introduce prototypical Josephson junction geometries such as SNS and SFS junctions, illustrating the theoretical concepts with supporting numerical calculations. Finally, general conclusions are presented, together with a short outlook for future work and research.

2 Preliminaries

2.1 Mathematical notation

The notation in this thesis will mostly follow established physics conventions. Vectors are denoted by bold lowercase letters, matrices by bold uppercase letters, and operators by a “hat” symbol, \hat{O} , unless stated otherwise. The commutator of two operators (or matrices) is defined as $[\mathbf{A}, \mathbf{B}] \equiv \mathbf{AB} - \mathbf{BA}$, and the anticommutator as $\{\mathbf{A}, \mathbf{B}\} \equiv \mathbf{AB} + \mathbf{BA}$. Partial derivatives are written in the shorthand notation $\partial_x f(x, y) = \partial f(x, y)/\partial x$, and ∂ without subscripts is equivalent to the gradient operator, $\partial \equiv \nabla$. Integration limits and summation ranges may be omitted if they are clear from the context or if they are yet unknown. Sums over nearest-neighbor pairs are indicated by $\sum_{\langle i,j \rangle}$. Unless otherwise stated, \mathbf{r} is a spatial coordinate, T is an absolute temperature, \mathbf{k} a wave vector, and σ a spin. The Dirac delta function is $\delta(t - t_0)$, and δ_{ij} is the Kronecker delta. The Pauli matrices are defined as

$$\sigma^1 = \sigma_x = \begin{bmatrix} 0 & 1 \\ 1 & 0 \end{bmatrix}, \quad \sigma^2 = \sigma_y = \begin{bmatrix} 0 & -i \\ i & 0 \end{bmatrix}, \quad \sigma^3 = \sigma_z = \begin{bmatrix} 1 & 0 \\ 0 & -1 \end{bmatrix}. \quad (2.1)$$

Sometimes it is convenient to group the Pauli matrices into a single object called the Pauli vector:

$$\mathbf{S} = \sigma^1 \hat{\mathbf{e}}_1 + \sigma^2 \hat{\mathbf{e}}_2 + \sigma^3 \hat{\mathbf{e}}_3, \quad (2.2)$$

where $\{\hat{\mathbf{e}}_1, \hat{\mathbf{e}}_2, \hat{\mathbf{e}}_3\}$ are the cardinal unit vectors. Additionally, the spin ladder matrices can be constructed as $\sigma^\pm \equiv \sigma^1 \pm i\sigma^2$. Together with the 2×2 identity matrix

$$\sigma^0 = \mathbb{I}^{2 \times 2} = \begin{bmatrix} 1 & 0 \\ 0 & 1 \end{bmatrix}, \quad (2.3)$$

the Pauli matrices span the entire spin space of 2×2 matrices.

2.2 Natural units

The laws of physics should not change depending on the physical units used. Therefore, it must be possible to simplify the mathematical expressions describing these laws by selecting a unit system where most constants take the value of one. A common choice in condensed matter physics is the Heaviside–Lorentz *natural units*, which are defined by:

$$\hbar = k_B = c = \epsilon_0 = \mu_0 = 1, \quad (2.4)$$

where \hbar is Planck’s reduced constant, k_B is Boltzmann’s constant, c is the speed of light in vacuum, and ϵ_0 and μ_0 are the vacuum permittivity and permeability, respectively. Equation (2.4) defines a system of physical units expressed in terms of physical constants. Any conventional unit system can then be recovered by plugging in the corresponding experimental values for the above-mentioned constants.

Note that in these units the wave vector is equivalent to crystal momentum, $\mathbf{k} \equiv \mathbf{p}$, since $\mathbf{p} = \hbar\mathbf{k}$.

2.3 The second quantization formalism

Systems of many particles can be conveniently represented in the language of *second quantization*. The formalism provides a compact way of representing the many-body space of excitations, with all the properties of the ladder operators encoded in a simple set of commutation relations. The basics of the formalism are introduced in this section based on the book by Altland and Simons [40].

In our notation, the quantum states are represented in the form $|n_1, n_2, \dots\rangle$, with n_i denoting the number of particles in single-particle state i . The set $\{|n_1, n_2, \dots\rangle\}$ defines the occupation number basis for the Fock space \mathcal{F} —a Hilbert space large enough to accommodate a state with an

undetermined number of particles. A general many-body state $|\Psi\rangle$ can then be represented as a linear superposition $|\Psi\rangle = \sum_{n_1, n_2, \dots} \alpha_{n_1, n_2, \dots} |n_1, n_2, \dots\rangle$, for a set of coefficients $\{\alpha_{n_1, n_2, \dots}\}$.

We can now define a *creation operator* as a linear map $\hat{c}_i^\dagger : \mathcal{F} \rightarrow \mathcal{F}$ for every $i = 1, 2, \dots$, such that applying the bosonic creation operator to a state $|n_1, n_2, \dots, n_i, \dots\rangle$ gives

$$\hat{c}_i^\dagger |n_1, n_2, \dots, n_i, \dots\rangle \equiv \sqrt{n_i + 1} |n_1, n_2, \dots, n_i + 1, \dots\rangle. \quad (2.5)$$

Due to Pauli's exclusion principle, the occupation numbers n_i for fermions can only be 0 and 1, meaning that the twofold application of the fermionic creation operator to any state leads to total annihilation, $(\hat{c}_i^\dagger)^2 = 0$. Its action on a state $|n_1, n_2, \dots, n_i, \dots\rangle$ is then

$$\hat{c}_i^\dagger |n_1, n_2, \dots, n_i, \dots\rangle \equiv \begin{cases} (-1)^{s_i} |n_1, n_2, \dots, n_i + 1, \dots\rangle, & \text{for } n = 0 \\ 0, & \text{for } n \neq 0 \end{cases} \quad (2.6)$$

where $s_i = \sum_{j=0}^{i-1} n_j$.

Any state in the Fock space can be constructed by repeatedly applying the creation operator to the vacuum state $|0\rangle$:

$$|n_1, n_2, \dots\rangle = \prod_i \frac{1}{\sqrt{n_i!}} (\hat{c}_i^\dagger)^{n_i} |0\rangle. \quad (2.7)$$

The *annihilation operator* is obtained by taking the hermitian conjugate of the creation operator, $\hat{c}_i \equiv (\hat{c}_i^\dagger)^\dagger$, and has the effect of reducing the number of particles n_i by 1. The application of this operator on the vacuum state, $\hat{c}_i |0\rangle = 0$, annihilates it.

The pairs of creation and annihilation operators are also sometimes called ladder operators. Fermions are antisymmetric under exchange of single-particle coordinates. This antisymmetry is reflected in the anticommutation relations between \hat{c}_i^\dagger and \hat{c}_j :

$$\{\hat{c}_i^\dagger, \hat{c}_j\} = \delta_{ij}, \quad \{\hat{c}_i^\dagger, \hat{c}_j^\dagger\} = 0, \quad \{\hat{c}_i, \hat{c}_j\} = 0, \quad (2.8)$$

for any $i, j = 1, 2, \dots$. This relation explains the $(-1)^{s_i}$ term in Eq. (2.6). Conversely, for bosons that are symmetric under exchange of coordinates, the ladder operators satisfy commutation instead,

$$[\hat{c}_i^\dagger, \hat{c}_j] = \delta_{ij}, \quad [\hat{c}_i^\dagger, \hat{c}_j^\dagger] = 0, \quad [\hat{c}_i, \hat{c}_j] = 0. \quad (2.9)$$

From the fermionic creation and annihilation operators we define the *local number operator* as

$$\hat{c}_i^\dagger \hat{c}_i = \hat{n}_i, \quad (2.10)$$

This operator just counts the number of particles in a state i , $\hat{n}_i |n_1, \dots, n_i, \dots\rangle = n_i |n_1, \dots, n_i, \dots\rangle$. The *total number operator* $\hat{N} = \sum_i \hat{n}_i$,

$$\hat{N} |n_1, \dots, n_i, \dots\rangle = \sum_i n_i |n_1, \dots, n_i, \dots\rangle, \quad (2.11)$$

as the name suggests, counts the total number of particles in the entire system.

2.4 Representation of operators in second quantization

A one-body operator acts on a single particle at a time, while the rest are unaffected. Such operator, \hat{O}_1 can be represented in second quantization as

$$\hat{O}_1 = \sum_{\mu\nu} \langle \mu | \hat{o} | \nu \rangle \hat{c}_\mu^\dagger \hat{c}_\nu, \quad (2.12)$$

where \hat{o} is an ordinary single-particle operator and the states $|\mu\rangle$ and $|\nu\rangle$ are single-particle states forming a basis of the one-particle Hilbert space. Two common examples are the local and total spin operator, written in the form

$$\hat{\mathbf{S}} = \frac{1}{2} \sum_i \hat{c}_{i,\sigma}^\dagger \mathbf{S}_{\sigma,\sigma'} \hat{c}_{i,\sigma'}. \quad (2.13)$$

and the one-body Hamiltonian³ for a free particle

$$\hat{H} = \int d\mathbf{r} \hat{c}^\dagger(\mathbf{r}) \left[\frac{\hat{\mathbf{p}}^2}{2m} + V(\mathbf{r}) \right] c(\mathbf{r}), \quad (2.14)$$

where $\hat{\mathbf{p}} = -i\hbar\partial$ and $V(\mathbf{r})$ is some external potential.

Single-body operators, however, are not sufficient to describe interactions between particles. For that purpose we need to introduce two-body operators.

$$\hat{O}_2 = \sum_{\kappa,\lambda,\mu,\nu} O_{\kappa\lambda\mu\nu} \hat{c}_\kappa^\dagger \hat{c}_\lambda^\dagger \hat{c}_\mu \hat{c}_\nu, \quad (2.15)$$

where $O_{\kappa,\lambda,\mu,\nu} \equiv \langle \kappa\lambda | \hat{O}_2 | \mu\nu \rangle$. Prototypical examples in condensed matter physics are the electron-electron interaction

$$\hat{V}_{ee} = \frac{1}{2} \int d\mathbf{r} \int d\mathbf{r}' V_{ee}(\mathbf{r} - \mathbf{r}') \hat{c}_\sigma^\dagger(\mathbf{r}) \hat{c}_{\sigma'}^\dagger(\mathbf{r}') \hat{c}_{\sigma'}(\mathbf{r}') \hat{c}_\sigma(\mathbf{r}) \quad (2.16)$$

and the spin-spin interaction

$$\hat{V} = \frac{1}{2} \int d\mathbf{r} \int d\mathbf{r}' J(\mathbf{r}, \mathbf{r}') \mathbf{S}_{\alpha,\beta} \mathbf{S}_{\alpha',\beta'} \hat{c}_\alpha^\dagger(\mathbf{r}) \hat{c}_{\alpha'}^\dagger(\mathbf{r}') \hat{c}_{\alpha'}(\mathbf{r}') \hat{c}_\beta(\mathbf{r}), \quad (2.17)$$

where $J(\mathbf{r}, \mathbf{r}')$ is the exchange interaction.

2.5 Nambu space

In condensed matter and quantum field theory, Nambu space (also called Nambu-Gor'kov space) is a formal doubling of the Hilbert space used to treat systems where particle number conservation is effectively broken, most notably in superconductivity. Consider the fermionic ladder operators ($\hat{c}_{i,\sigma}$, $\hat{c}_{j,\sigma}^\dagger$). If the Hamiltonian only involves bilinear terms in $\hat{c}_{i,\sigma}^\dagger \hat{c}_{j,\sigma'}$ diagonalization is relatively simple. However, when particle non-conserving terms such as $\hat{c}_{i,\sigma} \hat{c}_{j,\sigma'}$ and $\hat{c}_{i,\sigma}^\dagger \hat{c}_{j,\sigma'}^\dagger$ are present, it is convenient to introduce a two-component *Nambu spinor* combining \uparrow -creation and \downarrow -annihilation in a single object [41]:

$$\Psi_i = \begin{pmatrix} \hat{c}_{i,\uparrow} \\ \hat{c}_{i,\downarrow}^\dagger \end{pmatrix} \quad \text{and} \quad \Psi_i^\dagger = \begin{pmatrix} \hat{c}_{i,\uparrow}^\dagger \\ \hat{c}_{i,\downarrow} \end{pmatrix}. \quad (2.18)$$

This object lives in Nambu space. Operators in this space transform under Pauli matrices, in analogy with spinors. Note that in condensed matter theory, Pauli matrices in Nambu space are conventionally denoted by τ^i , to differentiate them from their spin space counterpart, σ^i . The Nambu space can generally be extended to Nambu \otimes Spin space, containing all spin degrees of freedom, by introducing the so-called Nambu bispinor:

$$\hat{\mathbf{c}}_i = \left(\hat{c}_{i,\uparrow}, \hat{c}_{i,\downarrow}, \hat{c}_{i,\uparrow}^\dagger, \hat{c}_{i,\downarrow}^\dagger \right)^T. \quad (2.19)$$

The Nambu representation handles this mixing of particle creation and annihilation operators, transforming the problem into a standard eigenvalue problem for a single-particle Hamiltonian,

$$\hat{H} = E_0 + \frac{1}{2} \sum_{i,j} \hat{\mathbf{c}}_i^\dagger \hat{\mathbf{H}}_{ij} \hat{\mathbf{c}}_j, \quad (2.20)$$

³ The operators $\hat{c}^\dagger(\mathbf{r})$ and $c(\mathbf{r})$ are called quantum field operators, representing creation and annihilation operators in real space. In much of the literature, they are instead denoted by $\psi^\dagger(\mathbf{r})$ and $\psi(\mathbf{r})$, respectively.

where $\hat{\mathbf{H}}_{ij}$ is a 4×4 matrix. For a finite lattice with N sites, this equation can be further compressed by collecting all site spinors into a single operator vector. Following the convention used by Ouassou [42], this extended object that lives in Lattice \otimes Nambu \otimes Spin space is defined as:

$$\check{\mathbf{c}} = (\hat{\mathbf{c}}_1, \hat{\mathbf{c}}_2, \dots, \hat{\mathbf{c}}_N)^T. \quad (2.21)$$

The Hamiltonian, Eq. (2.20), can now be written as:

$$\hat{H} = E_0 + \frac{1}{2} \check{\mathbf{c}}^\dagger \check{\mathbf{H}} \check{\mathbf{c}}, \quad (2.22)$$

where $\check{\mathbf{H}}$ is the extended Hamiltonian matrix

$$\check{\mathbf{H}} = \begin{pmatrix} \hat{\mathbf{H}}_{11} & \cdots & \hat{\mathbf{H}}_{1N} \\ \vdots & \ddots & \vdots \\ \hat{\mathbf{H}}_{N1} & \cdots & \hat{\mathbf{H}}_{NN} \end{pmatrix}. \quad (2.23)$$

The crucial advantage of this construction is that the eigenvalues of \hat{H} correspond directly to those of the matrix \mathbf{H} . Hence, the many-body problem reduces to the diagonalization of a finite-dimensional matrix, which can be done using standard linear algebra techniques. A potential challenge is that extended matrix is of dimension $4N \times 4N$, and can scale very rapidly with increased system size N . However, in practice, the matrix is usually very sparse with very few non-diagonal entries. Utilizing this sparsity can significantly lower the computational complexity.

Note that we use a single index here, it can be used to represent higher dimensional systems. For example the coordinates of a 2D system can be mapped to a single lattice index as shown in fig. 1.

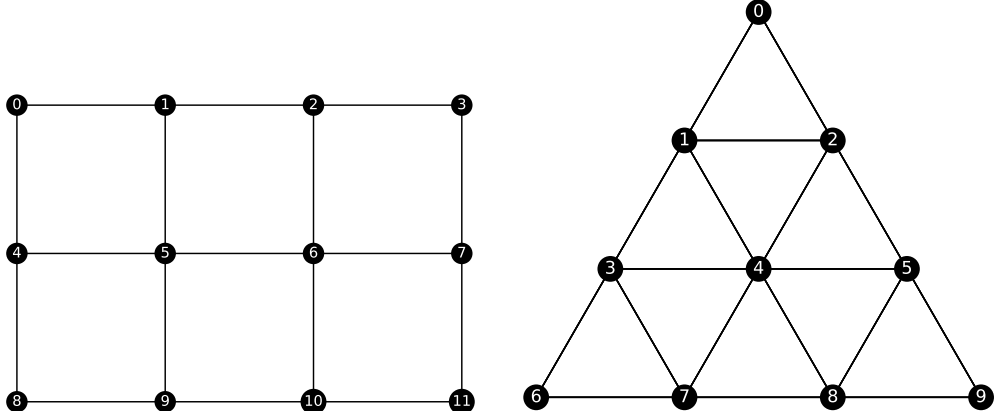


Figure 1: Example of a two-dimensional square (left) and triangular (right) lattice, where each lattice site is assigned a single integer index. This indexing scheme allows the Hamiltonian to be written compactly in Lattice \otimes Nambu \otimes Spin space.

3 Tight-Binding Model and Lattice Structure

The tight-binding model [43] is used to describe the motion of electrons in a periodic potential created by a lattice of positive ions. It is based on the assumption that electrons remain strongly localized around atomic sites, with their dynamics governed primarily by quantum-mechanical tunneling (hopping) between neighboring orbitals. This picture is especially appropriate for systems where atomic orbitals overlap weakly, such as transition-metal oxides or covalently bonded solids, but it is often a good approximation for other materials as well.

This section introduces Wannier orbitals and explains how to construct the tight-binding Hamiltonian for electrons in a lattice. We then diagonalize the Hamiltonian via Fourier transformation to momentum space and show how to compute physical observables such as the density of states. Finally, we extend the model to include electron–electron interactions through the extended Hubbard model.

3.1 Wannier orbitals and atomic lattices

In a crystalline solid, electrons move in the periodic potential created by the lattice of ions. While the theory developed here is not tied to any particular lattice geometry, we will, for concreteness, specialize in the following to a simple cubic lattice with lattice constant a . We can then select a basis of *Wannier orbitals*

$$\langle \mathbf{r}|i\rangle = w(\mathbf{r} - \mathbf{r}_i), \quad (3.1)$$

since they are localized and orthonormal [42, 43, 44]. Orbitals are localized in the sense that they become large closer to the atomic site \mathbf{r}_i with number i . The field annihilation and creation operators for a fermion with spin σ at position \mathbf{r} ($\hat{c}_\sigma(\mathbf{r}), \hat{c}_\sigma^\dagger(\mathbf{r})$) can be expressed in this basis as

$$\hat{c}_\sigma(\mathbf{r}) \equiv \sum_i w(\mathbf{r} - \mathbf{r}_i) \hat{c}_{i,\sigma} \quad \text{and} \quad \hat{c}_\sigma^\dagger(\mathbf{r}) \equiv \sum_i w^*(\mathbf{r} - \mathbf{r}_i) \hat{c}_{i,\sigma}^\dagger, \quad (3.2)$$

where $\hat{c}_{i,\sigma}$ ($\hat{c}_{i,\sigma}^\dagger$) annihilates (creates) a spin- σ particle at lattice site i .

3.2 Tight-binding Hamiltonian for a metal

For simplicity, let us assume periodic boundary conditions and that there is one electron per atom relevant for conduction. Furthermore, assume that the system consists of noninteracting electrons. A natural starting point in deriving the tight-binding Hamiltonian for the system is

$$\hat{H} = \sum_{\sigma,\sigma'} \int d\mathbf{r} \hat{c}_\sigma^\dagger(\mathbf{r}) \left(-\frac{\nabla^2}{2m} + U(\mathbf{r}) \right) \delta_{\sigma\sigma'} \hat{c}_{\sigma'}(\mathbf{r}) \equiv \sum_\sigma \int d\mathbf{r} \hat{c}_\sigma^\dagger(\mathbf{r}) H(\mathbf{r}) \hat{c}_\sigma(\mathbf{r}), \quad (3.3)$$

where we have defined $H(\mathbf{r}) = -\frac{\partial^2}{2m} + U(\mathbf{r})$, containing the kinetic and potential energy of an electron with respect to the ions [42]. This is a general one-particle Hamiltonian in the absence of gauge fields. It commutes with the translation operator \hat{T}_a which shifts by one lattice spacing a . This means that both operators have the same eigenstates, namely plane waves. The transition from a continuum model to a tight-binding model can then be formalized by calculating matrix elements and taking advantage of the orthonormality of the Wannier orbitals. Equation (3.3) then becomes

$$\hat{H} = \sum_{\langle i,j \rangle, \sigma} \langle i | H(\mathbf{r}) | j \rangle \hat{c}_{i,\sigma}^\dagger \hat{c}_{j,\sigma} \equiv - \sum_{\langle i,j \rangle, \sigma} t_{i,j} \hat{c}_{i,\sigma}^\dagger \hat{c}_{j,\sigma}. \quad (3.4)$$

The matrix element $t_{i,j}$ is the hopping amplitude and is given by the integral:

$$t_{i,j} = - \sum_{\sigma'} \int d\mathbf{r} w^*(\mathbf{r} - \mathbf{r}_i) H(\mathbf{r}) w(\mathbf{r} - \mathbf{r}_j). \quad (3.5)$$

The hopping amplitude is related to the probability of an electron moving from site j to i , i.e., an electron with spin σ is created at site i and an electron with spin σ is annihilated at site j . Here we have restricted the analysis to nearest-neighbor hopping, but the expression can be further expanded to higher orders. This is justified since the integral in Eq. (3.5) becomes smaller when the overlap between the orbitals is reduced, the next-nearest neighbor hopping can be neglected in a tight-binding treatment. It is customary to take the hopping amplitudes t_{ij} to be positive and real. In theoretical and numerical models, it is often assumed site-independent $t \equiv t_{ij}$ and as the base unit that other energies are measured against.

3.3 Diagonalizing the tight-binding Hamiltonian

The Hamiltonian in Eq. (3.4) is not diagonal in real space. To diagonalize it, we use the translational invariance of the system, mentioned in section 3.1, and Fourier-transform the creation and annihilation operators from real space to \mathbf{k} -space:

$$\hat{c}_{i,\sigma} = \frac{1}{\sqrt{N}} \sum_{\mathbf{k}} \hat{c}_{\mathbf{k},\sigma} e^{i\mathbf{k}\cdot\mathbf{r}_i}, \quad (3.6)$$

$$\hat{c}_{i,\sigma}^\dagger = \frac{1}{\sqrt{N}} \sum_{\mathbf{k}} \hat{c}_{\mathbf{k},\sigma}^\dagger e^{-i\mathbf{k}\cdot\mathbf{r}_i}. \quad (3.7)$$

It can be shown that each \mathbf{k} -component lies within the region $[-\pi/a, \pi/a]$, called the first Brillouin zone, meaning that wave vectors differing by an integer multiple of $2\pi/a$ are equivalent to each other.

We can assume, for simplicity, a one-dimensional system, i.e., $\mathbf{k} = (k, 0, 0)$. Generalizing to higher dimensions is achieved by simply repeating the procedure along each \mathbf{k} -component. Assuming also a constant $t_{ij} = t > 0$ and using the transformations in Eqs. (3.6) and (3.7), the Hamiltonian in Eq. (3.4) becomes:

$$\hat{H} = -t \frac{1}{N} \sum_j \sum_{k,k'} \left(e^{-ik'a} + e^{ik'a} \right) e^{-i(k-k')r_j} \hat{c}_{k,\sigma}^\dagger \hat{c}_{k',\sigma}. \quad (3.8)$$

Here, we can see that the expression in the parentheses is $e^{-ik'a} + e^{ik'a} = 2 \cos(k'a)$ and identify the discrete orthogonality relation for Fourier transforms on a finite lattice:

$$\delta_{k,k'} = \frac{1}{N} \sum_j e^{-i(k-k')r_j}. \quad (3.9)$$

Inserting this into Eq. (3.8), we get a Hamiltonian that is diagonal in k

$$\hat{H} = \sum_{k,\sigma} -t\alpha_k \hat{c}_{k,\sigma}^\dagger \hat{c}_{k,\sigma}, \quad (3.10)$$

with a structure factor $\alpha_k = 2 \cos(ka)$. From here it is easy to obtain the energy dispersion and other observables. We can further perform a parabolic expansion to obtain the dispersion around a small $|k| \ll a$

$$E(k) \approx -2t + \frac{k^2}{2m^*} + \mathcal{O}(k^4), \quad (3.11)$$

as shown in fig. 2. Note that this can be recognized as the expression of a free particle with effective mass m^* . The effective mass here is defined as $1/m^* = 2ta^2$ and contains all the effects from the interaction with the lattice ions.

3.4 Calculating physical observables

The grand canonical ensemble is a common way of describing many-particle systems in thermal equilibrium. In the grand canonical ensemble, the system has a variable number of particles, but a

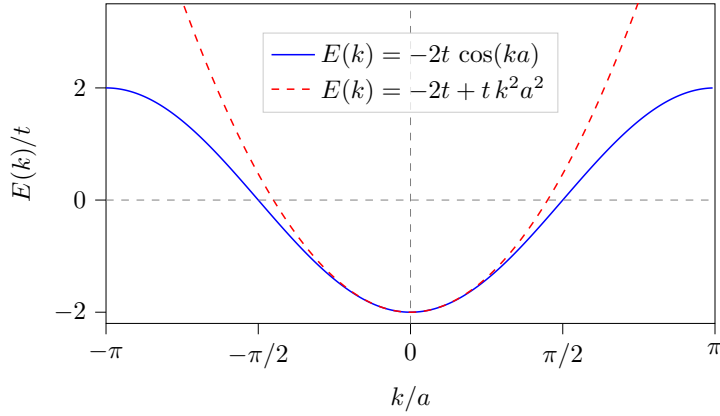


Figure 2: Energy dispersion $E(k)$ for a one-dimensional tight-binding chain. The blue solid curve shows the exact tight-binding result, while the red dashed curve represents the harmonic approximation near the band minimum, $E(k) \approx -2t + tk^2a^2$.

fixed chemical potential μ . The average number of particles is then well defined. The Hamiltonian in the grand canonical ensemble is usually written as [45, 44]

$$\hat{H} \rightarrow \hat{H} - \mu \hat{N}, \quad (3.12)$$

where \hat{N} is the total number operator. In the grand canonical ensemble Eq. (3.10) becomes:

$$\hat{H} = \sum_{\mathbf{k},\sigma} (-2t \cos ka - \mu) \hat{c}_{\mathbf{k},\sigma}^\dagger \hat{c}_{\mathbf{k},\sigma}. \quad (3.13)$$

Once the Hamiltonian in Eq. (3.13) is diagonalized, we obtain the dispersion relation

$$\xi_{\mathbf{k}} = -2t \cos ka - \mu. \quad (3.14)$$

The diagonalized Hamiltonian yields single-particle energies that can be used to calculate different physical observables, such as the average occupation number $\langle n_{\mathbf{k},\sigma} \rangle$ as

$$\langle n_{\mathbf{k},\sigma} \rangle = f(\xi_{\mathbf{k},\sigma}) \equiv \frac{1}{e^{\xi_{\mathbf{k},\sigma}/T} + 1}, \quad (3.15)$$

also known as the Fermi-Dirac distribution [46]. From this distribution average occupation number per spin can be obtained by taking an average over the momentum-resolved contributions:

$$\langle n_\sigma \rangle = \frac{1}{N} \sum_{\mathbf{k}} f(\xi_{\mathbf{k},\sigma}) \quad (3.16)$$

Another useful physical observable is the density of states (DOS), which up to normalization can be computed as:

$$D(E) = \sum_{\mathbf{k}} \delta(E - \xi_{\mathbf{k}}). \quad (3.17)$$

Note that in Eq. (3.14), the eigenvalues are independent of spin (spin degenerate). This means that in the ground state, the system will contain as many spin-up as spin-down electrons leading to a paramagnetic (PM) ordering.

The Helmholtz free energy is a common choice for systems at fixed temperature and volume. It is defined in terms of the internal energy U and the entropy S [45], and can also be obtained from the eigenvalues of the Hamiltonian:

$$\mathcal{F} = U - TS. \quad (3.18)$$

Once the Hamiltonian is diagonalized and the eigenvalues $\xi_{\mathbf{k}}$ are known, we can calculate all the quantities in Eq. (3.18) [27]:

$$U = \mathcal{E}_0 - \frac{1}{2} \sum_{\mathbf{k}} \xi_{\mathbf{k}}, \quad (3.19)$$

$$S = \sum_{\mathbf{k}} \log [1 + \exp (-\xi_{\mathbf{k}}/T)]. \quad (3.20)$$

\mathcal{E}_0 is a constant term that arises due to the different approximations and symmetrization of the Hamiltonian [47] and is usually neglected when comparing free energies of different systems or configurations. Note, however, that \mathcal{E}_0 can become important when performing self-consistent calculations, as shown later in sections 5 and 7.

3.5 The extended Hubbard model

The Hubbard model is a basic model describing strongly correlated electronic systems. It is essentially an extension to the tight-binding model including electron-electron interactions. The original model, first introduced by John Hubbard in his paper from 1963 [48], only considers on-site interactions. However, even back in the 1960s Hubbard suggested that for real world materials, a model considering beyond-on-site interactions is necessary. The extended Hubbard model is suitable for systems where the nearest-neighbor interaction become important [49, 50]. Generally the extended Hubbard model is given by the Hamiltonian

$$H = - \sum_{\langle i,j \rangle, \sigma} t \hat{c}_{i,\sigma}^\dagger \hat{c}_{j,\sigma} + \sum_i U \hat{n}_{i,\uparrow} \hat{n}_{i,\downarrow} + \sum_{\langle i,j \rangle, \sigma, \sigma'} V \hat{n}_{i,\sigma} \hat{n}_{j,\sigma'} - \mu \sum_{i,\sigma} \hat{n}_{i,\sigma}, \quad (3.21)$$

where U and V are the Coulomb interaction parameters and t is the hopping energy.

In this section we briefly introduce the extended Hubbard model following the approach of Keeling [51]. We continue to consider electrons moving in a regular lattice of ions. The electron-electron interaction is modeled by the Hamiltonian in Eq. (2.16). Using the Wannier orbitals from Eq. (3.1) as basis functions, the Hamiltonian can be written as

$$\hat{H}_{ee} = \frac{1}{2} \sum_{i,j,k,l,\sigma,\sigma'} V_{ijkl} \hat{c}_{i,\sigma}^\dagger \hat{c}_{j,\sigma'}^\dagger \hat{c}_{l,\sigma'} \hat{c}_{k,\sigma}, \quad (3.22)$$

where

$$V_{ijkl} = \int d\mathbf{r} \int d\mathbf{r}' w^*(\mathbf{r} - \mathbf{r}_i) w^*(\mathbf{r}' - \mathbf{r}_j) V_{ee}(\mathbf{r} - \mathbf{r}') w(\mathbf{r} - \mathbf{r}_k) w(\mathbf{r}' - \mathbf{r}_l) \quad (3.23)$$

If the wavefunctions are reasonably localized, we can restrict the sum to on-site and nearest neighbor terms; i.e. for i, j, k, l we take at most two different sites. Terms like $\hat{c}_{i,\sigma}^\dagger \hat{c}_{i,\sigma}^\dagger$ cancel out due to the Pauli exclusion principle. Furthermore, since quantum particles are indistinguishable, terms like $\hat{n}_{i,\uparrow} \hat{n}_{i,\downarrow}$ and $\hat{n}_{i,\downarrow} \hat{n}_{i,\uparrow}$ are identical. The surviving terms can take one of the forms shown in table 1 below:

The size of the coefficients U, A, V, F, P in the above expressions can be determined by calculating the overlap matrix elements. Compared to the Hubbard term, the other expressions are reduced because they involve overlap of wavefunctions centered on different sites.

The different terms in table 1 have different effects on the system. Notably, the U term with $U < 0$ is an “attractive Hubbard model” that could give rise to BCS superconductivity, while the nearest neighbor interaction (the V -term) term with $V < 0$ can be used to derive unconventional superconductivity. The A -term ties the electron itinerancy to the local interaction environment, leading to nontrivial renormalization of both the charge transport and the effective interactions, and is often analyzed in the context of unconventional superconductivity. It is important to note that this term is the only term in the extended Hubbard model that does not respect electron-hole symmetry. Electron-hole symmetry in this context means an invariance of the Hamiltonian under particle-hole transformation of the fermionic operators. For example, adding an electron

Table 1: Relevant two-body interaction processes in the extended Hubbard model, classified by site index relations. The table includes the on-site Hubbard repulsion, correlated (assisted) hopping, nearest-neighbor interactions, exchange and pair hopping terms. The site indices in the contribution column have been relabeled for readability. There are 4 distinct permutations of the site indices for the A -term, but only one is shown here. Based on the table on page 26 in Ref. [51].

Choice of site	Contribution	Description
$i = j = k = l$	$U\hat{n}_{i,\uparrow}\hat{n}_{i,\downarrow}$	Basic Hubbard term.
$i = j = k, l$	$A(\hat{c}_{i,\sigma}^\dagger\hat{c}_{j,\sigma} + \text{h.c.})(\hat{n}_{i,-\sigma} + \hat{n}_{j,-\sigma})$	Assisted hopping
	\vdots	
$i = l, k = j$	$V\hat{n}_{i,\sigma}\hat{n}_{j,\sigma'}$	NN interaction
$i = k, j = l$	$F\hat{c}_{i,\sigma}^\dagger\hat{c}_{j,\sigma'}^\dagger\hat{c}_{i,\sigma'}\hat{c}_{j,\sigma}$	NN exchange
$i = j, k = l$	$P\hat{c}_{i,\uparrow}^\dagger\hat{c}_{i,\downarrow}^\dagger\hat{c}_{j,\downarrow}\hat{c}_{j,\uparrow}$	Pair hopping

above half-filling is equivalent to removing an electron (i.e. adding a hole) below half-filling. More formally we can define a particle-hole transformation on lattice [52] as

$$\hat{c}_{i,\sigma} \rightarrow \hat{c}_{i,\sigma}^\dagger \quad \text{and} \quad \hat{c}_{i,\sigma}^\dagger \rightarrow \hat{c}_{i,\sigma}. \quad (3.24)$$

For a spin- $\frac{1}{2}$ particle in localized orbitals local number operator becomes

$$\hat{c}_{i,\sigma}^\dagger\hat{c}_{i,\sigma} = \hat{n}_{i,\sigma} \rightarrow 1 - \hat{n}_{i,\sigma}. \quad (3.25)$$

The notion of article-hole symmetry becomes very important when we discuss the Bogoliubov–de Gennes equations in the later chapters. The P -term promotes the delocalization of on-site singlet pairs, acting as a kinetic mechanism for composite bosons. It is negligible in strongly repulsive regimes but becomes important in some models of superconductivity. The exchange F -term, has a significant effect in that it favors ferromagnetic ordering.

4 Ferromagnetism

In this section we are going to consider two possible extensions of the tight-binding model giving rise to ferromagnetism (FM) and antiferromagnetism (AFM). The signature of these forms of magnetism is the existence of spontaneous ordering of the magnetic moments in a solid at a temperature below a critical temperature T^* . For ferromagnetism, $T^* = T_c$ is called the Curie temperature and for antiferromagnetism, $T^* = T_N$ is called the Neel temperature. Above the critical temperature, the spontaneous ordering vanishes and the material behaves like a normal paramagnet. These magnetic phenomena cannot be explained without quantum interactions [51, 53], as demonstrated by the Bohr-van Leeuwen theorem, stating that when classical statistical mechanics are applied consistently, the thermal average of the magnetization is always zero, i.e. in classical mechanics, there can be no magnetization [54].

This section develops the theoretical description of magnetism within lattice models. We start by discussing quantum exchange interactions and derive the mean-field Hamiltonian for ferromagnetism using the Hubbard model. We then analyze magnetic phases, introduce the Stoner criterion for ferromagnetic order, and conclude with a discussion of frustrated magnetism in geometrically constrained lattices.

4.1 Quantum exchange

The exchange interaction leading to ferromagnetism arises from an interplay between Coulomb forces and the Pauli principle. A given spin configuration restricts the range of possible spatial configurations. There is a significant energy cost associated with different spin configurations, because different spatial configurations can have significantly different energies [51, 55]. Within this framework, two categories of magnetic interaction exist. Potential exchange, driven by minimizing potential energy by reducing the wavefunction overlap. This leads to wavefunctions that are antisymmetric in space, where exchange favors electrons with symmetric spins – i.e., *ferromagnetic* ordering. On the other hand, kinetic exchange is driven by reducing the kinetic energy (reducing the gradients of wavefunctions), giving rise to symmetric superpositions of wavefunctions favoring antisymmetric spins – i.e., *antiferromagnetic* interactions.

Let's now look closer into ferromagnetism and consider the Coulomb potential,

$$V_{ee}(\mathbf{r} - \mathbf{r}') = \frac{e^2}{4\pi|\mathbf{r} - \mathbf{r}'|}. \quad (4.1)$$

Using the localized Wannier orbitals defined in Eq. (3.1) and restricting the interaction to on-site and nearest-neighbor terms, we substitute Eq. (4.1) into Eqs. (3.22) and (3.23) to obtain the extended Hubbard Hamiltonian. We identify two different types of contributions: direct (U, A, V, P -terms) and exchange interactions (F -term). Here we focus on the exchange term and write the exchange Hamiltonian H_e in lattice space,

$$H_e = \sum_{\langle i,j \rangle, \sigma, \sigma'} F_{ij} \hat{c}_{i,\sigma}^\dagger \hat{c}_{j,\sigma'}^\dagger \hat{c}_{i,\sigma'} \hat{c}_{j,\sigma}, \quad (4.2)$$

where

$$F_{ij} \equiv \frac{e^2}{8\pi} \int d^3r d^3r' |w(\mathbf{r} - \mathbf{r}_i)|^2 \frac{1}{|\mathbf{r} - \mathbf{r}'|} |w(\mathbf{r}' - \mathbf{r}_j)|^2. \quad (4.3)$$

The operators in the exchange term are normally ordered. We can rearrange them using anticommutation property of the fermionic ladder operators $\hat{c}_{j\sigma'}^\dagger \hat{c}_{i\sigma} = -\hat{c}_{i\sigma} \hat{c}_{j\sigma'}^\dagger + \delta_{ij}$. The exchange term in Equation (4.2) can be rewritten as

$$H_e = - \sum_{\langle i,j \rangle, \sigma, \sigma'} F_{ij} \hat{c}_{i,\sigma}^\dagger \hat{c}_{i,\sigma'} \hat{c}_{j,\sigma'}^\dagger \hat{c}_{j,\sigma} - \sum_{\langle i,j \rangle, \sigma, \sigma'} F_{ij} \hat{c}_{i,\sigma}^\dagger \hat{c}_{j,\sigma} \delta_{ij} \quad (4.4)$$

F_{ij} becomes divergent when $i = j$ and is thus unphysical. It corresponds to a constant shift in the Hamiltonian and can thus be neglected. The sum over spins can be expanded into

$$\begin{aligned} \sum_{\sigma,\sigma'} \hat{c}_{i,\sigma}^\dagger \hat{c}_{i,\sigma'} \hat{c}_{j,\sigma'}^\dagger \hat{c}_{j,\sigma}(\mathbf{r}') &= \frac{1}{2} \left(\hat{c}_{i,\uparrow}^\dagger \hat{c}_{i,\uparrow} + \hat{c}_{i,\downarrow}^\dagger \hat{c}_{i,\downarrow} \right) \left(\hat{c}_{j,\uparrow}^\dagger \hat{c}_{j,\uparrow} + \hat{c}_{j,\downarrow}^\dagger \hat{c}_{j,\downarrow} \right) \\ &\quad + \frac{1}{2} \left(\hat{c}_{i,\uparrow}^\dagger \hat{c}_{i,\uparrow} - \hat{c}_{i,\downarrow}^\dagger \hat{c}_{i,\downarrow} \right) \left(\hat{c}_{j,\uparrow}^\dagger \hat{c}_{j,\uparrow} - \hat{c}_{j,\downarrow}^\dagger \hat{c}_{j,\downarrow} \right) \\ &\quad + \hat{c}_{i,\uparrow}^\dagger \hat{c}_{i,\downarrow} \hat{c}_{j,\downarrow}^\dagger \hat{c}_{j,\uparrow} + \hat{c}_{i,\downarrow}^\dagger \hat{c}_{i,\uparrow} \hat{c}_{j,\uparrow}^\dagger \hat{c}_{j,\downarrow}. \end{aligned} \quad (4.5)$$

Note that the factors $\hat{c}_{i,\uparrow}^\dagger \hat{c}_{i,\uparrow} + \hat{c}_{i,\downarrow}^\dagger \hat{c}_{i,\downarrow}$ are just spin-independent number operators $\hat{c}_i^\dagger \hat{c}_i = \hat{n}_i$ and use the definitions in Eq. (2.17) in lattice space to write this expression compactly as:

$$\sum_{\sigma,\sigma'} \hat{c}_{i,\sigma}^\dagger \hat{c}_{i,\sigma'} \hat{c}_{j,\sigma'}^\dagger \hat{c}_{j,\sigma} = \frac{1}{2} \hat{n}_i \hat{n}_j + \frac{1}{2} \boldsymbol{\sigma}_i \cdot \boldsymbol{\sigma}_j, \quad (4.6)$$

where $\boldsymbol{\sigma}_i \cdot \boldsymbol{\sigma}_j = \sigma_i^3 \sigma_j^3 + \sigma_i^+ \sigma_j^- + \sigma_i^- \sigma_j^+$ where $\boldsymbol{\sigma}_i$ is the spin field operator. Since we are interested in the ferromagnetic interaction, we will focus on the behavior of electron spins and neglect the number density term. The exchange Hamiltonian can then be written as:

$$H_e = \frac{1}{2} \sum_{i,j} F_{ij} \boldsymbol{\sigma}_i \cdot \boldsymbol{\sigma}_j \quad (4.7)$$

Hence, in systems where this term is important, the ground state must be a state that maximizes the spin-field autocorrelation function $\langle \boldsymbol{\sigma}_i \cdot \boldsymbol{\sigma}_j \rangle$. This is known as *spontaneous magnetization*. The self-alignment of the spin field creates a macroscopic magnetic field due to the magnetic moment associated with each electron.

Equation (4.7) can be further simplified by using a mean-field approximation,

$$\boldsymbol{\sigma}_i = \langle \boldsymbol{\sigma}_i \rangle + \delta \boldsymbol{\sigma}_i, \quad (4.8)$$

where $\langle \boldsymbol{\sigma}_i \rangle$ is the mean field and $\delta \boldsymbol{\sigma}_i \equiv \boldsymbol{\sigma}_i - \langle \boldsymbol{\sigma}_i \rangle$ is the fluctuation field. As usual we assume that the spin field fluctuations are relatively weak, $|\delta \boldsymbol{\sigma}_i| \ll |\langle \boldsymbol{\sigma}_i \rangle|$, so we can discard terms of second order or higher in $\delta \boldsymbol{\sigma}_i$. Setting in Eq. (4.8) into Eq. (4.7) and ignoring terms constant with respect to the spin, the Hamiltonian is reduced to

$$H_e = - \sum_{i,j} F_{ij} \langle \boldsymbol{\sigma}_j \rangle \cdot \boldsymbol{\sigma}_i. \quad (4.9)$$

Re-expressing the spin field $\boldsymbol{\sigma}_i$ in terms of electron field operators $\hat{c}_{i\sigma}$ we obtain the following description of ferromagnetism in the mean-field theory:

$$H_M = - \sum_i \sum_{\sigma,\sigma'} \hat{c}_{i,\sigma}^\dagger [\mathbf{S} \cdot \mathbf{m}_i]_{\sigma,\sigma'} \hat{c}_{i,\sigma'}, \quad (4.10)$$

where \mathbf{S} is the Pauli vector (not to be confused with the spin field $\boldsymbol{\sigma}_i$) and we have defined the local exchange field at site i as $\mathbf{m}_i = \int d^3 r \mathbf{m}(\mathbf{r}) |w(\mathbf{r} - \mathbf{r}_i)|^2 \approx \mathbf{m}(\mathbf{r}_i)$. The last approximation follows from that the exchange field varies slowly with respect to the orbitals. The form of the Hamiltonian in Equation (4.10) is the one we later use in numerical simulations, since it allows us to precisely control the exchange field \mathbf{m}_i at each site and put it in the Hamiltonian for an arbitrary system. The exchange field in real space $\mathbf{m}(\mathbf{r})$ is given by

$$\mathbf{m}(\mathbf{r}) \equiv \frac{e^2}{8\pi} \int d^3 r' \frac{\langle \boldsymbol{\sigma}(\mathbf{r}') \rangle}{|\mathbf{r} - \mathbf{r}'|}. \quad (4.11)$$

Modeling a homogeneous bulk material, the exchange field can be assumed to be the same at all sites and can be chosen such that it only has a non-zero z -component [56]. With these simplifications, the exchange field Hamiltonian can be written as:

$$H_M = -m \sum_i \sum_{\sigma,\sigma'} \hat{c}_{i,\sigma}^\dagger \sigma_{\sigma,\sigma'}^3 \hat{c}_{i,\sigma'} = -m \sum_i (\hat{n}_{i,\uparrow} - \hat{n}_{i,\downarrow}) \quad (4.12)$$

Equation (4.12) shows the energy of spin-up electrons differs from the energy of spin-down electrons by the Zeeman energy $2m$ [57].

4.2 The single-band Hubbard model

In this section we only consider on-site electron-electron interactions, that is $V_{ijkl} = U\delta_{ij}\delta_{jk}\delta_{kl}$. Subsequently, the Hamiltonian in Eq. (3.22) is reduced to

$$\begin{aligned}\hat{H}_U &= \frac{1}{2}U \sum_{i,\sigma,\sigma'} \hat{c}_{i,\sigma}^\dagger \hat{c}_{i,\sigma'}^\dagger \hat{c}_{i,\sigma'} \hat{c}_{i,\sigma} \\ &= U \sum_i \hat{n}_{i,\uparrow} \hat{n}_{i,\downarrow},\end{aligned}\quad (4.13)$$

where in the second line we have used anticommutation of the fermionic ladder operators and the fact that fermion states can not be occupied by more than one electron (products of creation or annihilation operators with the same quantum numbers are zero). Hence, there are only non-zero terms when the spins σ and σ' are opposite.

We can now extend the tight-binding Hamiltonian from Eq. (3.4) and write

$$\hat{H} = -t \sum_{\langle i,j \rangle, \sigma} \hat{c}_{i,\sigma}^\dagger \hat{c}_{j,\sigma} + U \sum_i \hat{n}_{i,\uparrow} \hat{n}_{i,\downarrow} - \mu \sum_{i,\sigma} \hat{n}_{i,\sigma}, \quad (4.14)$$

also known as the half-filled Hubbard model Hamiltonian and is one of the most important and famous lattice models of interacting electrons [58].

This is called the half-filled case because the system can maximally contain two electrons per site (one for each spin) and thus a total electron number of $2N$. For $U \gg t$, the low-energy states can be found by first minimizing the interaction energy and then treating the kinetic energy as a perturbation. The interaction energy is minimized by placing exactly one electron on each site, but this does not necessarily say anything about the spin configuration of each electron. However, when the tight-binding hopping term is included, the magnitude of U in relation to t determines which magnetic phase is present. If neighboring electrons have opposite spins, an electron can hop (virtually) to a neighboring site and back; this virtual delocalization reduces the kinetic energy. If neighboring spins are parallel, such hopping is forbidden, because the intermediate step would violate the Pauli principle. Therefore, in this situation, an effective interaction is generated which favors neighboring electrons with opposite spin – i.e., AFM ordering [58]. However, the preference for antiferromagnetism in the half-filled case is not universal. Ferromagnetism can arise when the balance between kinetic and interaction energy changes. Despite its apparent simplicity, the Hubbard model cannot generally be solved exactly, except in the case of a one-dimensional system [59]. In our treatment of the model, we use the mean-field (Hartree–Fock) approximation of the Hubbard model [60, 61, 51]. So far, we have only considered magnetization from localized moments (electrons locked at a site). We will now consider itinerant electrons within a single-band lattice model, i.e., electrons not locked in a single site. We decompose the number operator into its mean value and a fluctuation term:

$$\hat{n}_{i,\sigma} = \langle n_\sigma \rangle + \delta\hat{n}_{i,\sigma}, \quad \delta\hat{n}_{i,\sigma} \equiv \hat{n}_{i,\sigma} - \langle n_\sigma \rangle. \quad (4.15)$$

Note that in the case of translational invariance in the system, the average number $\langle n \rangle$ is independent of the site. Inserting into Eq. (4.13), we get

$$\begin{aligned}\hat{H}_U &= U \sum_i [\langle n_\uparrow \rangle + \delta\hat{n}_{i,\uparrow}] [\langle n_\downarrow \rangle + \delta\hat{n}_{i,\downarrow}] \\ &\approx U \sum_i [\langle n_\uparrow \rangle \langle n_\downarrow \rangle + \delta\hat{n}_{i,\uparrow} \langle n_\downarrow \rangle + \delta\hat{n}_{i,\downarrow} \langle n_\uparrow \rangle] \\ &= U \sum_i [\hat{n}_{i,\uparrow} \langle n_\downarrow \rangle + \hat{n}_{i,\downarrow} \langle n_\uparrow \rangle - \langle n_\uparrow \rangle \langle n_\downarrow \rangle].\end{aligned}\quad (4.16)$$

In the second line we have assumed that the fluctuations are small, and thus their product can be neglected. To obtain the final expression we insert back the definition of $\delta\hat{n}_{i,\sigma}$. Equation (4.16) can be written compactly as:

$$\hat{H}_U^{MF} = U \sum_{i,\sigma} \hat{n}_{i,\sigma} \langle n_{-\sigma} \rangle - NU \langle n_\uparrow \rangle \langle n_\downarrow \rangle, \quad (4.17)$$

where the last term is constant and N is the total number of lattice sites. Note that the mean-field approximation has reduced the Hubbard term to a bilinear term with respect to the creation and annihilation operators. Equation (4.17) can also be written in \mathbf{k} -space by performing Fourier transformation (Equations (3.6) and (3.7)) to obtain

$$\hat{H}_U^{MF} = U \sum_{\mathbf{k},\sigma} \hat{n}_{\mathbf{k},\sigma} \langle n_{-\sigma} \rangle - NU \langle n_{\uparrow} \rangle \langle n_{\downarrow} \rangle. \quad (4.18)$$

4.3 Magnetic phases and the Stoner criterion

In order to find the ground-state energy for a given magnetic configuration, we employ a self-consistent scheme, because for a given spin σ , the energy depends on the mean occupation number of opposite spin, $\langle \hat{n}_{\sigma} \rangle$, which in turns depends on the eigenvectors of the energy matrix itself. Inserting Eq. (4.18) and ignoring the constant terms the Hamiltonian from Eq. (4.14) can be written compactly as

$$\hat{H}^{MF} = \sum_{\mathbf{k},\sigma} (\epsilon_{\mathbf{k}} + U \langle n_{-\sigma} \rangle) \hat{n}_{\mathbf{k},\sigma}, \quad (4.19)$$

with $\epsilon_{\mathbf{k}}$ the eigenvalues of the tight-binding Hamiltonian, Eq. (3.14).

Equation (3.16), together with the average occupation number per spin given by Eq. (3.16), define a self-consistency problem. We solve it by starting from an initial guess for the spin-dependent occupation numbers $\langle n_{\sigma} \rangle$, computing the corresponding energy spectrum (fig. 3), and using this updated spectrum to recalculate the average occupations. The final self-consistent solution, presented in fig. 3 (for the 2 dimensional case), shows that for small U/t the density of states remains spin-degenerate, indicating that electron-electron interactions are weak compared to the hopping term. For $U \gg t$, the degeneracy is lifted, splitting the DOS for spin-up and spin-down particles. Therefore, ferromagnetic ordering becomes energetically favorable. The splitting of different spin density of states is also the case when using the exchange field from the previous subsection rather than the Hubbard model. Indeed, the two models give rise to the same physics.

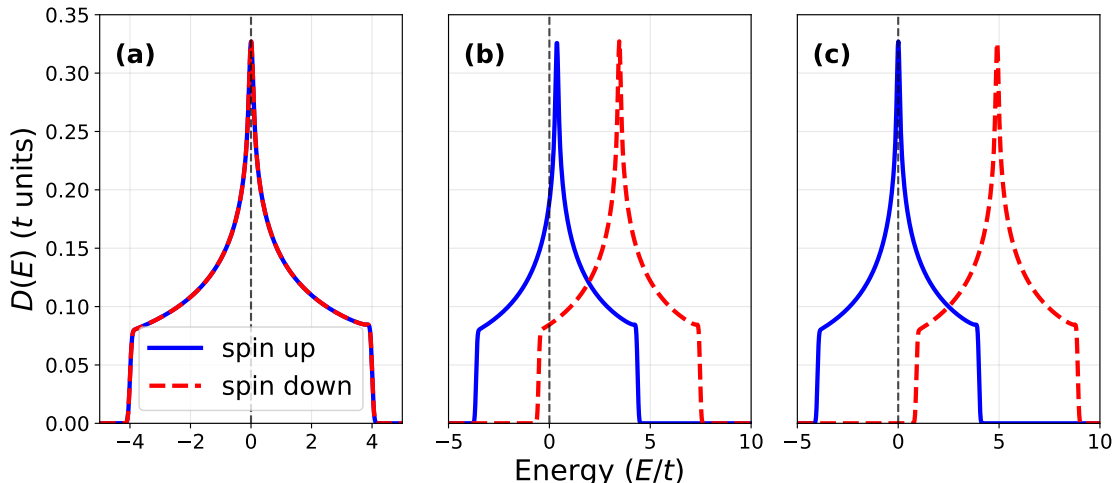


Figure 3: Density of states, $D(E)$, for the two-dimensional Hubbard model at zero temperature ($T = 0$) and zero chemical potential ($\mu/t = 0$). The plots distinguish spin-up (blue) and spin-down (red) electrons. Panel (a) shows the spin-degenerate density of states for the non-interacting case $U/t = 0$, corresponding to the paramagnetic (PM) phase. Panels (b) and (c) display results for interaction strengths $U/t = 8.518$ and $U/t = 10$, respectively, where ferromagnetic ordering emerges. The dashed black line marks the Fermi energy. A Gaussian with broadening $0.05t$ is used to numerically approximate Dirac's delta function.

At zero temperature, electrons occupy states up to the Fermi energy $E = 0$. In fig. 3(a), the spin-up and spin-down densities of states coincide, indicating the absence of spin polarization. As

the interaction strength increases, fig. 3(b) and fig. 3(c) show a clear splitting between the spin channels, leading to spin polarization.

For $U/t = 8.518$ (fig. 3(b)), most occupied states are spin-up, although a small number of spin-down states remain below the Fermi level. When the interaction reaches $U/t = 10$ (fig. 3(c)), all occupied states are spin-up, while the spin-down band is shifted entirely above the Fermi energy. Because electric transport is dominated by electrons near the Fermi level, such a *Fermi-level spin polarization* – i.e., an imbalance in the spin-up and spin-down densities of states at $E = 0$ – means that the resulting current carries a net spin. In the fully spin-polarized case shown in fig. 3(c), the system conducts electrons for one spin but acts as an insulator for the other, because no spin-down states are occupied or available without crossing an energy gap. A material exhibiting this behavior is known as a *half-metal* [62, 63].

To see more clearly where the transition occurs, let's take the approach of Keeling [51] and define the order parameter and total average number of particles as:

$$m \equiv \frac{1}{2} \langle n_\uparrow - n_\downarrow \rangle \quad \text{and} \quad n \equiv \langle n_\uparrow + n_\downarrow \rangle. \quad (4.20)$$

The full Hamiltonian from Eq. (4.14) can be then rewritten compactly in terms of these definitions

$$\hat{H}^{MF} = \sum_{\mathbf{k},\sigma} [\epsilon_{\mathbf{k}} - \sigma m U] \hat{n}_{\mathbf{k},\sigma} - NUm^2, \quad (4.21)$$

where the prefactor σ that takes value of $+1$ for spin-up and -1 for spin-down. It is clear that to have $m \neq 0$, the chemical potentials for n_\uparrow and n_\downarrow must be different. We consider a solution in which the chemical potentials for the two spins differ by δ ,

$$\langle n_\sigma \rangle = \int_0^{\epsilon_F + \sigma\delta} d\epsilon \rho(\epsilon) \simeq n_0 + \sigma \rho(\epsilon_F) \delta, \quad m = \rho(\epsilon_F) \delta. \quad (4.22)$$

Using self-consistency relation between m and δ we consider the total energy

$$\begin{aligned} \frac{E}{N} &= \sum_{\sigma} \int_0^{\epsilon_F + \sigma\delta} d\epsilon [\epsilon - \sigma m U] \rho(\epsilon) + U m^2 \\ &\simeq \text{const} + (\delta^2 - 2Um\delta) \rho(\epsilon_F) + Um^2 \\ &= \text{const} + \frac{m^2 [1 - U\rho(\epsilon_F)]}{\rho(\epsilon_F)}. \end{aligned} \quad (4.23)$$

We can see that, while for $U\rho(\epsilon_F) < 1$ the last term is positive and the energy is minimized when $m = 0$. However, if

$$U\rho(\epsilon_F) > 1 \quad (4.24)$$

the $m = 0$ state becomes unstable and is replaced with some $m \neq 0$. This is known as the *Stoner criterion* for the occurrence of ferromagnetic order in the Hubbard model. The Stoner criterion is sometimes also written as:

$$\frac{t}{U} < \rho(\epsilon_F)t. \quad (4.25)$$

The Stoner criterion, which sets a threshold for the interaction strength relative to the density of states at the Fermi level needed for the emergence of ferromagnetism. When this threshold is exceeded, spontaneous spin polarization becomes energetically favorable, marking a transition from a paramagnetic to a ferromagnetic phase.

4.4 Frustrated magnetism

As discussed earlier near half-filling and onsite repulsion $U \gg t$ we expect antiferromagnetic order. In geometrically frustrated magnets [64, 65], the magnetic spins are arranged on a crystal lattice where no ordered state can simultaneously satisfy all nearest-neighbor interactions, as shown in

fig. 4. In materials featuring some combination of geometric frustration, low-dimensionality, strong quantum fluctuations, competing interactions, and disorder the static antiferromagnetic order can be destroyed in favor of novel quantum ground states. Among these unique ground states are quantum spin liquids [66, 67], spin glasses [68], and spin ice [69].

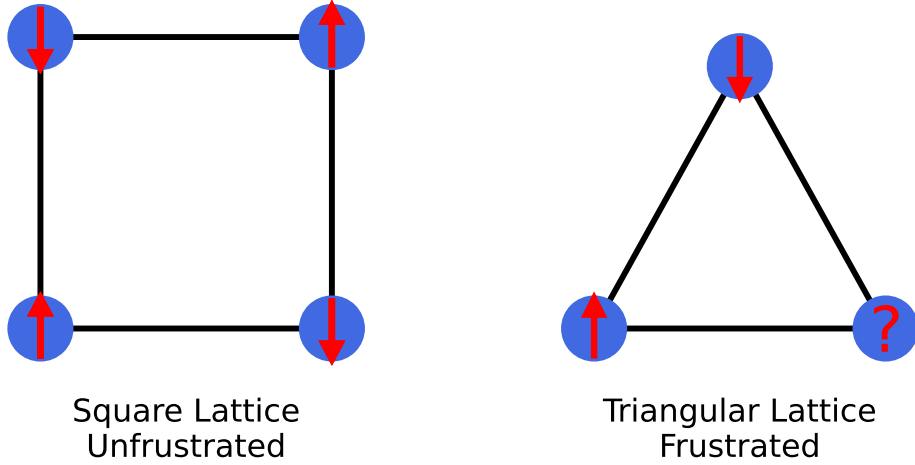


Figure 4: Illustration of geometric frustration. (Left) A square cell with antiferromagnetic NN interactions has a configuration in which all bonds are satisfied. (Right) A triangular cell with antiferromagnetic nearest-neighbor interactions cannot satisfy all bonds simultaneously, leading to frustration.

We will return to this notion in section 6, where we study the optimal spin configurations generated by the RKKY interaction for three symmetrically placed spins on a triangular lattice for different host materials.

5 Superconductivity

Conventional (*s*-wave) superconductors are well-described by the Bardeen–Cooper–Schrieffer (BCS) theory, which attributes the superconducting state to formation of Cooper pairs – bound pairs of electrons mediated by lattice vibrations (phonons). This pairing opens an energy gap in the electronic density of states, and leads to complete suppression of electrical resistance and expulsion of magnetic fields (the Meissner effect) [70]. Unconventional superconductors are materials that display superconductivity, but are not explained by BCS theory. The pairing in such superconductors may originate from some other mechanism than the electron–phonon interaction. Unconventional superconductors can also be defined as superconductors that have a pairing interaction not mediated by phonons or break additional symmetries to $U(1)$ [71, 72].

In this section, we formally introduce the BCS theory of superconductivity, alongside a discussion of unconventional superconductivity within the framework of the extended Hubbard model. We derive the Bogoliubov–de Gennes self-consistency equations for both conventional and unconventional pairing and solve them iteratively for on-site *s*-wave pairing characteristic of BCS superconductors. Key physical properties and behaviors of these systems are examined. Finally, concluding remarks are given and directions for future research are outlined.

5.1 Introduction to the Bardeen–Cooper–Schrieffer (BCS) theory

This section introduces the Bardeen–Cooper–Schrieffer (BCS) theory of superconductivity [4] following the book by Fossheim and Sudbø [70]. As a starting point, consider an electron moving in a lattice of positively charged ions; the electron’s negative charge slightly pulls the surrounding positively charged ions towards its path, producing a local lattice distortion. These “ripples” in the lattice then produce dipole moments that affect other electrons. The result is phonon-mediated scattering that produces a net attractive interaction. As Cooper has shown in his paper from 1956 [73], in the presence of an arbitrarily weak attractive interaction between two electrons near the Fermi level, a bound state known as a *Cooper pair* always forms.

Let us start by considering a Hamiltonian that describes the Coulomb interaction and phonon mediated scattering. Assuming that phonons are free bosons with well-defined energies $\omega_{\mathbf{q}}$, such a Hamiltonian can be formulated in momentum space using the second quantization formalism as:

$$\hat{H}_{\text{int}} = \sum_{\mathbf{k}, \mathbf{k}', \mathbf{q}, \sigma, \sigma'} \left(\frac{1}{4\pi} \frac{2\pi e^2}{\mathbf{q}^2} + \frac{2|\mathbf{M}_{\mathbf{q}}|^2 \omega_{\mathbf{q}}}{\omega^2 - \omega_{\mathbf{q}}^2} \right) \hat{c}_{\mathbf{k}+\mathbf{q}, \sigma}^\dagger \hat{c}_{\mathbf{k}'-\mathbf{q}, \sigma'}^\dagger \hat{c}_{\mathbf{k}, \sigma} \hat{c}_{\mathbf{k}', \sigma'}, \quad (5.1)$$

where ω is the transferred energy and $(\hat{c}_{\mathbf{q}, \sigma}^\dagger, \hat{c}_{\mathbf{q}, \sigma})$ are fermionic operators for electrons with momentum \mathbf{q} and spin σ . This is a two-step process where an electron in a state $|\mathbf{k}, \sigma\rangle$ is scattered into a state $|\mathbf{k} + \mathbf{q}, \sigma\rangle$, followed by another electron scattering from state $|\mathbf{k}', \sigma'\rangle$ to $|\mathbf{k}' - \mathbf{q}, \sigma'\rangle$. The interaction is mediated by a phonon transferring momentum \mathbf{q} between them. $\mathbf{M}_{\mathbf{q}}$ gives the strength of the electron–phonon interaction. It is inversely proportional to the ion mass and proportional to the momentum transfer \mathbf{q} . Equation (5.1) assumes that one phonon-mode dominates the coupling to the electrons. If that were not the case, we would have had to sum over phonon modes as well. Notice in Eq. (5.1) that the second term in the parentheses becomes negative for $\omega^2 < \omega_{\mathbf{q}}^2$, i.e., the interaction becomes attractive, and it formally diverges as $|\omega|$ approaches $\omega_{\mathbf{q}}$. It does not matter how small $|\mathbf{M}_{\mathbf{q}}|$ is, there will always be an energy range where the attractive interaction will overcome the Coulomb repulsion. We can, therefore, further simplify Eq. (5.1) by assuming that the sum in the parentheses is negative and constant (independent of ω) for a shell around the Fermi surface with thickness much smaller than the radius of the Fermi sphere, and zero otherwise. This simplification was first introduced in the original BCS paper on phonon-mediated superconductivity from 1957 [4]. The energy exchanged during the scattering is $\omega = \epsilon_{\mathbf{k}} - \epsilon_{\mathbf{k}+\mathbf{q}} = \epsilon'_{\mathbf{k}} - \epsilon'_{\mathbf{k}'-\mathbf{q}}$. All these energies must lie within an energy shell around the Fermi surface in order for the interaction to be attractive. This sets an extra restriction on the values of $(\mathbf{k}, \mathbf{k}', \mathbf{q})$. As shown in fig. 5, the initial momenta of the two electrons $(\mathbf{k}, \mathbf{k}')$ need to be equal in magnitude and opposite in direction in order to guarantee that both electrons stay inside the thin energy shell after scattering.

In addition to the restrictions on the allowed momenta, the electrons need to have opposite spins

in order to approach each other in space, due to the Pauli exclusion principle. Under these assumptions and restrictions, we set $\sigma' = -\sigma$, $\mathbf{k}' = -\mathbf{k}$ and redefine $\mathbf{k} + \mathbf{q} \rightarrow \mathbf{k}$, $\mathbf{k} \rightarrow \mathbf{k}'$. Rewriting Eq. (5.1), the full BCS Hamiltonian in the grand canonical ensemble is given by

$$\hat{H}_{\text{BCS}} = \sum_{\mathbf{k}, \sigma} \xi_{\mathbf{k}} \hat{c}_{\mathbf{k}, \sigma}^\dagger \hat{c}_{\mathbf{k}, \sigma} + \sum_{\mathbf{k}, \mathbf{k}', \sigma} V_{\mathbf{k}, \mathbf{k}'} \hat{c}_{\mathbf{k}, \sigma}^\dagger \hat{c}_{-\mathbf{k}, -\sigma} \hat{c}_{-\mathbf{k}', -\sigma} \hat{c}_{\mathbf{k}', \sigma}, \quad (5.2)$$

where $\xi_{\mathbf{k}} \equiv \epsilon_{\mathbf{k}} - \mu$. $\epsilon_{\mathbf{k}}$ is the energy of a free electron⁴ with momentum \mathbf{k} , μ is the chemical potential of the system, $V_{\mathbf{k}, \mathbf{k}'}$ is an attractive two-particle scattering matrix element which is operative if both \mathbf{k} and \mathbf{k}' are within a thin shell around the Fermi-surface.

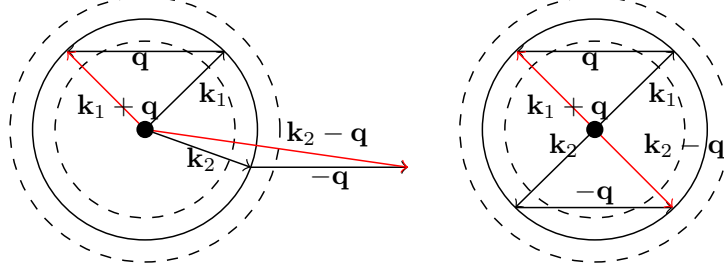


Figure 5: Phase-space of two-particle scattering within a thin shell of the Fermi-surface. On the left side the states have initial momenta $\mathbf{k} \neq -\mathbf{k}'$. On the right image the initial states have opposite momenta $\mathbf{k} = -\mathbf{k}'$. This figure is inspired by Fossheim and Sudbø [70].

Equation (5.2) can be further simplified using mean-field theory. The justification for applying mean-field theory will not be discussed here, the reader can refer to more general books and reviews on superconductivity and condensed matter field theory [41, 70, 72] for a more detailed explanation. It is worth to mention that this approximation is reasonable in our system but should be treated with much care in the case of the existence of an additional spin-orbit coupling [74]. We begin by defining the expectation values and fluctuations for the Cooper pair ladder operators:

$$b_{\mathbf{k}} = \langle \hat{c}_{-\mathbf{k}, \downarrow} \hat{c}_{\mathbf{k}, \uparrow} \rangle, \quad b_{\mathbf{k}}^\dagger = \langle \hat{c}_{\mathbf{k}, \uparrow}^\dagger \hat{c}_{-\mathbf{k}, \downarrow}^\dagger \rangle \quad (5.3)$$

$$\hat{\delta}b_{\mathbf{k}} = \hat{c}_{-\mathbf{k}, \downarrow} \hat{c}_{\mathbf{k}, \uparrow} - b_{\mathbf{k}}, \quad \hat{\delta}b_{\mathbf{k}}^\dagger = \hat{c}_{\mathbf{k}, \uparrow}^\dagger \hat{c}_{-\mathbf{k}, \downarrow}^\dagger - b_{\mathbf{k}}^\dagger. \quad (5.4)$$

In mean-field theory the fluctuations $\hat{\delta}b_{\mathbf{k}}$ are assumed to be very small compared to the mean field $b_{\mathbf{k}}$. Under this assumption, higher than linear order terms in $\hat{\delta}b_{\mathbf{k}}$ can be neglected. Eq. (5.2) can then be rewritten as an effective one-body Hamiltonian,

$$\hat{H}_{\text{BCS}}^{\text{MF}} = \sum_{\mathbf{k}, \sigma} \xi_{\mathbf{k}} \hat{c}_{\mathbf{k}, \sigma}^\dagger \hat{c}_{\mathbf{k}, \sigma} - \sum_{\mathbf{k}} \left(\Delta_{\mathbf{k}}^\dagger \hat{c}_{-\mathbf{k}, \downarrow} \hat{c}_{\mathbf{k}, \uparrow} + \Delta_{\mathbf{k}} \hat{c}_{\mathbf{k}, \uparrow}^\dagger \hat{c}_{-\mathbf{k}, \downarrow}^\dagger \right), \quad (5.5)$$

where we have omitted the term $-b_{\mathbf{k}}^\dagger \Delta_{\mathbf{k}}$ since it does not contain $\hat{c}_{\mathbf{k}}^\dagger$ or $\hat{c}_{\mathbf{k}}$. $\Delta_{\mathbf{k}}$ is called the superconducting *gap parameter* and is defined as

$$\Delta_{\mathbf{k}} \equiv - \sum_{\mathbf{k}'} V_{\mathbf{k}, \mathbf{k}'} b_{\mathbf{k}'} \quad \text{and} \quad \Delta_{\mathbf{k}'}^* \equiv - \sum_{\mathbf{k}} V_{\mathbf{k}, \mathbf{k}'} b_{\mathbf{k}}^\dagger. \quad (5.6)$$

We introduce new fermionic ladder operators $(\hat{\gamma}_{\mathbf{k}}^\dagger, \hat{\gamma}_{\mathbf{k}})$ and $(\hat{\eta}_{\mathbf{k}}^\dagger, \hat{\eta}_{\mathbf{k}})$ by performing a Bogoliubov transformation (a rotation in Nambu space by an angle $\theta_{\mathbf{k}}$) on the original electronic creation and annihilation operators:

$$\begin{aligned} \hat{c}_{\mathbf{k}, \uparrow} &= \cos(\theta_{\mathbf{k}}) \hat{\eta}_{\mathbf{k}} - \sin(\theta_{\mathbf{k}}) \hat{\gamma}_{\mathbf{k}}, \\ \hat{c}_{-\mathbf{k}, \downarrow}^\dagger &= \sin(\theta_{\mathbf{k}}) \hat{\eta}_{\mathbf{k}} + \cos(\theta_{\mathbf{k}}) \hat{\gamma}_{\mathbf{k}}. \end{aligned} \quad (5.7)$$

⁴ In the free electron model, the electron energy is given by $E = \mathbf{k}^2/2m_e$, assuming electrons move as free particles. In real conductors, the periodic lattice potential modifies this dispersion, leading to energy bands. Near the conduction band minimum, the relation can often be approximated by $E(\mathbf{k}) \approx E_c + \mathbf{k}^2/2m^*$, where m^* is the effective mass determined by the band curvature.

We can now pick $\theta_{\mathbf{k}}$ so that the transformed Hamiltonian $\hat{H}(\mathbf{k}) = \hat{U}^\dagger \hat{H}_{\text{BCS}}^{\text{MF}}(\mathbf{k}) \hat{U}$ is diagonal. It can be shown that the rotation angle that makes the off-diagonal terms disappear must satisfy $\tan(2\theta) = -\Delta_{\mathbf{k}}/\xi_{\mathbf{k}}$ [70]. For such values of $\theta_{\mathbf{k}}$ we have

$$\cos^2(\theta_{\mathbf{k}}) \equiv u_{\mathbf{k}}^2 = \frac{1}{2} \left[1 + \frac{\xi_{\mathbf{k}}}{E_{\mathbf{k}}} \right], \quad (5.8)$$

$$\sin^2(\theta_{\mathbf{k}}) \equiv v_{\mathbf{k}}^2 = \frac{1}{2} \left[1 - \frac{\xi_{\mathbf{k}}}{E_{\mathbf{k}}} \right]. \quad (5.9)$$

where

$$E_{\mathbf{k}} \equiv \sqrt{\xi_{\mathbf{k}}^2 + |\Delta_{\mathbf{k}}|^2}. \quad (5.10)$$

The effect of the gap on the dispersion is illustrated in fig. 6, where the normal-state parabola ($\Delta = 0$) is compared to the gapped quasiparticle branches for finite Δ .

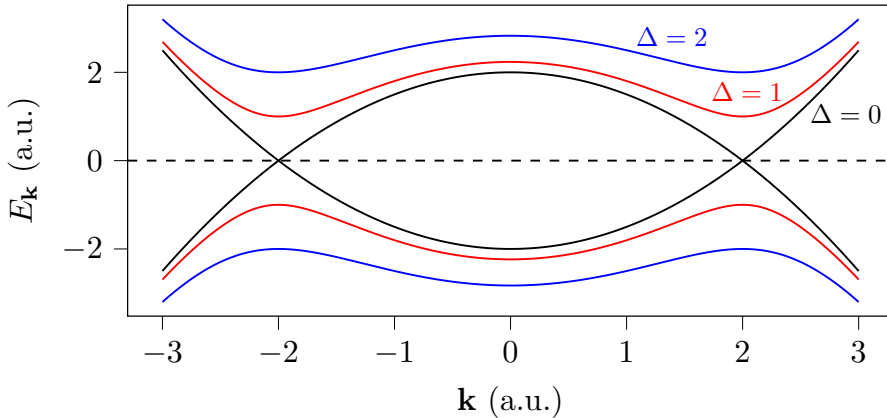


Figure 6: Bogoliubov quasiparticle dispersion $E_{\mathbf{k}}$ for free electrons with chemical potential $\mu = 2$ in the normal state ($\Delta = 0$, black) and in the superconducting state with finite s -wave gaps $\Delta = 1$ (red) and $\Delta = 2$ (blue). Both positive and negative energy branches are shown, corresponding to particle-like and hole-like excitations. A superconducting excitation gap of size 2Δ forms around the Fermi level, showing the effect of superconductivity on the quasiparticle dispersion.

Reintroducing $\Delta_{\mathbf{k}} b_{\mathbf{k}}^\dagger$ into Eq. (5.5), the equation can now be written as a simple free fermion quasiparticle gas Hamiltonian:

$$\hat{H} = \sum_{\mathbf{k},\sigma} (\xi_{\mathbf{k}} + \Delta_{\mathbf{k}} b_{\mathbf{k}}^\dagger) + \sum_{\mathbf{k}} E_{\mathbf{k}} (\hat{n}_{\mathbf{k}}^\dagger \hat{n}_{\mathbf{k}} - \hat{\gamma}_{\mathbf{k}}^\dagger \hat{\gamma}_{\mathbf{k}}). \quad (5.11)$$

For simplicity we can assume that the interaction term and the gap is independent of the momentum \mathbf{k} , i.e., $\Delta_{\mathbf{k}} = \Delta$ and $V_{\mathbf{k},\mathbf{k}'} = V$. This is a reasonable assumption in the context of conventional superconductivity⁵. Inverting the definitions in Eq. (5.6) we can see that

$$\Delta_{\mathbf{k}} b_{\mathbf{k}}^\dagger = \frac{|\Delta|^2}{V}. \quad (5.12)$$

Even though Eq. (5.12) here is derived in the context of conventional (s -wave) superconductors, it can be shown that the assumptions above are not absolutely necessary and the relation $\Delta_{\mathbf{k}} b_{\mathbf{k}}^\dagger \sim |\Delta_{\mathbf{k}}|^2$ still holds in other cases.

The quasiparticle excitation energies can be identified in Eq. (5.11) as $(E_{\mathbf{k}}, -E_{\mathbf{k}})$ for the two species of fermions. Rather than having spin-up electrons and spin-down electrons as our degrees of freedom, we now have two distinct linear combinations of particle-hole spin-singlets as our relevant degrees of freedom. Thus, the total number of degrees of freedom is conserved.

⁵ Even if the attractive interaction $V_{\mathbf{k},\mathbf{k}'}$ is not constant, conventional superconductivity can still occur, provided the interaction remains isotropic, i.e., depends only on the magnitudes of $|\mathbf{k}|$ and $|\mathbf{k}'|$ and not their relative orientation. In such case, the gap $\Delta_{\mathbf{k}}$ may vary with momentum magnitude but keeps the s -wave symmetry.

The Bogoliubov transformation described above serves as an analytical tool for diagonalizing the Hamiltonian and understanding its implications. In practice, we will herein use Eq. (5.5) instead, and the diagonalization is then carried out numerically.

5.2 Critical temperature T_c and the energy gap Δ in the BCS theory

The Hamiltonian Eq. (5.11) has the form of a free fermion gas. Applying a similar treatment as Ref. [70], the partition function in the grand canonical ensemble can be written as:

$$\mathcal{Z} = e^{-H_0/T} \prod_{\mathbf{k}} \left(1 + e^{-E_{\mathbf{k}}/T}\right) \left(1 + e^{E_{\mathbf{k}}/T}\right) = e^{-\Omega/T}, \quad (5.13)$$

$$H_0 \equiv \sum_{\mathbf{k}} \left(\xi_{\mathbf{k}} + \Delta_{\mathbf{k}} b_{\mathbf{k}}^{\dagger} \right). \quad (5.14)$$

It follows the grand potential Ω of the system is given by

$$\Omega = H_0 - T \sum_{\mathbf{k}} \left[\ln \left(1 + e^{-E_{\mathbf{k}}/T}\right) + \ln \left(1 + e^{E_{\mathbf{k}}/T}\right) \right], \quad (5.15)$$

which has the form of a pure mean-field term plus the contribution from a two-component effective non-interacting fermion gas. At zero temperature this equation becomes

$$\Omega = \sum_{\mathbf{k}} \left(\xi_{\mathbf{k}} + \Delta_{\mathbf{k}} b_{\mathbf{k}}^{\dagger} - E_{\mathbf{k}} \right). \quad (5.16)$$

The gap in this case can be thought of as a variational parameter, determined by minimizing the free energy with respect to variations in Δ_k . Since the grand potential is $\Omega = F - \mu \langle N \rangle$, minimizing the free energy is the same as as minimizing the grand potential [45]. As shown in Ref. [70], this is done by having the gap-parameter satisfy

$$\Delta_{\mathbf{k}} = - \sum_{\mathbf{k}'} V_{\mathbf{k}\mathbf{k}'} \Delta_{\mathbf{k}'} \frac{\tanh(E_{\mathbf{k}'}/2T)}{2E_{\mathbf{k}}}. \quad (5.17)$$

For an isotropic s -wave pairing, this equation becomes:

$$1 = V \sum_{\mathbf{k}'} \frac{\tanh(E_{\mathbf{k}'}/2T)}{2E_{\mathbf{k}}}. \quad (5.18)$$

This equation is easy to solve for $T = T_c$ and $T = 0$, where T_c denotes the critical temperature at which the system undergoes a transition between the superconducting and normal states. For phonon-assisted superconductivity, the pairs of wavenumbers $(\mathbf{k}, \mathbf{k}')$ lie in a thin shell around the Fermi surface of thickness ω_D , where ω_D is the Debye frequency. The \mathbf{k} -sum can be replaced by an energy integral by introducing the density of states $D(\epsilon)$. Further, if $D(\epsilon)$ varies slowly near the Fermi-surface, we can replace $D(\epsilon)$ with $D(0)$ [75]. For $T \rightarrow T_c$ we obtain the following equation

$$1 = VD(0) \int_0^{\omega_D} d\epsilon \frac{\tanh(\epsilon/2T)}{\epsilon}. \quad (5.19)$$

In the weak coupling limit $VD(0) \ll 1$ it can be shown [70] that this integral simplifies to

$$1 = VD(0) \ln \left(\frac{2e^{\gamma} \omega_D}{\pi T} \right), \quad (5.20)$$

where $\gamma = 0.5772\dots$ is the Euler-Mascheroni constant. Solving this equation gives

$$T_c = \frac{2e^{\gamma}}{\pi} \omega_D e^{-\frac{1}{VD(0)}}. \quad (5.21)$$

For the other solution, $T = 0$, the gap equation becomes

$$1 = VD(0) \sinh^{-1} \left(\frac{\omega_D}{\Delta} \right). \quad (5.22)$$

For this equation to be solvable in the weak coupling $VD(0) \ll 1$, we need that $\omega_D/\Delta \gg 1$. Hence $\sinh^{-1}(\omega_D/\Delta) \approx \ln(2\omega_D/\Delta)$, giving the following solution:

$$\Delta(T=0) = 2\omega_D e^{-\frac{1}{VD(0)}}. \quad (5.23)$$

Note that the ratio between $\Delta(T=0)/T_c$ is a universal amplitude ratio for BCS superconductors where all the material-dependent quantities cancel out. This was already noted by Bardeen, Cooper and Schrieffer and is referred to as the *BCS ratio* [4]:

$$r_{\text{BCS}} = \frac{2\Delta(T=0)}{T_c} = \frac{2\pi}{e^\gamma} \approx 3.52$$

(5.24)

5.3 Mean-field extended Hubbard model of superconductivity

The BCS theory considered so far, gives a superconducting gap structure that is isotropic in \mathbf{k} -space. In the extended Hubbard model, the conventional *s*-wave superconducting order parameter is obtained if an on-site opposite-spin attractive interaction term is used (the *U*-term in table 1 with $U < 0$). As a starting point to model unconventional superconductivity, i.e., to allow for more complex gap structures, we should consider the nearest-neighbor Hubbard interaction term given by the *V*-term in table 1. As it is shown later in this chapter, even without imposing symmetry constraints, the model allows us to construct superconducting order parameters with *p*-wave and *d*-wave symmetry properties [72, 76]. When discussing the different types of superconductivity, it is convenient to split the nearest-neighbor interaction term to same spin and opposite spin contributions, similar to what is done in Terrade's PhD thesis [74]:

$$\hat{H}_{VV'} = - \sum_{\langle i,j \rangle} V_i (\hat{n}_{i,\uparrow} \hat{n}_{j,\downarrow} + \hat{n}_{i,\downarrow} \hat{n}_{j,\uparrow}) - \sum_{\langle i,j \rangle} V'_i (\hat{n}_{i,\uparrow} \hat{n}_{j,\uparrow} + \hat{n}_{i,\downarrow} \hat{n}_{j,\downarrow}) = -\hat{H}_V - \hat{H}_{V'}, \quad (5.25)$$

where V_i is the nearest-neighbor attraction between electrons with opposite spin on the site i and V'_i , that of same spin electrons on the site i . We can assume that $V_i = V$ and $V'_i = V'$ are independent of the lattice site inside the superconducting region. As before, a Hartree-Fock mean field approximation can be used to decouple the quartic terms in Eq. (5.25). Defining the correlation functions [74] as:

$$F_{i,j}^{\sigma\sigma'} = \langle \hat{c}_{i,\sigma} \hat{c}_{j,\sigma'} \rangle, \quad (5.26)$$

leads to the following Hamiltonian operator:

$$\hat{H}_{VV'}^{MF} = -V \sum_{\langle i,j \rangle} \left(F_{i,j}^{\uparrow\downarrow} \hat{c}_{j,\downarrow}^\dagger \hat{c}_{i,\uparrow}^\dagger + F_{i,j}^{\downarrow\uparrow} \hat{c}_{j,\uparrow}^\dagger \hat{c}_{i,\downarrow}^\dagger + \text{h.c.} \right) - V' \sum_{\langle i,j \rangle, \sigma} \left(F_{i,j}^{\sigma\sigma} \hat{c}_{j,\sigma}^\dagger \hat{c}_{i,\sigma}^\dagger + \text{h.c.} \right), \quad (5.27)$$

where we have dropped the constant energy offset coming from the Hartree-Fock approximation. Note that it can be shown [74] terms including $F_{i,j}^{\uparrow\downarrow}$ and $F_{i,j}^{\downarrow\uparrow}$ are equivalent, such that

$$\sum_{\langle i,j \rangle} V_i F_{i,j}^{\uparrow\downarrow} \hat{c}_{j,\downarrow}^\dagger \hat{c}_{i,\uparrow}^\dagger = \sum_{\langle i,j \rangle} V_j F_{i,j}^{\downarrow\uparrow} \hat{c}_{j,\uparrow}^\dagger \hat{c}_{i,\downarrow}^\dagger. \quad (5.28)$$

Moreover, for $V_i = V_j \equiv V$, first sum in Eq. (5.27) can then be simplified by keeping only the $\uparrow\downarrow$ channel explicitly:

$$V \sum_{\langle i,j \rangle} \left(F_{i,j}^{\uparrow\downarrow} \hat{c}_{j,\downarrow}^\dagger \hat{c}_{i,\uparrow}^\dagger + F_{i,j}^{\downarrow\uparrow} \hat{c}_{j,\uparrow}^\dagger \hat{c}_{i,\downarrow}^\dagger + \text{h.c.} \right) = 2V \sum_{\langle i,j \rangle} \left(F_{i,j}^{\uparrow\downarrow} \hat{c}_{j,\downarrow}^\dagger \hat{c}_{i,\uparrow}^\dagger + \text{h.c.} \right). \quad (5.29)$$

Further in text we will reabsorb the numerical factor of into the interaction strength by $V \rightarrow 2V$. This allows us to introduce the following notation for simplicity:

$$F_i^{\pm x} = F_{i,i\pm\hat{x}}^{\uparrow\downarrow}, \quad F_i^{\pm y} = F_{i,i\pm\hat{y}}^{\uparrow\downarrow}, \quad (5.30)$$

$$F_{i,\sigma\sigma}^{\pm x} = F_{i,i\pm\hat{x}}^{\sigma\sigma}, \quad F_{i,\sigma\sigma}^{\pm y} = F_{i,i\pm\hat{y}}^{\sigma\sigma}, \quad (5.31)$$

where \hat{x} and \hat{y} indicates the displacement by one lattice spacing along the x and y -direction. More explicitly the the nearest neighbor of site i in the $+\hat{x}$ direction is the site j whose position satisfies $\mathbf{R}_j = \mathbf{R}_i + a\hat{\mathbf{x}}$, where $\hat{\mathbf{x}}$ is the unit vector along the x -axis. We then write this relation in the compact form $j = i + \hat{x}$, and correspondingly use subscripts like $F_{i,i+\hat{x}}^{\uparrow\downarrow}$. This is a slight abuse of notation that is very common in the literature, the site label i is a discrete index, whereas \hat{x} is a vector in real space. The meaning is that $i + \hat{x}$ is “the site obtained by moving one lattice spacing from i in the $+x$ direction”, and similarly for $i - \hat{x}$, $i \pm \hat{y}$, etc. In numerical works we typically choose units where the lattice constant is set to unity.

5.4 Pairing symmetries and superconducting gap beyond on-site s -wave

In order to describe the superconducting phase of the bulk system, we define the superconducting order parameters that contain the spin and momentum symmetry of the energy gap known for the extended s -wave, d -wave, p_x -wave and p_y -wave superconductors. They are generally defined as

$$\Delta_0(i) = UF_{ii}^{\uparrow\downarrow}, \quad (5.32)$$

$$\Delta_s(i) = V \left(F_i^{+\hat{x}(S)} + F_i^{-\hat{x}(S)} + F_i^{+\hat{y}(S)} + F_i^{-\hat{y}(S)} \right) / 4, \quad (5.33)$$

$$\Delta_{d_{x^2-y^2}}(i) = V \left(F_i^{+\hat{x}(S)} + F_i^{-\hat{x}(S)} - F_i^{+\hat{y}(S)} - F_i^{-\hat{y}(S)} \right) / 4, \quad (5.34)$$

$$\Delta_{p_x}(i) = V \left(F_i^{+\hat{x}(T)} - F_i^{-\hat{x}(T)} \right) / 2, \quad (5.35)$$

$$\Delta_{p_y}(i) = V \left(F_i^{+\hat{y}(T)} - F_i^{-\hat{y}(T)} \right) / 2, \quad (5.36)$$

$$\Delta_{p_x}^{\sigma\sigma}(i) = V' \left(F_{i,\sigma\sigma}^{+\hat{x}(T)} - F_{i,\sigma\sigma}^{-\hat{x}(T)} \right) / 2, \quad (5.37)$$

$$\Delta_{p_y}^{\sigma\sigma}(i) = V' \left(F_{i,\sigma\sigma}^{+\hat{y}(T)} - F_{i,\sigma\sigma}^{-\hat{y}(T)} \right) / 2. \quad (5.38)$$

Here Δ_s is the extended s -wave pairing amplitude, constructed from nearest-neighbor bonds. The superscripts correspond to spin-singlet (S) and spin-triplet (T) symmetries. The correlators are then defined as

$$F_{ij}^{(S)} = \frac{F_{ij} + F_{ji}}{2} \quad \text{and} \quad F_{ij}^{(T)} = \frac{F_{ij} - F_{ji}}{2} \quad (5.39)$$

In contrast Δ_0 with $F_{ii}^{\uparrow\downarrow} = \langle \hat{c}_{i,\uparrow} \hat{c}_{i,\downarrow} \rangle$ is the conventional s -wave gap that arises from an on-site attractive interaction U (as discussed in the previous section). We include Δ_0 here for completeness.

Note that the $\{s, p_x, p_y, d_{x^2-y^2}\}$ orders are the natural spatial symmetries in a square lattice because they transform according to the irreducible representations of C_{4v} and are compatible with the fourfold rotation and mirror symmetries of the lattice. On different structures, other pairing symmetries may be relevant; for example f -wave pairing due to the valley-sublattice structure [77] or presumably g -wave in Sr_2RuO_4 as suggested by some studies [78]. In this section we focus on square lattices where $\{s, p_x, p_y, d_{x^2-y^2}\}$ are expected to be the relevant orders.

The symmetry constraints can be described using the two-fermion correlation function [79]

$$F_{\alpha\beta}(\mathbf{r}, t) \equiv \langle \mathcal{T} c_\alpha(\mathbf{r}, t) c_\beta(\mathbf{0}, 0) \rangle \quad (5.40)$$

Here \mathcal{T} is the time-ordering operator, \mathbf{r} is the *relative* spatial coordinate and t is the *relative* time coordinate, α and β are the spin indices of the electrons in the Cooper pair. Due to the Fermi statistics of the creation and annihilation operators we require that exchanging the two electrons of the Cooper pair must be overall antisymmetric. This sets symmetry constraints on the permutation properties of the two operators in the pairing state, as pointed out by Berezinskii [80]. The exchange can be factorized into separate permutations acting on different degrees of freedom of the pair: *relative* coordinate permutation P^* , which sends $\mathbf{r} \rightarrow -\mathbf{r}$; time coordinate permutation T^* , sending the *relative* time $t \rightarrow -t$; spin exchange S , given as $S F_{\alpha\beta}(\mathbf{r}, t) S^{-1} = F_{\beta\alpha}(\mathbf{r}, t)$. In multiband systems one must also include orbital (band) exchange O , but in the present single-band treatment it is trivial $O = +1$ and will be omitted. It can then be shown [80] that applying these permutation operations on the pair correlations $S P^* T^* F_{\alpha\beta}(\mathbf{r}, t) = -F_{\alpha\beta}(\mathbf{r}, t)$. Since $P^{*2} = T^{*2} = S^2 = 1$, there

are only two possibilities for each of the operations. This leads to four possible states as listed in table 2.

Table 2: Symmetry properties of the anomalous two-fermion correlator. Adapted from Ref. [79].

Spin (S)	Parity (P^*)	Frequency (T^*)	Total	Examples
Odd	Even	Even- ω	Odd	BCS spin-singlet s wave; Al, Nb [4]
Even	Odd	Even- ω	Odd	Spin-triplet p -wave; UTe ₂ [15]
Even	Even	Odd- ω	Odd	MgB ₂ in applied magnetic field [81]
Odd	Odd	Odd- ω	Odd	Predicted in multi-band superconductors[82]

The first two rows in table 2 are the usual even-frequency singlet-even and triplet-odd states (conventional singlet s/d -wave and triplet p -wave). The last two rows are odd-frequency superconducting states: even-parity triplet and odd-parity singlet. For an odd-frequency Cooper pair the two-particle correlator is odd under interchange of the time arguments, i.e., $t \rightarrow -t$; therefore the electron pairs seem uncorrelated at if looked at simultaneously, but correlate with a finite time retardation. The wave function, however, can still be time independent or static when expressed in terms of the absolute time $t_1 + t_2$. Magnetic proximity effects break time-reversal symmetry and thereby enable mixing between even- and odd-frequency pairing channels. This is why magnetic proximity structures are particularly effective generators of odd-frequency superconductivity. Odd-frequency pairing can also emerge in the absence of magnetism, for example in a superconductor–normal-metal junction where translational symmetry is broken at the interface [83]. Consider a singlet BCS superconductor–normal-metal bi-layer: the loss of translational invariance at the interface means that momentum is not conserved and thereby generates odd-parity pairing components. At the same time, the system remains spin-degenerate and there is no mechanism to convert singlet pairs into triplet pairs. Consequently, the induced pairing is odd in both spatial parity and spin; according to table 2, it must therefore also be odd in frequency. For extensive review on the topic the reader can refer to Refs. [79, 84].

As in the BCS theory, it is analytically convenient to transform the Hamiltonian to \mathbf{k} -space. We assume bulk system and adopt periodic boundary conditions. Then using the Fourier transformations of the creation and annihilation operators, Eqs. (3.6) and (3.7), and inserting these into the mean-field Hamiltonian Eq. (5.27) the first term becomes:

$$\begin{aligned}
H_V^{MF} &= V \sum_{\langle i,j \rangle} \left(F_{i,j}^{\uparrow\downarrow} \hat{c}_{j,\downarrow}^\dagger \hat{c}_{i,\uparrow}^\dagger + \text{h.c.} \right) \\
&= V \sum_i \left(F_i^{+\hat{x}} \hat{c}_{i+\hat{x},\downarrow}^\dagger \hat{c}_{i,\uparrow}^\dagger + F_i^{-\hat{x}} \hat{c}_{i-\hat{x},\downarrow}^\dagger \hat{c}_{i,\uparrow}^\dagger + F_i^{+\hat{y}} \hat{c}_{i+\hat{y},\downarrow}^\dagger \hat{c}_{i,\uparrow}^\dagger + F_i^{-\hat{y}} \hat{c}_{i-\hat{y},\downarrow}^\dagger \hat{c}_{i,\uparrow}^\dagger + \text{h.c.} \right) \\
&= V \sum_{\mathbf{k}} \left[(F^{+\hat{x}} e^{-ik_x} + F^{-\hat{x}} e^{ik_x} + F^{+\hat{y}} e^{-ik_y} + F^{-\hat{y}} e^{ik_y}) \hat{c}_{\mathbf{k},\downarrow}^\dagger \hat{c}_{-\mathbf{k},\uparrow}^\dagger + \text{h.c.} \right], \tag{5.41}
\end{aligned}$$

where we have used translational invariance of the system and Eq. (3.9) is used leading to $\mathbf{k}' = -\mathbf{k}$. The same can be done to the second term in Eq. (5.27),

$$\begin{aligned}
H_{V'}^{MF} &= V' \sum_{\langle i,j \rangle, \sigma} \left(F_{i,j}^{\sigma\sigma} \hat{c}_{j,\sigma}^\dagger \hat{c}_{i,\sigma}^\dagger + \text{h.c.} \right) \\
&= V' \sum_{\mathbf{k}, \sigma} \left[(F_{\sigma\sigma}^{+\hat{x}} e^{-ik_x} + F_{\sigma\sigma}^{-\hat{x}} e^{ik_x} + F_{\sigma\sigma}^{+\hat{y}} e^{-ik_y} + F_{\sigma\sigma}^{-\hat{y}} e^{ik_y}) \hat{c}_{\mathbf{k},\sigma}^\dagger \hat{c}_{-\mathbf{k},\sigma}^\dagger + \text{h.c.} \right] \\
&= V' \sum_{\mathbf{k}, \sigma} \left[F_{\mathbf{k},\sigma} \hat{c}_{\mathbf{k},\sigma}^\dagger \hat{c}_{-\mathbf{k},\sigma}^\dagger + \text{h.c.} \right], \tag{5.42}
\end{aligned}$$

where we have defined

$$F_{\mathbf{k},\sigma} = -2i [F_{\sigma\sigma}^{+\hat{x}} \sin(k_x) + F_{\sigma\sigma}^{+\hat{y}} \sin(k_y)], \tag{5.43}$$

using the fact that $F_{\sigma\sigma}^{+\hat{x}(\hat{y})} = -F_{\sigma\sigma}^{-\hat{x}(\hat{y})}$ [56].

To illustrate the differences between the superconducting gap functions Eqs. (5.33) to (5.38), in Fourier space, we plot the normalized magnitude of the gap, i.e., the quantity $|\Delta(\mathbf{k})|$ as a function of momentum $\mathbf{k} = (k_x, k_y)$ over the first Brillouin zone $(-\pi, \pi)$, in fig. 7. The four panels display distinct gap-symmetry patterns. Panel (a) (extended s -wave) is invariant under 90° rotations and reflections about both axes, with no sign change, i.e., full C_{4v} symmetry. Panel (b) ($d_{x^2-y^2}$) retains the lattice fourfold symmetry but changes sign under a 90° rotation, producing nodal lines along $k_x = \pm k_y$; it is even under $k_x \rightarrow -k_x$ and $k_y \rightarrow -k_y$, but odd under $k_x \leftrightarrow k_y$. Panel (c) ($p_x + p_y$) is anisotropic and only preserves the reflections that map the two lobes correctly; it is odd under both $k_x \rightarrow -k_x$ and $k_y \rightarrow -k_y$. Panel (d) ($p_x + ip_y$) produces nearly isotropic $|\Delta(\mathbf{k})|$, since the two orthogonal p -components combine with a relative phase, effectively restoring rotational symmetry in the magnitude.

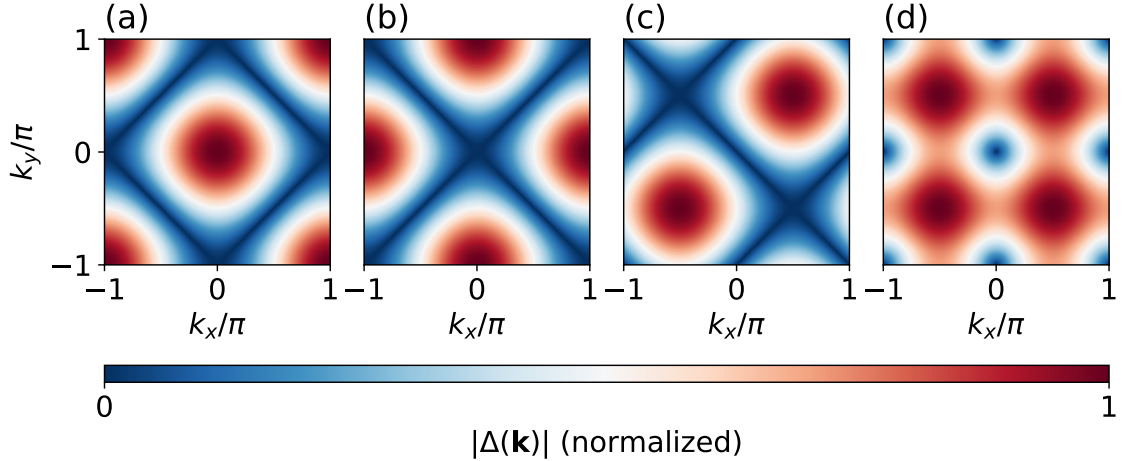


Figure 7: Momentum-space structure of the gap magnitude $|\Delta(\mathbf{k})|$ for (a) extended s -wave, (b) $d_{x^2-y^2}$ -wave, (c) $p_x + p_y$ -wave, and (d) $p_x + ip_y$ -wave phases in the 1st Brillouin zone. The color scale shows the local gap magnitude normalized to the maximum value within each panel.

One way to represent any of the order parameters introduced above is by defining a 2×2 matrix $\Delta(\mathbf{k})$ [72]. For a singlet pairing $\Delta^{(S)}(\mathbf{k})$ must be antisymmetric in spin and symmetric in \mathbf{k} , as shown in table 2, and described by a single even function $\psi(\mathbf{k})$,

$$\Delta^{(S)}(\mathbf{k}) = \Delta^{(S)}(\mathbf{k})i\sigma^2 = \begin{bmatrix} 0 & \psi(\mathbf{k}) \\ -\psi(\mathbf{k}) & 0 \end{bmatrix} \quad (5.44)$$

On the other hand, triplet pairing is odd in parity. The matrix can then be described by the so called \mathbf{d} -vector [72, 19] as

$$\Delta^{(T)}(\mathbf{k}) = \begin{bmatrix} \Delta_{\uparrow\uparrow}(\mathbf{k}) & \Delta_{\uparrow\downarrow}(\mathbf{k}) \\ \Delta_{\downarrow\uparrow}(\mathbf{k}) & \Delta_{\downarrow\downarrow}(\mathbf{k}) \end{bmatrix} = \begin{bmatrix} -d_x(\mathbf{k}) + id_y(\mathbf{k}) & d_z(\mathbf{k}) \\ d_z(\mathbf{k}) & d_x(\mathbf{k}) + id_y(\mathbf{k}) \end{bmatrix} = (\mathbf{d}(\mathbf{k}) \cdot \mathbf{S})i\sigma^2 \quad (5.45)$$

This notation is particularly practical because under spin rotation operation \mathbf{d} transforms like a three-dimensional vector.

5.5 Bogoliubov–de Gennes (BdG) formalism

In previous chapters, we discussed normal metals, ferromagnetism and superconductivity in the context of the tight-binding model and the extended Hubbard model. Following a similar treatment to Refs. [42, 44] we combine Eqs. (3.4), (4.10), (5.5) and (5.27) derived earlier. We can thus write down an effective Hamiltonian for superconductors, ferromagnets, and normal metals:

$$\begin{aligned} \hat{H} = & E_0 - \sum_{i,\sigma} \mu_i \hat{c}_{i,\sigma}^\dagger \hat{c}_{i,\sigma} - \sum_{\langle i,j \rangle, \sigma} t_{ij} \hat{c}_{i,\sigma}^\dagger \hat{c}_{j,\sigma} - \sum_{i,\sigma,\sigma'} \hat{c}_{i,\sigma}^\dagger [\mathbf{S} \cdot \mathbf{m}_i]_{\sigma,\sigma'} \hat{c}_{i,\sigma'} \\ & - \sum_i \left(\Delta_i \hat{c}_{i,\uparrow}^\dagger \hat{c}_{i,\downarrow}^\dagger + \Delta_i^\dagger \hat{c}_{i,\downarrow} \hat{c}_{i,\uparrow} \right) - \sum_{\langle i,j \rangle, \sigma, \sigma'} \left(\Delta_{ij}^{\sigma\sigma'} \hat{c}_{j,\sigma'}^\dagger \hat{c}_{i,\sigma}^\dagger + (\Delta_{ij}^{\sigma\sigma'})^\dagger \hat{c}_{i,\sigma} \hat{c}_{j,\sigma'} \right), \end{aligned} \quad (5.46)$$

where we have Fourier-transformed Eq. (5.5) back to real space and Eq. (5.27) is written compactly by setting $\Delta_{ij}^{\sigma\sigma'} \equiv [V'\delta_{\sigma,\sigma'} + V(1 - \delta_{\sigma\sigma'})]F_{i,j}^{\sigma\sigma'}$.

This Hamiltonian can be written compactly using the Lattice \otimes Nambu \otimes Spin space [42, 44], Eq. (2.21),

$$\hat{H} = E_0 + \frac{1}{2}\check{\mathbf{c}}^\dagger \check{\mathbf{H}} \check{\mathbf{c}}, \quad \check{\mathbf{H}} = [\hat{\mathbf{H}}_{ij}], \quad \hat{\mathbf{H}}_{ij} = \begin{pmatrix} M_{ij} & \Delta_{ij} \\ \Delta_{ji}^* & -M_{ij}^* \end{pmatrix}. \quad (5.47)$$

Here we have defined the matrix block $M_{ij} = -(\mu_i + \mathbf{S} \cdot \mathbf{m}_i)\delta_{ij} - t_{ij}$. In the case of conventional superconductivity, we have $\Delta_{ij} = i\sigma_2 F_{ii}^{\uparrow,\downarrow}\delta_{ij}$. In other words, the gap parameter is local due to the on-site attractive interaction U_i .

$\check{\mathbf{H}}$ defines a $4N \times 4N$ matrix. Diagonalizing this matrix diagonalizes the Hamiltonian operator \hat{H} as well. We write the eigenvalue equation for the corresponding $4N$ -element eigenvectors $\check{\chi}_n = (\chi_{n,1}, \dots, \chi_{n,N})$:

$$\check{\mathbf{H}}\check{\chi}_n = E_n \check{\chi}_n. \quad (5.48)$$

Each component of $\check{\chi}_n$ is a bispinor $\chi_{n,i} = (u_{n,i}, v_{n,i})$ that can be decomposed into the corresponding electron spinor u and hole spinor v . The eigenvalue equation in lattice space is given by

$$\sum_j \hat{\mathbf{H}}_{ij} \chi_{n,j} = E_n \chi_{n,i}. \quad (5.49)$$

Since $\check{\mathbf{H}}$ is Hermitian, it can be diagonalized by factorization as $\check{\mathbf{H}} = \check{\mathbf{X}} \check{D} \check{\mathbf{X}}^{-1} = \check{\mathbf{X}} \check{D} \check{\mathbf{X}}^\dagger$, where $\check{\mathbf{X}} = [\check{\chi}_n]$ is a matrix constructed from the eigenvectors and $\check{D} = \text{diag}(E_{-2N}, \dots, E_{2N})$ from the eigenvalues. Due to particle-hole symmetry, the eigenvalues come in pairs that can be labeled as $E_{-n} = -E_{+n}$. Defining the basis $\check{\mathbf{c}} \equiv \check{\mathbf{X}} \check{\gamma}$, Equation (5.47) can be written in diagonal form

$$\hat{H} = E_0 + \frac{1}{2}\check{\gamma}^\dagger \check{D} \check{\gamma} = E_0 + \frac{1}{2} \sum_n E_n \gamma_n^\dagger \gamma_n, \quad (5.50)$$

with $\check{\gamma} = \check{\mathbf{X}}^\dagger \check{\mathbf{c}} = [\gamma_n]$. We can write each component explicitly as:

$$\gamma_n = \sum_{i,\sigma} \left(u_{n,i,\sigma}^* \hat{c}_{i,\sigma} + v_{n,i,\sigma}^* \hat{c}_{i,\sigma}^\dagger \right). \quad (5.51)$$

For a γ_n corresponding to a positive eigenvalue E_n , then particle-hole symmetry implies that there is another eigenvector γ_{-n} with eigenvalue E_{-n} , such that $\gamma_{-n}^\dagger = \gamma_n$. This means the operators γ_{-n} and γ_n are not linearly independent, since the original Hamiltonian operator Eq. (5.46) contains only $2N$ degrees of freedom, whereas the extension to Nambu space formally doubles the dimensionality. We can avoid this artificial doubling by exploiting the above mentioned symmetry and discard the eigenvalues $E_n < 0$ and corresponding eigenvectors. The Hamiltonian operator Eq. (5.50) can be rewritten using independent operators as

$$\begin{aligned} \hat{H} &= E_0 + \frac{1}{2} \sum_{n>0} E_n \gamma_n^\dagger \gamma_n + \frac{1}{2} \sum_{n<0} E_n \gamma_n^\dagger \gamma_n \\ &= E_0 + \frac{1}{2} \sum_{n>0} E_n \gamma_n^\dagger \gamma_n - \frac{1}{2} \sum_{n>0} E_n \gamma_n \gamma_n^\dagger \\ &= E_0 + \frac{1}{2} \sum_{n>0} E_n (\gamma_n^\dagger \gamma_n - \gamma_n \gamma_n^\dagger) \\ &= E_0 + \sum_{n>0} E_n (\gamma_n^\dagger \gamma_n - 1/2), \end{aligned} \quad (5.52)$$

where in the last line we have used anticommutation of fermionic operators, Eq. (2.8).

Now that the Hamiltonian is diagonalized, we can look at the gap parameter. The operators $(\gamma_n^\dagger, \gamma_n)$ are fermionic so we can assume that in equilibrium they obey Fermi-Dirac distribution $f(E_n)$, Eq. (3.15). Hence, $\langle \gamma_n^\dagger \gamma_m \rangle = f(E_n; T) \delta_{nm}$ and $\langle \gamma_n \gamma_m^\dagger \rangle = 1 - f(E_n; T) \delta_{nm}$. Inserting these into the expression for the gap we obtain

$$\Delta_i = U_i \langle \hat{c}_{i,\uparrow} \hat{c}_{i,\downarrow} \rangle = U_i \sum_{n,m>0} [v_{n,i,\uparrow}^* u_{m,i,\downarrow} \langle \gamma_n^\dagger \gamma_m \rangle + u_{n,i,\uparrow} v_{m,i,\downarrow}^* \langle \gamma_n \gamma_m^\dagger \rangle], \quad (5.53)$$

$$\boxed{\Delta_i(T) = U_i \sum_{n>0} [v_{n,i,\uparrow}^* u_{n,i,\downarrow} f(E_n; T) + u_{n,i,\uparrow} v_{n,i,\downarrow}^* (1 - f(E_n; T))]} \quad (5.54)$$

We see that the BdG formalism leads to a self-consistent problem. The gap parameter depends on the quasiparticle amplitudes $u_{n,i,\sigma}$ and $v_{n,i,\sigma}$, which themselves are obtained by solving the BdG eigenvalue problem $\tilde{\mathbf{H}}\tilde{\chi}_n = E_n \tilde{\chi}_n$. However, the Hamiltonian $\tilde{\mathbf{H}}$ contains Δ_i as an input parameter, meaning that Δ_i determines the quasiparticle states while those states in turn determines the gap.

5.6 Self-consistent solution for on-site *s*-wave pairing

Equations (5.48) and (5.54) define a coupled system of equations that is solved self-consistently by iteratively determining the quasiparticle spectrum and the superconducting order parameter until self-consistency is achieved between them. We begin with an initial guess for the gap function Δ_{ij} , and using this trial Δ_{ij} , the BdG eigenvalue problem Eq. (5.48) is solved to obtain the quasiparticle energies E_n and wavefunctions $\chi_{m,i} = (u_{n,i,\uparrow}, v_{n,i,\downarrow})$. These solutions are then substituted into the self-consistency condition Eq. (5.54), which yields an updated gap function. The procedure is repeated, diagonalizing the Hamiltonian and recalculating Δ_{ij} at each step, until convergence, i.e., until successive iterations of Δ_{ij} differ by less than a predefined tolerance.

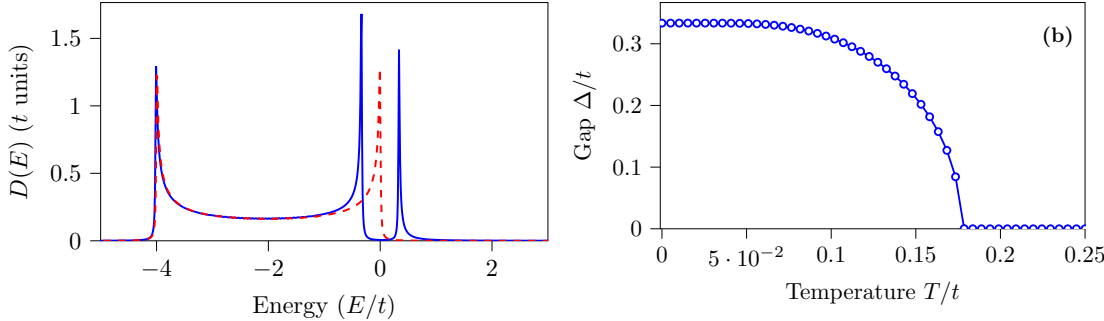


Figure 8: (a) Density of states $D(E)$ (in units of t) as a function of energy E/t for a one-dimensional system with $L = 512$ sites at low temperature ($T = 10^{-6}t$). The mean bandgap for the system is found self-consistently, $\Delta \approx 0.33351t$. The results are obtained by solving the self-consistent mean-field BdG equations. The blue solid line corresponds to a superconducting state with attractive potential $U = 2t$ and chemical potential $\mu = 2t$. The red dashed line represents the normal metallic state with zero gap ($\Delta = 0$) and no attractive potential ($U = 0$). A Lorentzian broadening $0.01t$ is used. (b) Temperature dependence of the superconducting gap Δ/t for the same superconducting 1D system and parameters, showing the rapid closing of the gap as temperature increases.

Once the Bogoliubov-de Gennes equations have been solved self-consistently, all relevant physical observables can be expressed in terms of the quasiparticle amplitudes $\{u_{n,i,\sigma}, v_{n,i,\sigma}\}$ and eigenenergies $\{E_n\}$. The single-particle density at site i and spin σ [44] is obtained from

$$n_{i\sigma} = \sum_{n>0} [|u_{n,i,\sigma}|^2 f(E_n; T)] = \sum_{n>0} [|v_{n,i,\sigma}|^2 (1 - f(E_n; T))]. \quad (5.55)$$

The total local charge density and magnetization in the z direction follows as

$$n_i = n_{i\uparrow} + n_{i\downarrow}, \quad m_i = n_{i\uparrow} - n_{i\downarrow}. \quad (5.56)$$

The local density of states (LDOS) can be computed from the quasiparticle spectrum as

$$D_i(E) = \sum_{n>0} [|u_{n,i}|^2 \delta(E - E_n) + |v_{n,i}|^2 \delta(E + E_n)], \quad (5.57)$$

which is directly measurable, for instance, via scanning tunneling [44]. The total density of states is obtained by summing over all lattice sites, as shown in fig. 8(a). Other quantities, such as the kinetic energy, supercurrent density, and total free energy, can also be derived from the BdG

eigenstates. Thus, once the BdG system is converged, the full set of microscopic observables can be systematically evaluated from the eigenvalues and eigenvectors of the self-consistent Hamiltonian.

The Fermi-Dirac distribution introduces temperature dependence. As the temperature increases, thermal excitations progressively depopulate the Cooper pairs, shrinking the superconducting gap $\Delta_{ij}(T)$. The iterative BdG solution at each temperature gives a different gap parameter, which continuously decreases and eventually vanishes at the critical temperature T_c , indicating transition to the normal state, as shown in fig. 8(b). An efficient algorithm to locating the critical temperature is the Bisection algorithm 1, with parameter $p \rightarrow T$ and order parameter $\Phi \rightarrow \Delta$. The system solver f is replaced by performing a single iteration of the self-consistency procedure to determine whether the order parameter is increasing or decreasing.

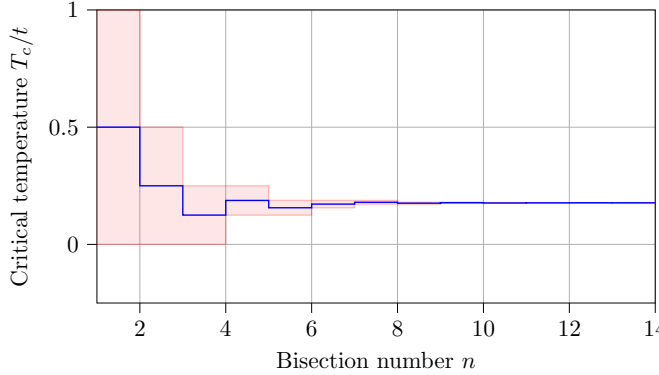


Figure 9: Convergence of the critical temperature T_c/t for a one-dimensional system with $L = 512$ sites and attractive potential $U = 2t$ as a function of the bisection iteration number n . The blue curve shows the estimated T_c/t at each iteration, while the shaded region highlights the range of uncertainty during the early stages of the bisection process. Up to tolerance $\text{tol} = 10^{-6}$, the critical temperature is $T_c \approx 0.17738t$.

As shown in fig. 9, starting with a range enclosing the critical temperature value, the algorithm rapidly converges towards the critical value. Note that the values for the gap and the critical temperature are exaggerated for better visualization. The ratio between the critical temperature T_c and the gap at zero temperature, $\Delta(T=0)$, is approximately $r \approx 3.77$. This is very close to the BCS ratio, Eq. (5.24). The difference comes because the BCS ratio is derived in the weak coupling limit, but in the current case U is comparable to t .

5.7 Bogoliubov–de Gennes equations in the extended Hubbard model

In this subsection, the BdG formalism is applied to superconducting states with unconventional pairing symmetries. It provides a natural framework to treat momentum-dependent and anisotropic order parameters, such as the ones we have mentioned in Eqs. (5.33) to (5.38). The full BdG Hamiltonian, Eq. (5.46), can in this case be written explicitly as

$$\begin{aligned} \hat{H}_{\text{BdG}} = & - \sum_{i,\sigma} \mu_i \hat{c}_{i,\sigma}^\dagger \hat{c}_{i,\sigma} - \sum_{\langle i,j \rangle, \sigma} t_{ij} \hat{c}_{i,\sigma}^\dagger \hat{c}_{j,\sigma} \\ & - \sum_{i,\sigma,\sigma'} \hat{c}_{i,\sigma}^\dagger [\mathbf{S} \cdot \mathbf{m}_i]_{\sigma,\sigma'} \hat{c}_{i,\sigma'} - U \sum_i \left(F_{i,i}^{\uparrow\downarrow} \hat{c}_{i,\downarrow}^\dagger \hat{c}_{i,\uparrow}^\dagger + \text{h.c.} \right) \\ & - V \sum_{\langle i,j \rangle} \left(F_{i,j} \hat{c}_{j,\downarrow}^\dagger \hat{c}_{i,\uparrow}^\dagger + \text{h.c.} \right) - V' \sum_{\langle i,j \rangle, \sigma} \left(F_{i,j}^{\sigma\sigma} \hat{c}_{j,\sigma}^\dagger \hat{c}_{i,\sigma}^\dagger + \text{h.c.} \right). \end{aligned} \quad (5.58)$$

However, a more practical approach for numerically modeling this Hamiltonian is to use the \mathbf{d} -vector representation, introduced in Eqs. (5.44) and (5.45), reformulated in lattice space. Using the superconducting gap parameters defined in Eqs. (5.33) to (5.38), we construct the real-space pairing kernel Δ_{ij} in the singlet-triplet decomposition:

$$\Delta_{ij} = \begin{pmatrix} -d_{ij}^x + id_{ij}^y & \psi_{ij} + d_{ij}^z \\ -\psi_{ij} + d_{ij}^z & d_{ij}^x + id_{ij}^y \end{pmatrix} = \psi_{ij} i\sigma^2 + (\mathbf{d}_{ij} \cdot \mathbf{S}) i\sigma^2, \quad (5.59)$$

with singlet term

$$\psi_{i,i\pm\hat{x}} = \Delta_s(i) + \Delta_{d_{x^2-y^2}}(i), \quad \psi_{i,i\pm\hat{y}} = \Delta_s(i) - \Delta_{d_{x^2-y^2}}(i). \quad (5.60)$$

The **d**-vector components are

$$d_{i,i\pm\hat{x}}^z = \pm\Delta_{p_x}(i), \quad d_{i,i\pm\hat{y}}^z = \pm\Delta_{p_y}(i), \quad (5.61)$$

$$d_{i,i\pm\hat{x}(\hat{y})}^x = \frac{1}{2} \left(\Delta_{i,i\pm\hat{x}(\hat{y})}^{\uparrow\uparrow} - \Delta_{i,i\pm\hat{x}(\hat{y})}^{\downarrow\downarrow} \right), \quad d_{i,i\pm\hat{x}(\hat{y})}^y = \frac{1}{2i} \left(\Delta_{i,i\pm\hat{x}(\hat{y})}^{\uparrow\uparrow} + \Delta_{i,i\pm\hat{x}(\hat{y})}^{\downarrow\downarrow} \right), \quad (5.62)$$

$$\text{with } \Delta_{i,i\pm\hat{x}(\hat{y})}^{\uparrow\uparrow} = \pm\Delta_{p_{x(y)}}^{\uparrow\uparrow}, \quad \Delta_{i,i\pm\hat{x}(\hat{y})}^{\downarrow\downarrow} = \pm\Delta_{p_{x(y)}}^{\downarrow\downarrow}. \quad (5.63)$$

This decomposition fixes the even (singlet) and odd (triplet) bond symmetries by construction and can readily be inserted into the BdG Hamiltonian, Eq. (5.46), yielding:

$$\begin{aligned} \hat{H}_{BdG} = & - \sum_{i,\sigma} \mu_i \hat{c}_{i,\sigma}^\dagger \hat{c}_{i,\sigma} - \sum_{\langle i,j \rangle, \sigma} t_{ij} \hat{c}_{i,\sigma}^\dagger \hat{c}_{j,\sigma} - \sum_{i,\sigma,\sigma'} \hat{c}_{i,\sigma}^\dagger [\mathbf{S} \cdot \mathbf{m}_i]_{\sigma,\sigma'} \hat{c}_{i,\sigma'} \\ & - \sum_{i,j,\sigma,\sigma'} \left(\hat{c}_{i,\sigma}^\dagger [(\Delta_0 \delta_{ij} + \psi_{ij} + \mathbf{d}_{ij} \cdot \mathbf{S}) i\sigma^2]_{\sigma,\sigma'} \hat{c}_{j,\sigma'}^\dagger + \text{h.c.} \right). \end{aligned} \quad (5.64)$$

This version of the Hamiltonian can easily be recast in Nambu \otimes Lattice \otimes Spin space, described in section 5.5, and diagonalized numerically. The total density of states for *p* and *d*-wave superconductors can be calculated from the obtained eigenvalues, as shown in fig. 10. Panel (a) shows that the DOS for the chiral $p_x + ip_y$ state is fully gapped centered at the Fermi level $E/t = 0$ and therefore there are no electron states allowed in the gap. In the case of p_x , $p_x + p_y$ and $d_{x^2-y^2}$ -wave superconductors the DOS is not fully gapped and decreases as the Fermi level is approached. This is characteristic for symmetries with nodal lines intersecting the Fermi surface in momentum space; as we have seen in fig. 7, this is the case for $p_x + p_y$ and $d_{x^2-y^2}$ -wave symmetries, and it is also true for p_x -wave.

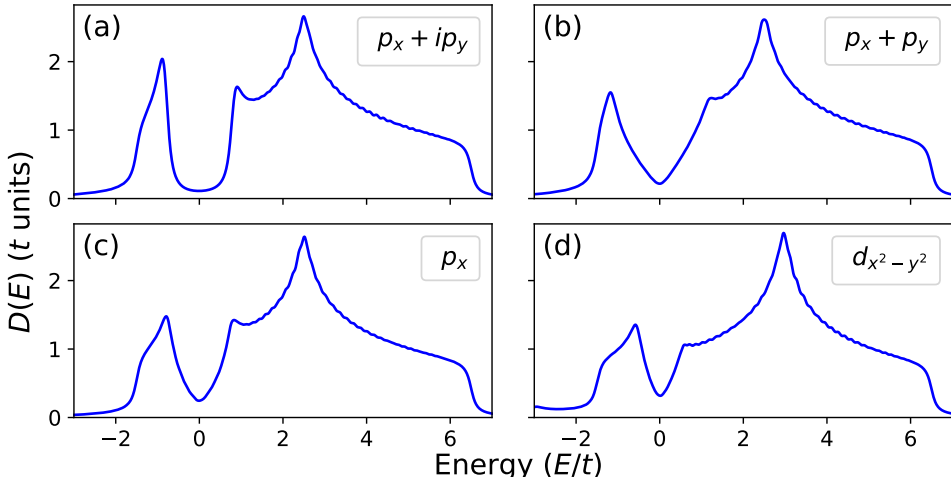


Figure 10: Density of states $D(E)$ as a function of energy E/t for a $71a \times 71a$ lattice with periodic boundary conditions, computed (non-self-consistently) in real space with a Lorentzian broadening of $\eta = 0.1t$ and chemical potential $\mu = -2.5t$. The panels correspond to different superconducting order-parameter symmetries: (a) chiral $p_x + ip_y$, (b) real $p_x + p_y$, (c) p_x , and (d) $d_{x^2-y^2}$.

Although it is somehow common practice to parametrize the Hamiltonian entirely in momentum-space (or partially in the case of interfaces as described in appendix A), in Eq. (5.64) we adopt a purely real-space (lattice) formulation. This representation is more general without assumptions on the lattice symmetry; it therefore affords flexibility in the choice of boundary conditions and is straightforward to implement numerically for different lattices, such as the triangular lattice used in section 6. Moreover, it allows us to analyze the spatial structure and edge effects in unconventional superconductors.

When open boundary conditions are imposed, interesting effects arise, as shown in fig. 11. We immediately notice the edge LDOS is non-zero inside the gap. Figure 11(a) shows a sharp peak, whereas the chiral case shows the edge contribution from a dispersing chiral mode. This can

be explained by *Andreev bound states* [85] arising around $E/t = 0$ near the edges of $p_x + p_y$ -wave superconductor when we assume open boundary conditions. Assuming that quasiparticles are specularly reflected, $(k_x, k_y) \rightarrow (-k_x, k_y)$, and the real order parameter $\Delta(\mathbf{k}) \propto \sin k_x + \sin k_y$ changes sign between incoming and reflected trajectories (a π -phase shift), resulting in a sharp peak at $E = 0$. On the other hand, the chiral $p_x + ip_y$ -wave has order parameter $\Delta(\mathbf{k}) \propto \sin k_x + i \sin k_y$. Upon a specular reflection, the phase obtained is not generally π , but depends on the momentum parallel to the boundary. This leads to a less pronounced, more broadened zero-energy peak.

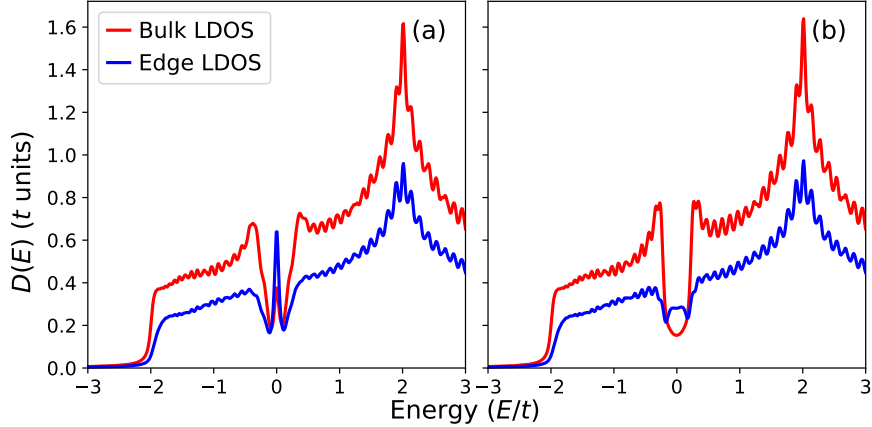


Figure 11: Edge-local (blue) and bulk (red) density of states $D(E)$ for $p_x + p_y$ (a) and $p_x + ip_y$ -wave (b) superconductors for a $45a \times 45a$ lattice with open boundary conditions. Using gap magnitude $\Delta_0 = 0.1t$, chemical potential $\mu = -2t$ and Lorentzian broadening $\eta = 0.04t$.

Note that there is zero-energy energy DOS contribution for the bulk case (as shown in fig. 11) due to sample size effects and the way we define the thickness of the edges. This can be better seen by inspecting the spatial distribution of the zero-energy LDOS over the lattice. In fig. 12(a), corresponding to the $p_x + p_y$ state, the spectral weight is strongly concentrated in a two of the corners, with node at the diagonal and only weak spreading along the edges. In contrast, fig. 12(b) shows that for the chiral $p_x + ip_y$ state the zero-energy LDOS is distributed rather uniformly along all edges, with negligible weight in the bulk, reflecting the presence of dispersing chiral edge modes.

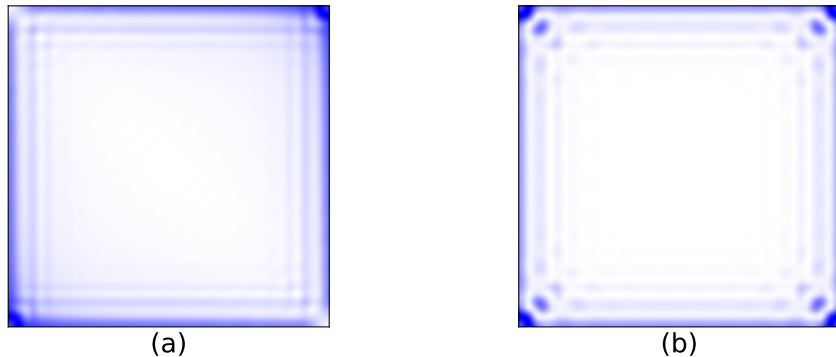


Figure 12: Spatial distribution of the zero-energy local density of states (LDOS) on a $45a \times 45a$ lattice with open boundaries for (a) $p_x + p_y$, (b) $p_x + ip_y$. In these plots we use a Lorentzian broadening of $\eta = 0.01t$ and chemical potential $\mu = -2.5t$.

So far our treatment of unconventional superconductors has been purely non-self-consistent. We now define, in direct analogy to BCS theory, Eq. (5.54), the correlation functions using the eigen-

values and eigenvectors of the Hamiltonian matrix [74]:

$$F_i^{\pm\hat{x}(\hat{y})} = \sum_{n>0} \left(u_{n,i,\uparrow} v_{n,i\pm\hat{x}(\hat{y}),\downarrow}^* [1 - f(E_n; T)] + v_{n,i,\uparrow}^* u_{n,i\pm\hat{x}(\hat{y}),\downarrow} f(E_n; T) \right), \quad (5.65)$$

$$F_{i,\uparrow\uparrow}^{\pm\hat{x}(\hat{y})} = \sum_{n>0} \left(u_{n,i,\uparrow} v_{n,i\pm\hat{x}(\hat{y}),\uparrow}^* [1 - f(E_n; T)] + v_{n,i,\uparrow}^* u_{n,i\pm\hat{x}(\hat{y}),\uparrow} f(E_n; T) \right), \quad (5.66)$$

$$F_{i,\downarrow\downarrow}^{\pm\hat{x}(\hat{y})} = \sum_{n>0} \left(u_{n,i,\downarrow} v_{n,i\pm\hat{x}(\hat{y}),\downarrow}^* [1 - f(E_n; T)] + v_{n,i,\downarrow}^* u_{n,i\pm\hat{x}(\hat{y}),\downarrow} f(E_n; T) \right). \quad (5.67)$$

Once again, we are faced with a self-consistent problem: the anomalous correlators that define the gaps are computed from the BdG eigenstates, which themselves depend on those gaps. Unlike the standard case, however, where a single scalar Δ satisfies one gap equation, here we must solve a coupled set for the vector of order parameters,

$$\Delta \equiv \left\{ \Delta_0, \Delta_s, \Delta_{d_{x^2-y^2}}, \Delta_{p_x}, \Delta_{p_y}, \Delta_{p_x}^{\uparrow\uparrow}, \Delta_{p_y}^{\uparrow\uparrow}, \Delta_{p_x}^{\downarrow\downarrow}, \Delta_{p_y}^{\downarrow\downarrow} \right\}. \quad (5.68)$$

This complicates the problem significantly. Because the different symmetry channels are coupled through $\check{\mathbf{H}}$, multiple components can coexist; an example is the coexistence of d and p -wave order parameters in superconductor/(anti)ferromagnet bi-layer systems, where the proximity effect induces an imbalance of spin-up and spin-down electron densities [86]. Numerically, methods like under-relaxation [87] may be needed to ensure robust convergence and stability. When several solutions are obtained for the same set of parameters (μ, T) , the state with the lowest free energy, Eq. (3.18), is adopted as the true one [88]. In practice, this requires a robust optimization scheme that includes different initial guesses to explore the energy landscape and avoid local minima.

5.8 Concluding remarks

In this section, we introduced the BCS theory of superconductivity, followed by an introduction to unconventional superconductivity within the extended Hubbard model. We then reformulated the corresponding Hamiltonians into the Bogoliubov–de Gennes framework and analyzed the resulting superconducting states and their properties. For the BCS-type superconductors, we derived the self-consistent gap equation and solved it numerically.

For unconventional superconductivity, we similarly derived the relevant self-consistent gap equations and outlined the numerical scheme required to solve them, but did not implement this scheme within the scope of the present project. A fully self-consistent analysis of the various unconventional superconducting phases will instead be performed as part of the master’s thesis.

6 Ruderman–Kittel–Kasuya–Yosida (RKKY) Interaction

Before we introduce proximity effects in heterostructures it is useful to understand how a conducting medium can already intertwine superconductivity and magnetism in a non-homogeneous system. The RKKY interaction [23, 24, 25] describes the indirect exchange coupling between localized spins interacting via itinerant spin carriers in a material.

In this section, the RKKY mechanism is introduced. Then the behavior of two spins on a square lattice is analyzed. Next, three spins are arranged symmetrically on a triangular lattice to induce geometric frustration whenever they interact antiferromagnetically. The resulting spin ground state configuration is studied as a function of the distance between the spins. To the best of our knowledge, this last part has not been previously investigated and thus constitutes an original research contribution from this thesis.

6.1 Formalism of the RKKY interaction

In metals, the RKKY interaction is usually mediated by electrons. When itinerant electrons approach a localized spin, the wave functions of electrons are scattered in different ways depending on their spin. Therefore, the spin expectation value of the itinerant electrons oscillates and decays as a function of the distance from the localized spin. When a second localized spin couples to the itinerant electrons, its lowest-energy spin orientation depends on whether it is placed in a peak or trough of the spin density generated by the first localized spin. The net interaction between the spins can thus be either ferromagnetic or antiferromagnetic, depending on their separation distance [89]. In non-superconducting metals, the RKKY interaction usually exhibits a decaying oscillation between ferromagnetic and antiferromagnetic coupling as the separation distance between the spins increases, as shown in fig. 13. In singlet superconductors, an additional antiferromagnetic coupling appears [27]. The indirect coupling between localized spins gives rise to an effective interaction that can take the same functional forms as a direct exchange coupling. Depending on the microscopic properties of the system and on the approximations employed, different types of spin–spin interactions emerge, which can be collected in the effective Hamiltonian

$$H_{\text{RKKY}} = \sum_{i,j} \mathbf{J}_{ij} \cdot (\mathbf{s}_i \circ \mathbf{s}_j) + \sum_{i,j} \mathbf{D}_{ij} \cdot (\mathbf{s}_i \times \mathbf{s}_j), \quad (6.1)$$

where \circ refers to element-wise multiplication.

If \mathbf{J}_{ij} is isotropic, i.e., $J_{ij}^x = J_{ij}^y = J_{ij}^z = J_{ij}$, the first term reduces to a Heisenberg interaction, and the spins tend to minimize or maximize their total spin depending on the sign of J_{ij} (antiferromagnetic vs. ferromagnetic coupling). When the components of \mathbf{J}_{ij} differ, the exchange becomes anisotropic (Ising interaction). It can arise, for example, in unconventional superconductors [89] or in systems with strong spin-orbit coupling [90]. The last term is the Dzyaloshinskii-Moriya (DM) interaction. This type of interaction allows for twisted spin configurations and does not give rise to simple ferromagnetic or anti-ferromagnetic ordering. This interaction commonly occurs in certain types of unconventional superconductors or in the presence of spin-orbit coupling. Since we are not interested in spin-orbit coupling or non-unitary superconducting orders in this thesis, we expect the DM term to be zero up to numerical accuracy. For that reason, we will not further delve into the physics of the DM interaction.

In the context of the tight-binding model, the RKKY interaction is modeled by placing classical spins \mathbf{s}_i at positions \mathbf{R}_i on the surface of the material interact with the itinerant electrons via an exchange interaction with a Hamiltonian,

$$\hat{H}_F = -\frac{1}{2} \mathcal{J} \sum_{i,\sigma,\sigma'} \hat{c}_{i,\sigma}^\dagger (\mathbf{s}_i \cdot \mathbf{S})_{\sigma,\sigma'} \hat{c}_{i,\sigma'}, \quad (6.2)$$

with \mathcal{J} the magnitude of the spin-electron exchange coupling. The rest of the Hamiltonian is given by Eq. (5.64). Numerically, we normalize the spins such that $|\mathbf{s}_i| = 1$, since only the combined magnitude $|\mathcal{J}\mathbf{s}_i|$ enters the numerical model [27].

6.2 Spin-spin interactions

For a general conductor interaction with N classical spins \mathbf{s}_i , the free energy (up to second-order perturbation) can be written as

$$\mathcal{F}(\{\mathbf{s}_i\}) = \mathcal{F}_0 + \sum_{i=1}^N \boldsymbol{\mu}_i \cdot \mathbf{s}_i + \frac{1}{2} \sum_{\substack{i,j=1 \\ i \neq j}}^N \mathbf{s}_i \cdot \boldsymbol{\eta}_{ij} \mathbf{s}_j, \quad (6.3)$$

Here $\boldsymbol{\mu}_i$ is a vector representing the interactions between spin \mathbf{s}_i and the host material, while $\boldsymbol{\eta}_{ij}$ is a tensor that gives the effective interaction between the two spins \mathbf{s}_i and \mathbf{s}_j . \mathcal{F}_0 contains all contributions that are independent of the spin directions [27]. For a symmetric system with a homogeneous d -vector we can assume that $\boldsymbol{\mu}_i \equiv \boldsymbol{\mu} = \text{const}$. This significantly simplifies the problem, since now we can find the ground state spin configuration from the parameters $\{\mathcal{F}_0, \boldsymbol{\mu}, \boldsymbol{\eta}_{ij}\}$.

For two classical spins we adapt the approach presented in Ref. [27]. The interactions $\boldsymbol{\mu}$ and $\boldsymbol{\eta}$ can be obtained from the numerical calculations of the free energy, Eq. (6.3). To do that we define a short-hand notation for the free energy,

$$\begin{aligned} \mathcal{F}_{+n,+m} &\equiv \mathcal{F}(+\hat{\mathbf{e}}_n, +\hat{\mathbf{e}}_m), & \mathcal{F}_{+n,-m} &\equiv \mathcal{F}(+\hat{\mathbf{e}}_n, -\hat{\mathbf{e}}_m), \\ \mathcal{F}_{-n,-m} &\equiv \mathcal{F}(-\hat{\mathbf{e}}_n, -\hat{\mathbf{e}}_m), & \mathcal{F}_{-n,+m} &\equiv \mathcal{F}(-\hat{\mathbf{e}}_n, +\hat{\mathbf{e}}_m), \end{aligned} \quad (6.4)$$

for $n, m \in \{1, 2, 3\}$. Each permutation can then be written as

$$\mathcal{F}_{\pm n, \pm m} = \mathcal{F}_0 \pm (\mu_n + \mu_m) + \eta_{nm}, \quad \mathcal{F}_{\pm n, \mp m} = \mathcal{F}_0 \pm (\mu_n - \mu_m) - \eta_{nm} \quad (6.5)$$

The components of μ and η can then be extracted using:

$$\mu_n = \frac{1}{4} (\mathcal{F}_{+n,+n} - \mathcal{F}_{-n,-n}) \quad (6.6)$$

$$\eta_{nm} = \frac{1}{4} (\mathcal{F}_{+n,+m} + \mathcal{F}_{-n,-m} - \mathcal{F}_{+n,-m} - \mathcal{F}_{-n,+m}). \quad (6.7)$$

By calculating the free energy for all 36 possible combinations of spins oriented along the cardinal directions $\{\pm \mathbf{e}_1, \pm \mathbf{e}_2, \pm \mathbf{e}_3\}$, we can fully characterize the leading-order spin interactions [27]. The elements of the $\boldsymbol{\eta}_{ij}$ can be parametrized in a form similar to Eq. (6.1)

$$\mathbf{s}_i \boldsymbol{\eta}_{ij} \mathbf{s}_j = \mathbf{J}_{ij} \cdot (\mathbf{s}_i \circ \mathbf{s}_j) + \mathbf{D}_{ij} \cdot (\mathbf{s}_i \times \mathbf{s}_j) + \mathbf{s}_i \cdot \boldsymbol{\Omega}_{ij} \mathbf{s}_j, \quad (6.8)$$

with $\boldsymbol{\Omega}$ representing any remaining contributions from $\boldsymbol{\eta}$ not captured by \mathbf{J} or \mathbf{D} . As shown in Ref. [27], the $\boldsymbol{\Omega}$ term vanishes for two spins on a square lattice. In all of our calculations we likewise find its contribution to be negligible, and we therefore omit this term in the rest of the discussion. To leading orders in \mathbf{s}_i the free energy of the system is then

$$\mathcal{F} = \mathcal{F}_0 + \boldsymbol{\mu} \cdot \sum_{i=1}^N \mathbf{s}_i + \frac{1}{2} \sum_{\substack{i,j=1 \\ i \neq j}}^N [\mathbf{J}_{ij} \cdot (\mathbf{s}_i \circ \mathbf{s}_j) + \mathbf{D}_{ij} \cdot (\mathbf{s}_i \times \mathbf{s}_j)] \quad (6.9)$$

In this parametrization $J_z \equiv \eta_{3,3}$. We can then write

$$J_z = \frac{1}{4} (\mathcal{F}_{+3,+3} + \mathcal{F}_{-3,-3} - \mathcal{F}_{+3,-3} - \mathcal{F}_{-3,+3}) \equiv \frac{1}{2} (\mathcal{F}_{\text{AFM}} - \mathcal{F}_{\text{FM}}), \quad (6.10)$$

so J_z directly indicates whether the system energetically favors ferromagnetic ($J_z < 0$) or antiferromagnetic ($J_z > 0$) alignment along the z -axis.

The RKKY coupling J_z is shown in fig. 13. The results are obtained by setting up the BdG Hamiltonian with the appropriate order parameter (or none, for the normal metal), placing two impurities with exchange strength $\mathcal{J} = 3t$ at distinct sites along the x -axis, and evaluating the free energy numerically. J_z exhibits the expected oscillatory, power-law-decaying behavior, with

the normal state (blue) serving as a reference. The s -wave curve (red) and the chiral $p_x + ip_y$ state (orange) closely follow the normal-state result but are shifted towards antiferromagnetism. In contrast, the p_y state (green) is qualitatively indistinguishable from the normal metal. This behavior can be understood from the superconducting gap structure: for s -wave and chiral $p_x + ip_y$ pairing, quasiparticles propagating along the x -axis between the impurities are fully gapped, strongly suppressing low-energy states and enhancing a non-oscillatory, long-ranged AFM condensate contribution to J_z . For the p_y -wave state, quasiparticles moving along x experience no gap, so the RKKY interaction remains essentially normal metallic, in agreement with Ref. [27].

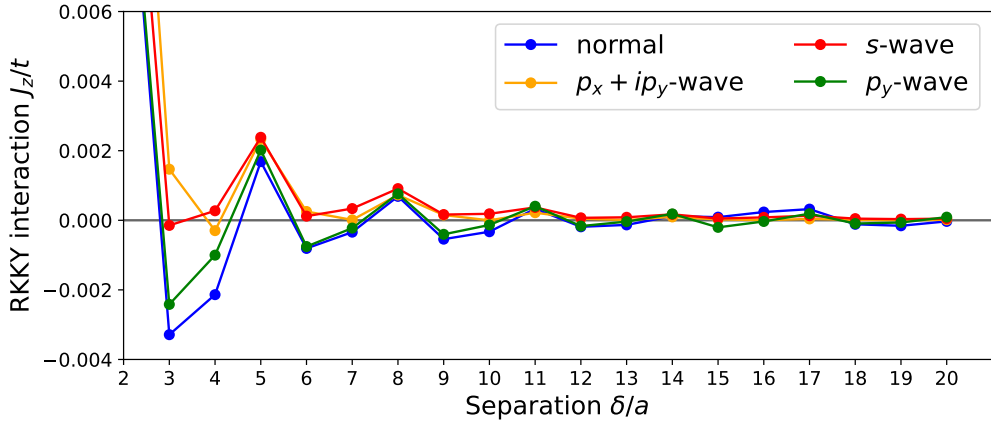


Figure 13: RKKY interaction between two classical spins in a 2D square lattice. Shown is the numerically computed coupling J_z/t as a function of impurity separation $\delta = |R_1 - R_2|$ on a $120a \times 40a$ lattice with chemical potential $\mu = -3t$ and exchange coupling $\mathcal{J} = 3t$. Both spins are placed in the middle of the y -axis; the first impurity is fixed at $x = 40a$, while the second is placed at $x = 40a + \delta$ along the positive x -axis. The free energy is calculated non-self-consistently. The magnitude of the gap for all superconducting cases is $\Delta_0 = 0.1t$ and the temperature is $T = 10^{-4}t$.

6.3 Geometric frustration on a superconducting triangular lattice

Let us now consider three classical spins, \mathbf{s}_1 , \mathbf{s}_2 , \mathbf{s}_3 , placed symmetrically in a triangular lattice with side length $80a$ and with pair-wise distances $\delta_{12} = \delta_{13} = \delta_{23} \equiv \delta$, such that they respect C_3 invariance. To avoid edge and finite size effects we introduce a “padding” region of width $\text{pad} = 20a$ along each edge of the triangular sample used in the simulations. For clarity, a scaled-down version of this geometry is shown in fig. 14.

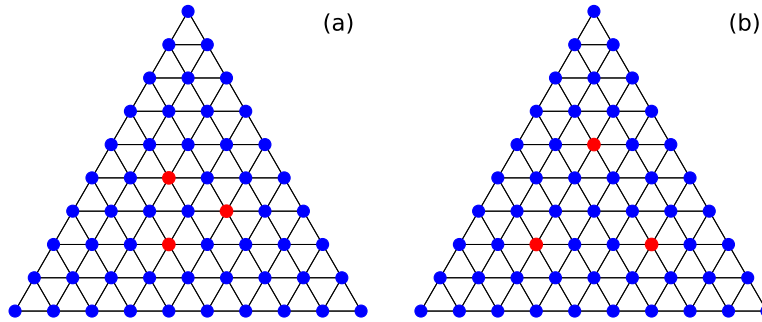


Figure 14: Visualization of triangular lattice with three impurity spins arranged in a C_3 -symmetric configuration. For visibility, we show here a reduced system with side length $10a$, $\text{pad} = 2a$. Blue circles denote ordinary lattice sites, and red circles mark the impurity spins. Panel (a) corresponds to an impurity separation $\delta = \sqrt{3}a$, while panel (b) uses $\delta = 3a$.

Note that in fig. 14(a), there is no direct path connecting the spins, so the distance (in units of the

lattice constant a) is not an integer. This configuration has the added benefit of reducing finite-size effects, since the impurities are not connected by specular reflection paths.

The procedure introduced in the previous subsection for two classical spins can be easily generalized to this three-spin case. To fully characterize the system, we compute the free energy $\mathcal{F}(\mathbf{s}_1, \mathbf{s}_2, \mathbf{s}_3)$ for 216 different spin combinations along each of the cardinal directions and find five parameters $\{\mathcal{F}_0, \boldsymbol{\mu}, \boldsymbol{\eta}_{12}, \boldsymbol{\eta}_{13}, \boldsymbol{\eta}_{23}\}$. In practice, this is implemented by fixing one pair of spins at a time and averaging the free energy over all possible orientations of the third spin. In analogy to the notation introduced earlier in Eq. (6.4), we can define the free energy for 3 spins as

$$\mathcal{F}_{\alpha n, \beta m, \gamma k} \equiv \mathcal{F}(\alpha \hat{\mathbf{e}}_n, \beta \hat{\mathbf{e}}_m, \gamma \hat{\mathbf{e}}_k), \quad (6.11)$$

with $n, m, k \in \{\pm 1, \pm 2, \pm 3\}$ and $\alpha, \beta, \gamma \in \{+, -\}$. Then we can define the averaged quantity

$$\mathcal{F}_{n,m} = \frac{1}{6} \sum_{k=-3}^{+3} \mathcal{F}_{n,m,k}. \quad (6.12)$$

Equation (6.12) can then be used directly to determine the components of the parameters in Eqs. (6.6) and (6.7). We find that in a normal metal, an s -wave (BCS) spin-singlet superconductor, and a chiral p -wave spin-triplet superconductor this geometric configuration gives $\boldsymbol{\eta}_{12} = \boldsymbol{\eta}_{13} = \boldsymbol{\eta}_{23} \equiv \boldsymbol{\eta}$. This symmetry of the interaction strength can lead to geometric frustration. The host materials are chosen because their pairing symmetries are compatible with the triangular-lattice symmetry and are, therefore, stable phases in this geometry.

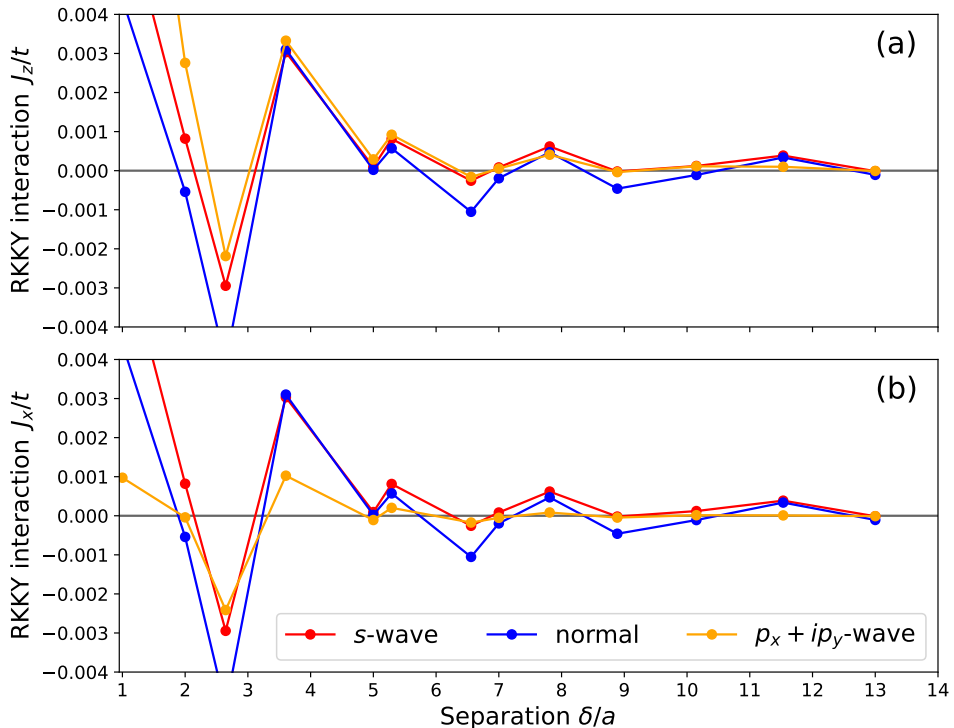


Figure 15: Pairwise RKKY interaction between classical spins in a 2D triangular lattice. Shown in panel (a) is the numerically computed coupling J_z as a function of impurity separation δ on an equilateral triangle with a side length $80a$. Panel (b) shows the coupling $J_x (= J_y)$. Both graphs correspond to chemical potential $\mu = -3t$ and an exchange coupling between impurities and itinerant charges $\mathcal{J} = 3t$. The free energy is calculated non-self-consistently. The magnitude of the superconducting gap for all cases is $\Delta_0 = 0.1t$ and the temperature is $T = 10^{-4}t$.

Our goal is to determine how the ground-state spin configuration evolves as a function of δ . We focus on the emergence of degenerate and non-collinear configurations in such frustrated systems.

To the best of our knowledge, this problem has not been previously investigated. Throughout, we use the same parameters as in fig. 13. As before, we parametrize $\boldsymbol{\eta}$ in terms of \mathbf{J} and \mathbf{D} and substitute the resulting parameter values into Eq. (6.9) to reconstruct the free energy $\mathcal{F}(\mathbf{s}_1, \mathbf{s}_2, \mathbf{s}_3)$. We can, once again, look at the effective interaction J_z against the separation distance for the different materials to see whether we should expect the ground state to be mostly ferromagnetic or antiferromagnetic. Figure 15 shows the typical oscillation between FM and AFM ordering for the normal metal, while the s -wave and $p_x + ip_y$ -wave are skewed towards AFM. The results closely resemble fig. 13; however, due to the geometry of the lattice, each lattice site here has 6 nearest neighbors instead of 4, which leads to a faster decay of the amplitudes. As expected for the Heisenberg interactions in normal metal and s -wave superconductors $J_x = J_z$, while for the Icing chiral p -wave the two values are vastly different.

The optimal spin configuration can now be obtained by minimizing $\mathcal{F}(\mathbf{s}_1, \mathbf{s}_2, \mathbf{s}_3)$ subject to the constraint

$$|\mathbf{s}_1| = |\mathbf{s}_2| = |\mathbf{s}_3| = 1. \quad (6.13)$$

For all of the above mentioned superconducting symmetries, we find that $J_x = J_y$ and $\boldsymbol{\mu}, \mathbf{D} \approx 0$, up to numerical accuracy. Hence, we argue that the free energy is degenerate with respect to rotations in the xy -plane, yielding infinitely many equivalent configurations. We therefore restrict our analysis to spins confined to the xz -plane; parameterizing each spin \mathbf{s}_i terms of some $\theta_i \in [0, 2\pi)$ gives

$$\mathbf{s}_i = [\cos \theta_i, 0, \sin \theta_i]. \quad (6.14)$$

Furthermore, for an isotropic Heisenberg interaction with $J_x = J_y = J_z$, such as the one we observe for normal metals and s -wave superconductors, the free energy is invariant under arbitrary global rotations of all three spins. This additional symmetry implies a continuous degeneracy of the ground state under simultaneous rigid rotations of $(\mathbf{s}_1, \mathbf{s}_2, \mathbf{s}_3)$. To remove this trivial degeneracy, we fix a global spin frame by choosing one of the spins, without loss of generality \mathbf{s}_2 , to point along the positive z -axis. In the parametrization Eq. (6.14), this corresponds to setting $\theta_2 = \pi/2$ and minimizing the free energy only with respect to the remaining spins.

In principle, we can directly use `scipy.optimize.minimize` to minimize the free energy with respect to the angles $\{\theta_i\}$. This parametrization naturally preserves the norm of the spins while allowing us to find the optimal orientation. Since the problem is nonconvex, we try to approach the global minimum (or minima) by repeating the optimization for different initial guesses, choosing $\theta_i \in [0^\circ, 360^\circ]$ on a uniform grid with steps of 30° , and comparing the final energies. In practice; however, because \mathcal{F} is a highly nonlinear function of $\{\theta_i\}$, this strategy is numerically unstable, and the optimization frequently becomes trapped in local minima.

Instead, we implement the optimization procedure described in Ref. [27]. Namely, we convert the constrained optimization problem to an unconstrained one by incorporating the constraints into penalty terms. The objective function we are trying to minimize now becomes

$$\mathcal{G}(\mathbf{s}_1, \mathbf{s}_2, \mathbf{s}_3) = \mathcal{F}(\mathbf{s}_1, \mathbf{s}_2, \mathbf{s}_3) + \lambda (|\mathbf{s}_1^2 - 1| + |\mathbf{s}_2^2 - 1| + |\mathbf{s}_3^2 - 1|) \quad (6.15)$$

For a large enough penalty λ , the constraints are automatically satisfied during the optimization. Again we use `scipy.optimize.minimize` to minimize Eq. (6.15). The penalty is chosen as $\lambda = 10^n$ with $n = 1, 2, \dots, 6$; n is increased between successive calls to the optimizer. This scheme allows the optimizer to explore the energy landscape during the early stages, while strongly imposing the constraints in the final iterations.

In theory, solutions may exist in the full three-dimensional xyz space. Among the symmetry classes we considered, the chiral case is the most likely to admit solutions that are not captured by Eq. (6.14) for any choice of θ_i . To test this numerically, we repeat the same optimization procedure, but now initialize the spins in three dimensions using the spherical coordinate parametrization

$$\mathbf{s}_i = [\cos \theta_i \cos \phi_i, \cos \theta_i \sin \phi_i, \sin \theta_i], \quad (6.16)$$

where $\theta_i \in [0, \pi]$ and $\phi_i \in [0, 2\pi)$. We find that the minimum free energy obtained from initial guesses constrained to the xy -plane coincides with the minimum obtained from fully three-dimensional initial guesses. This agreement supports our original assumption about the structure of the solution.

To validate the method, we first apply the optimization procedure to a normal metal and to an s -wave superconductor, both described by Heisenberg interactions. For these systems, the ground state of an antiferromagnet is known to exhibit a 120° spin configuration in an arbitrary plane [91]. As expected, our procedure reproduces this ordering, as shown in fig. 16. For the chiral superconductor, more interesting patterns emerge. This system is characterized by an Ising interaction, which explicitly distinguishes the x and z spin components. In the ferromagnetic regime, the interaction is dominated by J_x , and the ground state aligns all spins along the $\pm x$ axis. In contrast, in the antiferromagnetic regime the interaction is dominated by J_z , giving rise to various degenerate and noncollinear configurations due to geometric frustration. The spin configurations shown in fig. 16 represent only a subset of the full set of ground states. However, since the spins are equivalent, the additional minima are related to the depicted ones by trivial spin permutations and do not correspond to distinct physical phases.

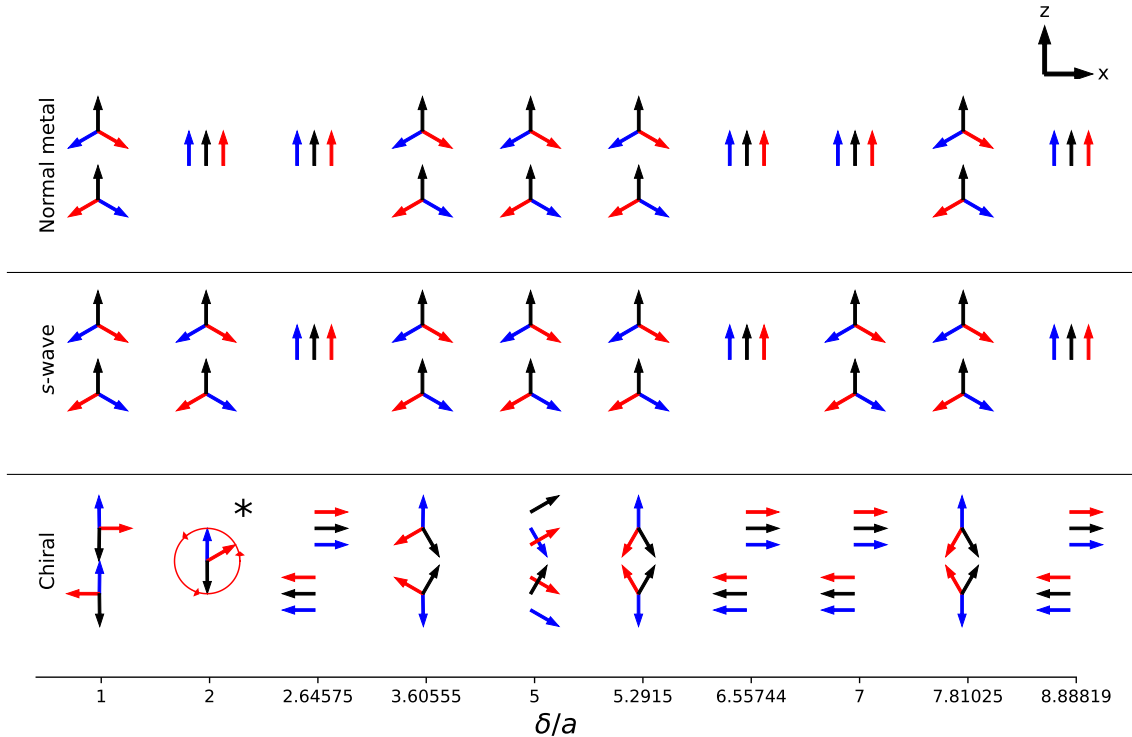


Figure 16: Ground-state spin configurations for three symmetrically placed spins embedded in a normal metal, an s -wave superconductor and a chiral $p_x + ip_y$ -wave superconductor as a function of the separation δ/a . For each configuration the spins $\mathbf{s}_1, \mathbf{s}_2, \mathbf{s}_3$ are shown in blue, black, and red, respectively. In the normal-metal and s -wave cases (Heisenberg exchange) we fix \mathbf{s}_2 along the $+z$ direction. In the chiral case the Ising interaction dominates; all configurations are degenerate under permutations of the three equivalent spins, so only one representative configuration is shown at each δ/a . The configuration marked by “*” has two spins aligned along $\pm \hat{\mathbf{e}}_3$, while the third remains fully degenerate in any direction. Multiple vertically repeated configurations at a given δ/a indicate distinct but degenerate ground states.

The resulting ground states depend sensitively on the relative magnitudes of J_x and J_z . For strong J_z (as in the examples shown for $\delta = a, 2a$), the system strongly favors alignment along the z axis, whereas for larger δ the configurations begin to resemble those of the normal metal and s -wave superconductor, but with a noticeable bias toward the z direction. A particularly interesting configuration at $\delta = 2a$ (indicated by *) is that two of the spins are rigidly pinned along the z axis, while the third remains completely free to orient in any direction, giving rise to a continuous degeneracy of the ground state. Theoretically, for $J_x \ll J_z$ and $\mu = 0$, $\mathbf{D} = \mathbf{0}$, the free energy Eq. (6.9) can be written as

$$\mathcal{F} \approx \mathcal{F}_0 + J_z(\mathbf{s}_1^z \mathbf{s}_2^z + \mathbf{s}_1^z \mathbf{s}_3^z + \mathbf{s}_2^z \mathbf{s}_3^z). \quad (6.17)$$

The lowest possible value of this system satisfying the constraints on the spins is $-J_z$ and can be

achieved, for example, by picking $\mathbf{s}_1^z = +1$ and $\mathbf{s}_2^z = -1$. But inserting this into Eq. (6.17) leads to

$$\mathcal{F} = \mathcal{F}_0 + J_z [(-1)(+1) + (-1)\mathbf{s}_3^z + (+1)\mathbf{s}_3^z] = \mathcal{F}_0 - J_z, \quad (6.18)$$

which is independent of \mathbf{s}_3^z . Thus the third spin is unconstrained and this leads to a complete magnetic frustration, where two spins anti-align while the third is does not have a well defined solution.

At $\delta = 2a$ we find $J_x (= J_y) = -4 \times 10^{-5}t$ and $J_z = 2 \times 10^{-3}t$, so that $|J_x|$ is roughly two orders of magnitude smaller than J_z . For these parameters the system is therefore expected to be close to degeneracy but not fully degenerate. We suspect that there is still a finite set of configurations that minimize the full free energy that is not captured by the optimizer.

To probe this, we adopt a “brute-force” strategy: we evaluate the free energy from Eq. (6.9) for 10^4 initial guesses (per spin) and then manually minimize to extract optimal configurations. This procedure again suggests a degenerate ground state. The most likely explanation is that the variations in \mathcal{F} are very small and lie below the numerical accuracy of the optimization and are effectively indistinguishable. To push the accuracy further, we explicitly construct the full Hamiltonian matrix for a set of configurations: one spin is fixed along $\hat{\mathbf{e}}_3$, while the remaining spins are rotated on a discrete grid in angular steps of 5° . This is substantially more expensive and thus limits the angular resolution, but provides a better accuracy. Within this grid we do not find any configuration with energy lower than the previously identified minimum. Consequently, we are unable to resolve a unique minimizer beyond the apparent degeneracy.

Overall, the consistency between the recovered 120° order in the Heisenberg case gives us a high degree of confidence in the optimization procedure. Repeated runs with different random initial configurations reliably converge to symmetry-related representatives of the same set of minima, and the optimized energies are numerically indistinguishable within our tolerance. We should keep in mind that, in this analysis, we have omitted the Ω term from Eq. (6.9). To quantify the impact of this term, we compute the difference between the free energy obtained directly from Eq. (3.18) and the one reconstructed from Eq. (6.9). The resulting discrepancy is found to be in the range $10^{-6}\text{--}10^{-8}$, i.e., good approximation within reasonable numerical precision. This confirms that the contribution of the Ω term is negligible for the parameter regimes considered here, and thus its omission does not significantly affect our conclusions.

6.4 Concluding remarks

In this section, we have extended the standard two-impurity RKKY formalism to the case of three classical spins embedded in a superconducting triangular lattice, and used self-consistent BdG calculations to extract the corresponding effective exchange couplings. This constitutes, to the best of our knowledge, an original study of the RKKY interaction in a frustrated superconducting geometry. For a normal metal and an s -wave superconductor, where the interaction is essentially Heisenberg-like with $J_x = J_y = J_z$ and negligible \mathbf{D} and Ω , we recover the expected 120° non-collinear ordering on the triangle in the antiferromagnetic regime, see fig. 16. This serves as a stringent benchmark of both the numerical extraction of η_{ij} and the constrained optimization procedure used to determine the ground-state spin textures.

In the chiral $p_x + ip_y$ superconductor, the extracted couplings are strongly anisotropic and well described by an Ising-like interaction with $|J_z| \gg |J_x| = |J_y|$ and vanishing DM terms. In the ferromagnetic regime this anisotropy pins all three spins along the $\pm x$ axis, whereas in the anti-ferromagnetic regime it generates a rich manifold of noncollinear and frustrated configurations. In particular, for separations where $J_z > 0$ and $|J_x| \ll J_z$, we find fully frustrated states in which two spins lock antiferromagnetically along $\pm \hat{\mathbf{e}}_3$, while the third spin remains essentially unconstrained, leading to a continuous degeneracy of the ground state.

These results are not only of conceptual interest for RKKY physics in unconventional superconductors, but also have direct implications for proximity-induced spin-triplet pairing in SF hybrid structures, that we look into closer in the next chapter. These noncollinear ground states and frustrated configurations provide an intrinsic non-collinear exchange texture creating the neces-

sary conditions to convert singlet pairs into spin-polarized triplet Cooper pairs, without the need of externally fabricated magnetic multilayers. Furthermore, by extending the present setup to larger impurity networks, one could in principle design tunable superconducting analogues of frustrated Ising magnets, opening a route toward controllable, proximity-induced implementations of quantum spin liquids and related topological phases [66, 92].

7 Proximity Effect

Proximity structures made of different combinations of superconducting and non-superconducting elements in contact with each other are a topic of current research interest [93, 94]. When a superconductor (S) is placed in proximity with another material, such as a normal metal (N), a ferromagnet (F), an insulator (I), or even a different superconductor, the superconducting order does not end abruptly at the interface. Instead, Cooper pairs “leak” into the adjacent material over a finite length scale, while conversely, the properties of the superconductor near the interface are modified by the presence of the non-superconducting region. This mutual influence is referred to as the *proximity effect*. Such effects can, for example, enhance the critical temperature [36] or induce a Josephson current between superconductors [70].

This section explores proximity effects in hybrid superconducting structures. We begin with SN junctions and Andreev reflection, then discuss Josephson junctions of the SNS type, and finally examine SF junctions where magnetism induces oscillation in the pair correlations in the ferromagnetic region.

7.1 Proximity effect in SN junctions

Cooper pairs are generated inside a superconductor, but are not confined to the interior of the superconductor itself. They also retain phase memory in the normal conducting region. Therefore, the transport properties are determined in detail by the quasiparticle states produced by elastic scattering from inhomogeneities and boundaries. In the presence of superconductivity, a scattering process known as the Andreev reflection [95] occurs, as shown schematically in figure fig. 17. An excited electron incident from the normal conductor with an energy $|\varepsilon| < |\Delta|$ below the superconducting quasiparticle energy gap cannot drain off alone into the superconductor. Instead, it can drag along a second electron at energy $-\varepsilon$ with opposite spin and momentum. The two electrons together create a Cooper pair at the Fermi level. The second electron leaves a hole in the valence band that travels back along the path of the original electron. In a clean system (ballistic limit), the dephasing happens over the coherence length $\xi_N = v_F/T$, with $v_F = k_F/m$ the Fermi velocity and T the temperature, which is taken as the primary source of dephasing.

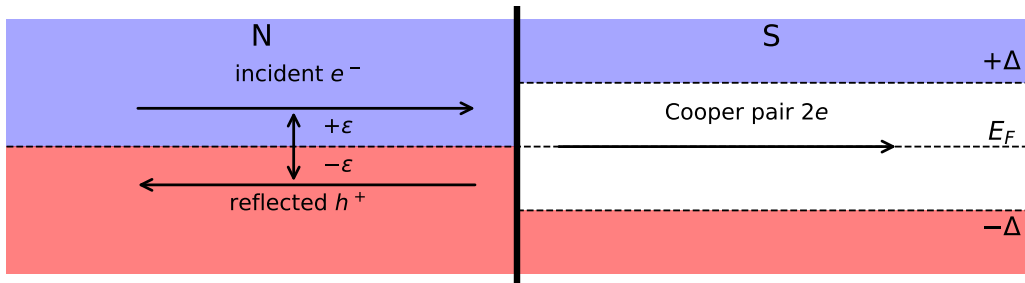


Figure 17: Andreev reflection of an electron with energy ε at the interface of a normal metal and a superconductor with energy gap Δ . The incoming electron itself and the electron taken from valence band enter the superconductor, where they are converted into a Cooper pair.

The reverse process is also possible. If an incoming hole in the valence band meets the interface, it can pull a Cooper pair out of the superconducting condensate. One of the electrons occupies the hole and the other electron occupies an excited state in the conduction band and travels back along the path of the original incoming hole. The induced electrons pair carries superconducting properties along the path of traveling, no longer bound together by the attractive interaction. This correlated pair does not necessarily have exactly opposite momentum and, therefore, dephases even in the absence of pair breaking mechanisms. The coherence length is further shortened by other sources of dephasing, such as inelastic scattering processes and magnetic fields [96]. The largest contribution to the coherence length is based on the dominating energy term of the system. Other terms also enter the expression but their contributions are orders of magnitude smaller; therefore, the coherence length in a clean superconductor with energy gap Δ is $\xi_S = v_F/\pi\Delta$ [97]. It is similar

to its normal metal counterpart, except that in the superconducting regime the energy gap is larger than the thermal excitations [97].

The conceptual description above is often sufficient, but to understand Andreev reflection better we need to look at the microscopic processes that occur when a superconductor is brought into contact with a normal metal. Here we briefly outline these processes. Consider again the diagonalized BCS Hamiltonian, Eq. (5.11). Since the Bogoliubov quasiparticle operators mix electrons and holes, they do not commute with the number operator and thus do not conserve the number of charges. To address this, we adapt the approach in Ref. [74] and introduce the operators $(\hat{S}_k^\dagger, \hat{S}_k)$ that create and annihilate a Cooper pair with electron momenta $(\mathbf{k}, -\mathbf{k})$. The excited states with well defined charge can then be described by

$$\hat{\gamma}_{e,k,\uparrow}^\dagger = u_k^* \hat{c}_{\mathbf{k},\uparrow}^\dagger - v_k^* \hat{S}_k^\dagger \hat{c}_{-\mathbf{k},\downarrow}, \quad (7.1)$$

$$\hat{\gamma}_{h,k,\uparrow}^\dagger = u_k^* \hat{S}_k \hat{c}_{\mathbf{k},\uparrow}^\dagger - v_k^* \hat{c}_{-\mathbf{k},\downarrow}, \quad (7.2)$$

$$\hat{\gamma}_{e,k,\downarrow}^\dagger = u_k^* \hat{c}_{-\mathbf{k},\downarrow}^\dagger - v_k^* \hat{S}_k^\dagger \hat{c}_{\mathbf{k},\uparrow}, \quad (7.3)$$

$$\hat{\gamma}_{h,k,\downarrow}^\dagger = u_k^* \hat{S}_k \hat{c}_{-\mathbf{k},\downarrow}^\dagger - v_k^* \hat{c}_{\mathbf{k},\uparrow}, \quad (7.4)$$

where $u_{\mathbf{k}}$ and $v_{\mathbf{k}}$ satisfy Eqs. (5.8) and (5.9). The operators for electrons and holes are related by

$$\hat{\gamma}_{e,\mathbf{k},\sigma}^\dagger = \hat{S}_k^\dagger \hat{\gamma}_{h,\mathbf{k},\sigma}^\dagger. \quad (7.5)$$

This shows that adding an electron to the superconductor is equivalent to adding a hole and a cooper pair. In the normal metal the superconducting gap is suppressed; in a region where $\Delta_0 = 0$ we have $u_{\mathbf{k}} = 1$, while $v_{\mathbf{k}} = 0$, so the quasiparticle creation operator reduces to the electronic operator, $\hat{\gamma}_{e,\mathbf{k},\sigma}^\dagger \sim \hat{c}_{\mathbf{k},\sigma}^\dagger$. As a charge carrier in the normal metal approaches the interface $v_{\mathbf{k}}$ increases, while $u_{\mathbf{k}}$ decreases. This leads to the excitation no longer being a simple electron but a mixture of electron-like and hole-like excitation with a Cooper pair. When the electron-like excitation reaches the superconductor, it effectively creates a Cooper pair in the condensate and a hole-like excitation with opposite spin and group velocity that propagates back into the metal–this is the Andreev reflection process.

7.2 Josephson junctions (SNS/SIS)

Superconductor–normal-metal–superconductor (SNS) and superconductor–insulator–superconductor (SIS) junctions are typically realized by depositing two superconducting electrodes on a mesoscopic normal conductor. The material used is often a diffusive metal (Cu, Au, Ag) or a semiconductor/2DEG nanowire, separated by a short gap, so that the normal region is phase-coherently proximitized by both superconductors [98]. In a standard planar geometry, a normal nanowire or strip bridges two superconducting banks with good metallic contact. In contrast, SIS junctions have thin insulating layer, usually an oxide layer, between the superconducting electrodes. This results in a tunnel junction with low transparency in which the supercurrent is carried by Cooper-pair tunneling through localized Andreev bound states rather than by extended quasi-particle trajectories in a metallic link.

In this subsection, we consider SNS/SIS-junctions, where the left superconductor has pairing potential $\Delta_L = \Delta e^{-i\varphi/2}$ and the right one $\Delta_R = \Delta e^{i\varphi/2}$. A normal metal/insulator of width W_N is placed in the middle. As shown in fig. 18, an electron meeting the right interface can be reflected as a hole and create a Cooper pair in the right superconductor. The hole will then be reflected as an electron pulling a Cooper pair from the left superconductor. If the phase difference $\varphi \neq 0$, there will be Andreev bound states in the SNS-junction. This process creates a net transfer of Cooper pairs in one direction, giving rise to a *supercurrent*. The effect is known as the *dc Josephson effect*.

The bond current can be derived from the Heisenberg equation of motion for $\langle n_i \rangle = \langle n_{i,\uparrow} \rangle + \langle n_{i,\downarrow} \rangle$ for a system with Hamiltonian \hat{H} [44]:

$$i \frac{\partial \langle n_i \rangle}{\partial t} = \langle [\hat{n}_i, \hat{H}] \rangle = \left\langle \sum_{i \neq j; \sigma\sigma'} \left(t_{ij} \hat{c}_{i,\sigma}^\dagger \hat{c}_{j,\sigma'} - t_{ji} \hat{c}_{j,\sigma'}^\dagger \hat{c}_{i,\sigma} \right) \right\rangle. \quad (7.6)$$

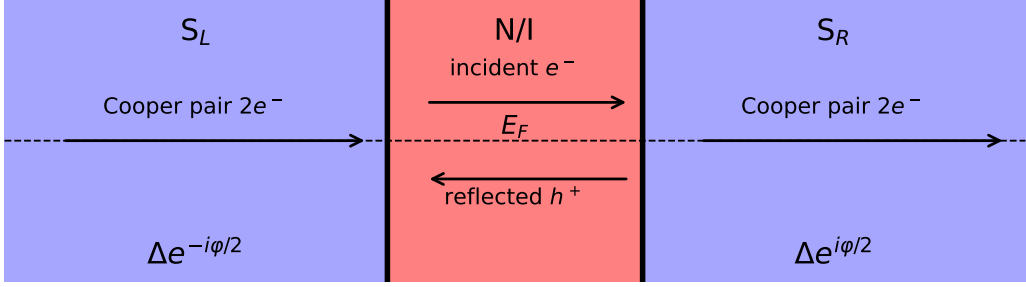


Figure 18: SNS junction. An excited electron reflects off the right interface as a hole, transmitting a charge \$2e\$ to the right superconductor. The hole will then reflect off the left interface as an electron, pulling a charge of \$2e\$ from the left superconductor. A net current between the left and right superconductor can occur depending on the phase difference \$\varphi\$.

Each term in the commutator describes the hopping of an electron between site i and a neighboring site j ; hence it represents the net particle flow along the bond (i, j) . Then we can define of the current operator as

$$\hat{J}_{ij} = \frac{e}{i} \sum_{\sigma, \sigma'} \left(t_{ij} \hat{c}_{i,\sigma}^\dagger \hat{c}_{j,\sigma'} - t_{ji} \hat{c}_{j,\sigma'}^\dagger \hat{c}_{i,\sigma} \right). \quad (7.7)$$

We can now define the local charge density on lattice site i as $\hat{\rho}_i = e \hat{n}_i$. Inserting this definition into Eq. (7.6), we obtain the discrete continuity equation

$$\frac{\partial}{\partial t} \langle \rho_j \rangle + \sum_j \langle J_{ij} \rangle = 0. \quad (7.8)$$

The electric current through the junction can be calculated as the expectation value of the current operator. It can be expressed in terms of the eigenvectors and eigenvalues of the Hamiltonian matrix Eq. (5.50); it is given by

$$\langle J_{ij} \rangle = \frac{e}{i} \sum_{\sigma, \sigma'} \sum_{n > 0} \left[(t_{ij} u_{n,i,\sigma}^* u_{n,j,\sigma'} f(E_n; T) + v_{n,i,\sigma} v_{n,j,\sigma'}^* (1 - f(E_n; T)) - \text{c.c.}) \right] \quad (7.9)$$

$$= \frac{2e}{i} \sum_{\sigma, \sigma'} \sum_{n > 0} \left[(t_{ij} u_{n,i,\sigma}^* u_{n,j,\sigma'} f(E_n; T) - \text{c.c.}) \right] \quad (7.10)$$

$$= \frac{2e}{i} \sum_{\sigma, \sigma'} \sum_{n > 0} \left[(t_{ij} v_{n,i,\sigma} v_{n,j,\sigma'}^* (1 - f(E_n; T)) - \text{c.c.}) \right], \quad (7.11)$$

where in the last two expressions we have used the particle-hole symmetry.

Equation (7.8) expresses local charge conservation: the rate of change of charge at site i is exactly balanced by the total current flowing out through all bonds attached to that site. The formulas in Eqs. (7.9) to (7.11) simply evaluate the expectation value $\langle J_{ij} \rangle$ in the eigenbasis of the Hamiltonian that we can implement numerically.

In the dc Josephson effect a stationary supercurrent flows through a weak link between two superconductors even at zero applied voltage. Each side of the junction can be described by macroscopic wavefunctions. Then the Josephson current is entirely determined by the phase difference between the order parameters on both sides of the junction. For an ideal tunnel junction the current–phase relation is

$$I(\varphi) = I_c \sin \varphi, \quad (7.12)$$

with critical current of the junction I_c . Currents higher than I_c become resistive, generating heat which destroys superconductivity. The sinusoidal dependence makes the Josephson current a nonlinear function of the phase difference, so the junction behaves as an intrinsically nonlinear circuit element. When no voltage is applied, the second Josephson relation

$$\frac{d\varphi}{dt} = 2eV \quad (7.13)$$

implies that $\varphi = \text{constant}$, so that I is time independent. This is the dc Josephson current [31].

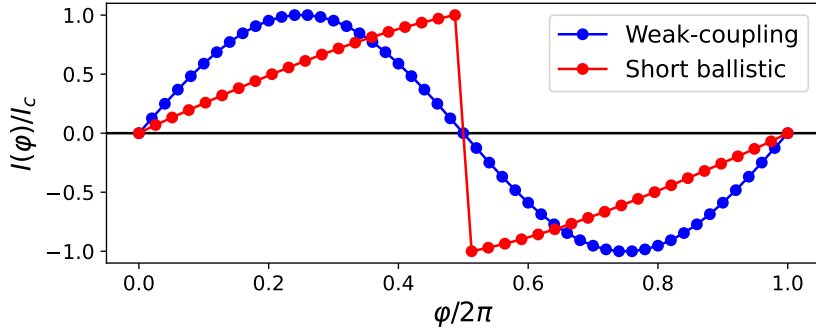


Figure 19: dc Josephson current in a one dimensional junction with total length $L = 128a$ and normal metal slab of thickness $W = 10a$. The curves show the current-phase relation for a SNS junction in the short ballistic limit (red) and the weak-coupling limit (blue). In the weak-coupling case the metal is modeled by reducing the hopping amplitude to $t_I = 0.9t$ in the normal metal bulk and interface. The currents are calculated self-consistently at temperature $T = 10^{-6}t$, keeping the gap constant at the left and right boundaries. Parameters used are chemical potential $\mu = 2t$, pairing potential $U_i = t$ in the superconducting regions, 0 otherwise.

Figure 19 shows different transport regimes of SNS junctions. The weak-coupling case (blue) is close to a purely sinusoidal dependence, $I(\varphi) \propto \sin \varphi$, characteristic of supercurrent through a weak link, where higher harmonics are strongly suppressed and the supercurrent is carried mainly by low-transparency Andreev bound states. On the other hand, in the ballistic limit (red) there is a large contribution from higher harmonics due to the ballistic nature of the normal region. This creates the sawtooth shape with a sharp change of sign near $\varphi \simeq \pi$.

In practice, Josephson junctions are integrated into SQUID loops, superconducting resonators, and hybrid qubits; their relatively large transparency and geometry-tunable nonlinearity make them useful as weakly nonlinear elements in microwave circuits and Andreev-level qubits [31].

7.3 Proximity effect in SF junctions

When a superconductor is placed in proximity to a ferromagnet instead of a normal metal, we have to take into account the spin polarization and exchange energy. The change in spin band associated with Andreev reflection may cause an anomaly in the conductance of ferromagnet–superconductor junctions because the spin-up and the spin-down bands in the ferromagnet are different. The Andreev reflection can even be fully blocked due to the absence of a complete spin band, for 100% spin polarization. The ferromagnetic coherence length is defined as $\xi_F = v_F/E_{\text{ex}}$, with splitting energy $E_{\text{ex}} = 2|\mathbf{m}|$, as described in Eq. (4.10). E_{ex} is typically of order T_C , the Curie temperature, dominates and the length is much shorter than in a normal metal, fig. 20. Incoming electrons and the corresponding reflected holes in a ferromagnet experience a potential energy difference between spin-up and spin-down, while the total energy is fixed. This means that the kinetic energy of a particle in the minority spin band is less than that of the majority spin band. Hence, the Cooper pair will have a net momentum, leading to an oscillation [99] further destabilizing the pair. This effect is often significant. In very clean normal metals this can reach hundreds of micrometers at low T , so superconductivity can penetrate deeply into the N region. Ferromagnets, on the other hand, can have much higher Curie temperatures, with iron, for example, having $T_c \approx 1000$ K. This results in the proximity-induced Cooper pairs in the ferromagnet decaying only over a few nanometers.

It can be interesting to examine how the exchange field affects the spin-singlet state using Dirac notation. For a spin-up ($|\uparrow\rangle$) and spin-down ($|\downarrow\rangle$), we write the singlet $\Psi^{(S)}$ and opposite-spin

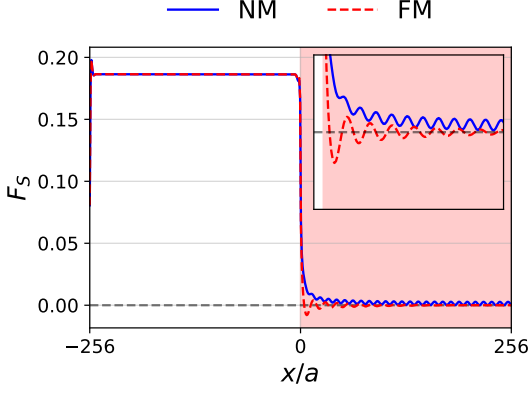


Figure 20: Spatial pair correlation profiles F_S in a one-dimensional junction between a BCS superconductor and either a normal metal (NM, blue solid line) or a ferromagnet (FM, red dashed line). The total system length is $L = 512a$ and the NM/FM slab has width $W = 256a$. The pair correlations are obtained self-consistently for an attractive on-site interaction $U = 2t$ confined to the superconducting region (zero elsewhere), chemical potential $\mu = 1.5t$, temperature $T = 10^{-6}t$. The NM/FM part of the system is shaded in red, while the superconducting region is left clear. The inset magnifies the interface region, emphasizing the damped oscillatory behavior of F_S in the ferromagnetic case.

latory behavior of F_S in the ferromagnetic case. Note that there is a small additional oscillation due to finite size effects and is not representative of physical properties of the system.

triplet $\Psi_0^{(T)}$ states (up to normalization) as

$$\Psi^{(S)} = |\uparrow\downarrow\rangle - |\downarrow\uparrow\rangle \quad \text{and} \quad \Psi_0^{(T)} = |\uparrow\downarrow\rangle + |\downarrow\uparrow\rangle. \quad (7.14)$$

Consider exchange field in the z -direction, with strength m . As defined in Eq. (4.12), the energy of each state is

$$\hat{H}_M |\uparrow\rangle = (\xi_k - m) |\uparrow\rangle = E_\uparrow |\uparrow\rangle, \quad \hat{H}_M |\downarrow\rangle = (\xi_k + m) |\downarrow\rangle = E_\downarrow |\downarrow\rangle. \quad (7.15)$$

Proximity induced Cooper pairs with electrons coming in at an incident angle θ , into a ferromagnet experience a potential energy difference between spin up and spin down, while the total energy is fixed. This means that the kinetic energy, and thus, the momenta will differ,

$$k_{F\uparrow} = k_F + \delta k, \quad k_{F\downarrow} = k_F - \delta k, \quad \delta k = \frac{E_{\text{ex}}}{2v_F \cos \theta}, \quad (7.16)$$

where v_F is the Fermi velocity. The state $|\uparrow\downarrow\rangle$ acquires a center-of-mass momentum $+Q$, while $|\downarrow\uparrow\rangle$ acquires $-Q$, where we have defined $Q = 2\delta k$ [99]. Thus, after propagating a distance x the states pick up opposite spatial phases,

$$|\uparrow\downarrow\rangle \rightarrow e^{-iQx} |\uparrow\downarrow\rangle, \quad |\downarrow\uparrow\rangle \rightarrow e^{+iQx} |\downarrow\uparrow\rangle. \quad (7.17)$$

The time evolution of the spin singlet state is given by

$$\begin{aligned} \Psi^{(S)}(x) &= e^{-iQx} |\uparrow\downarrow\rangle - e^{+iQx} |\downarrow\uparrow\rangle \\ &= \Psi^{(S)} \cos(Qx) - i\Psi_0^{(T)} \sin(Qx). \end{aligned} \quad (7.18)$$

We see that the singlet state actually oscillates between a singlet and a triplet component with a period $P = 2\pi/Q$ as it propagates through the ferromagnet [100]. In other words, a homogeneous exchange field leads to the generation of correlated spin triplet pairs. For that reason, ferromagnetic interfaces can be used to couple singlet and triplet superconductors [36, 38], that otherwise do not interact [37]. However, this coupling alone generates only opposite-spin triplet pairs of the form $(|\uparrow\downarrow\rangle + |\downarrow\uparrow\rangle)$. Equal-spin triplets can be obtained by considering these states in a rotated spin basis. While the singlet state is invariant under rotations of the spin quantization axis, the three triplet components mix into one another under such rotations. For example, the mixed-spin triplet state along the y -axis $(|\uparrow\downarrow\rangle + |\downarrow\uparrow\rangle)_y$, is the same as $(|\uparrow\uparrow\rangle + |\downarrow\downarrow\rangle)_z$ along the z -axis. Equal-spin triplets can then be obtained by exposing the opposite-spin triplets to multiple noncollinear exchange-field directions. Such effective fields can arise from inhomogeneous magnetism, for example, due to magnetic domains or impurities. The noncollinear ground states and frustrated configurations uncovered in section 6 provide precisely this type of intrinsic, noncollinear exchange texture. Embedding the corresponding impurity arrangements in SF heterostructures would thus realize the necessary conditions to convert singlet pairs into spin-polarized triplet Cooper pairs.

Because the equal-spin triplet component aligns with the local exchange field, it does not experience exchange splitting. Consequently, the coherence length in the ballistic limit for the same spin-triplet component in the ferromagnet is therefore $\xi_{FT} \sim v_F/T$ [101]. Since the exchange energy is usually much higher than the superconductor transition temperature the resulting equal-spin triplet component penetrates deeply into the ferromagnet and produces a notable increase in its conductance below the superconducting critical temperature T_c .

Ferromagnets can also be placed between two superconductors to create another type of Josephson junction. As we have shown earlier in this chapter, in an SF junction the spin splitting of the electron states in the ferromagnet leads to spatial modulation of the proximity-induced pair amplitudes due to Cooper pairs with a finite center-of-mass momentum. When this effect is combined with the Josephson effect, it leads to the so-called π -junction [31, 102]. In such system the pairing amplitudes on both sides of the junctions will have a phase difference of 0 or π depending on the length of the junction.

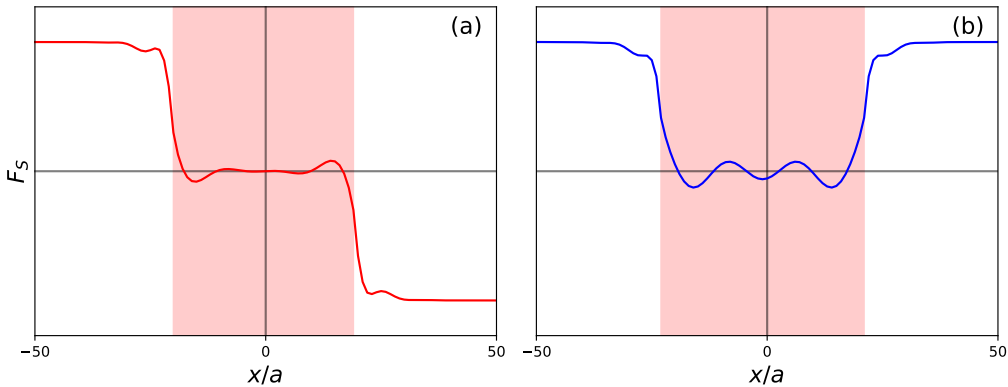


Figure 21: Spatial pair correlation profiles F_S in a one-dimensional SFS junction where the ferromagnet (shaded in red) is placed between two BCS superconductors. The total length of the system is $L = 256a$, but the panels focus on the central region near the interfaces. The red shaded area marks the ferromagnetic layer, whose total thickness is $W = 40a$ in (a) and $W = 45a$ in (b). The Cooper-pair correlations are obtained from fully self-consistent calculations with attractive potential $U = t$, chemical potential $\mu = 1.9t$, temperature $T = 10^{-4}t$ and exchange field $\mathbf{m} = 0.1t\hat{\mathbf{e}}_3$.

The correlations in fig. 21 are obtained self-consistently for initial guess for the gap $\Delta_0 = \pm 10^{-4}t$. For each solution we calculate the free energy \mathcal{F} using Eq. (3.18) in order to identify the ground state solution and distinguish it from a local minimum. In fig. 21(a) we show a π -junction where the singlet pair amplitude F_S changes sign between the two superconductors, so that the ground state of the junction corresponds to a phase difference of π . This sign reversal is a direct consequence of the oscillatory decay of the singlet correlations inside the ferromagnet. For the thickness $W = 40a$ used in panel (a), the ferromagnetic region is too small for F_S to complete a full oscillation period so at the right S/F interface, it acquires the opposite sign to that at the left one. In panel (b), where the ferromagnet is slightly thicker, $W = 45a$, the correlations undergo an additional phase advance and recover the same sign on both sides of the junction, yielding a 0-junction. In both cases the red shaded region clearly illustrates the rapid oscillatory decay of F_S inside the ferromagnet compared to the nearly constant behavior in the superconductors. The damping of these oscillations reflects the finite coherence length in the magnetic layer.

7.4 Concluding remarks

In this section we present the most common proximity systems, in particular SN. In this chapter we have established the basic framework for understanding proximity effects in hybrid superconducting structures and their manifestation in Josephson junctions of various types. Starting from the simplest SN, SI, and SF bilayers, we have seen how a superconducting condensate can leak into an adjacent non-superconducting material, modifying both the local order parameter and the quasiparticle spectrum. In particular, we have emphasized that this leakage is not merely an

exponential decay governed by a coherence length, but in the presence of exchange fields can acquire an intrinsically oscillatory character. Building on this, we have extended the discussion to Josephson junctions of the SNS and SFS types. For SNS junctions, the supercurrent is well captured at low energies by the standard current–phase relation. In SFS junctions, however, the same oscillatory proximity effect present in SF bilayers has a profound consequence. Depending on the thickness of the ferromagnetic interlayer is varied, the pair amplitude acquires a ground-state phase π across the F region leading to a sign change.

8 Conclusions and Outlook

In this project, we first reviewed the tight-binding formalism and the extended Hubbard model, and summarized the microscopic mechanisms that underlie ferromagnetism and superconductivity. On this basis, we derived the real-space Bogoliubov–de Gennes (BdG) equations for a broad class of superconducting and magnetic systems, thereby establishing a unified framework applicable to both conventional and unconventional pairing. The formulation accommodates the presence or absence of an exchange field, and thus describes superconductors coexisting with magnetism as well as purely nonmagnetic phases. Furthermore, it applies to both bulk systems and proximity structures, as demonstrated in section 7, making it well suited for modeling realistic heterostructures with experimentally relevant parameters.

A central component of the work is the numerical implementation of this real-space BdG framework. We developed computational routines to construct and diagonalize the lattice Hamiltonians and to evaluate key observables, including the local density of states and Cooper-pair correlations. This implementation renders the formalism operational and enables systematic exploration of superconducting and magnetic lattice models across a range of geometries and parameter regimes.

In addition to the BdG equations, we have derived the corresponding self-consistency conditions for the superconducting order parameter within this real-space formulation. These gap equations provide the link between the microscopic pairing interaction and the emergent superconducting state, and are essential for capturing feedback effects between the quasiparticle spectrum and the order parameter profile. This establishes the infrastructure needed for future self-consistent studies of more complex proximity structures and unconventional pairing states.

As a first application, in section 5.6 we solved the BdG equations numerically for a conventional BCS superconductor and obtained the local density of states, the superconducting gap, and the critical temperature. The results were verified by confirming that the BCS ratio $2\Delta(0)/T_c$ is consistent with the expected value. In section 5.7 we diagonalized the BdG equations for unconventional superconductors in order to analyze the local density of states and the emergence of edge states.

An original contribution of this work is the study of frustrated magnetism arising from RKKY-mediated interactions between three localized spins placed symmetrically on a triangular lattice. This setup provides a minimal yet nontrivial geometry in which competing exchange couplings lead to frustrated ground states. Using the developed framework, we have implemented the RKKY interaction to investigate magnetism mediated by superconducting quasiparticles and verified our implementation by reproducing known results in simpler geometries. Our calculations demonstrate the emergence of nontrivial degenerate and non-collinear ground-state configurations in the frustrated triangular setup. In the chiral regime with inter-spin distance $\delta = 2a$, no unique set of minimizing configurations is resolved, consistent with an effectively degenerate ground state. It is plausible that this apparent degeneracy conceals a discrete set of true ground states whose energy splittings lie below the present numerical resolution. Therefore, a natural next step is to increase numerical precision and employ complementary approaches, such as Monte Carlo sampling of the spin configuration space, to refine the free energy landscape and determine whether the degeneracy is genuine or weakly lifted.

In section 7 we formulated proximity systems within the same framework and applied the method to superconducting correlations across interfaces. Fully self-consistent calculations of singlet Cooper-pair correlations in SN and SF junctions resolve their spatial evolution in the non-superconducting regions. The correlations decay exponentially in a normal metal, whereas in a ferromagnet they exhibit spatial oscillations. Using the same self-consistent scheme, we also computed the Josephson current in an SNS junction, thereby relating microscopic pairing correlations to the macroscopic current–phase relation and illustrating the applicability of the approach to realistic proximity devices.

A direction for future work is to extend the numerical framework to fully accommodate unconventional self-consistency conditions. To achieve this we need to allow the coexistence of multiple superconducting orders. This implies handling several coupled gap components, such as singlet

and triplet, or different triplet channels, that may transform according to distinct irreducible representations and mix in the presence of magnetism. In addition, we need to verify the robustness and convergence of the method in such complex system. Accomplishing these tasks will enable us to systematically study magnetically coupled proximity structures involving high-temperature and exotic triplet superconductors. We can then quantify the conditions under which triplet components are stabilized, and assess the whether it is possible to realize meaningful improvement in realistic device geometries.

Description of Use of Artificial Intelligence

In working on this project, I have used artificial intelligence (AI) tools in the following ways: I used ChatGPT to refine the language and suggest phrasing, but all content has been reviewed, edited, and academically assessed by me. I used Microsoft's Copilot with NTNU license to proofread the text. Numerically AI assistance (GitHub Copilot) was sometimes used to comment the code and to aid in the customization of plots. I have used the autocomplete function of the Github Copilot Extension in VS Code. AI was NOT used to generate entire paragraphs or to write this thesis in its entirety. AI was NOT used to generate data or provide analysis. I am solely responsible for the content of this work.

A Extended Hubbard Model in Mixed Real–Momentum Space

A common way to model systems with an interface parallel to one axis, i.e. the x -axis, is to adopt periodic boundary conditions along the y -direction. Under this assumption, we can define $k = 2\pi n/L$, for $n \in \mathbb{Z}$ and L is the number of sites in the y -direction. The Fourier transform of the fermionic creation and annihilation operators is given by

$$\hat{c}_{j,\sigma} = \frac{1}{\sqrt{L_y}} \sum_k \hat{c}_{j,k,\sigma} e^{ikL_y}, \quad (\text{A.1})$$

$$\hat{c}_{j,\sigma}^\dagger = \frac{1}{\sqrt{L_y}} \sum_k \hat{c}_{j,k,\sigma}^\dagger e^{-ikL_y}, \quad (\text{A.2})$$

where j is the site position along the x direction. Inserting this into Eq. (5.46), we obtain the following terms:

$$\hat{H}_\mu = - \sum_{i,k,\sigma} \mu_i \hat{c}_{i,k,\sigma}^\dagger \hat{c}_{i,k,\sigma}, \quad (\text{A.3})$$

$$\hat{H}_t = -t \sum_{i,j,k,\sigma} \hat{c}_{i,k,\sigma}^\dagger \hat{c}_{j,k,\sigma} (\delta_{i,j+1} + \delta_{i,j-1} + 2 \cos(ka) \delta_{ij}), \quad (\text{A.4})$$

$$\hat{H}_M = \sum_{i,k,\sigma,\sigma'} \hat{c}_{i,k,\sigma}^\dagger [\mathbf{S} \cdot \mathbf{m}_i]_{\sigma,\sigma'} \hat{c}_{i,k,\sigma'}. \quad (\text{A.5})$$

$$H_U = - \sum_{i,k} \left(\Delta_i \hat{c}_{i,k,\uparrow}^\dagger \hat{c}_{i,-k,\downarrow}^\dagger + \Delta_i^\dagger \hat{c}_{i,-k,\downarrow} \hat{c}_{i,k,\uparrow} \right), \quad (\text{A.6})$$

$$H_V = \sum_{i,j,k} V_i \left[\left(F_j^{+\hat{x}} \delta_{i,j+1} + F_j^{-\hat{x}} \delta_{i,j-1} + (F_i^{+\hat{y}} e^{-ika} + F_i^{-\hat{y}} e^{ika}) \delta_{ij} \right) \hat{c}_{i,k,\downarrow}^\dagger \hat{c}_{j,-k,\uparrow} + \text{h.c.} \right], \quad (\text{A.7})$$

$$H_{V'} = \sum_{i,j,k} V'_i \left[\left(F_{j,\sigma\sigma}^{+\hat{x}} \delta_{i,j+1} + F_{j,\sigma\sigma}^{-\hat{x}} \delta_{i,j-1} + 2i F_{i,\sigma\sigma}^{+\hat{y}} \sin(ka) \delta_{ij} \right) \hat{c}_{i,k,\sigma}^\dagger \hat{c}_{j,-k,\sigma} + \text{h.c.} \right], \quad (\text{A.8})$$

where we have assumed isotropic $t_{ij} = t$ and a is the lattice constant. We have used that $F_{i,\sigma\sigma}^{+\hat{y}} = -F_{i,\sigma\sigma}^{-\hat{y}}$ [74]. The benefit of this formulation is that the Hamiltonian is already diagonal along the y -axis, reducing the complexity of the problem. The approach here is similar to section 5, we write the full Hamiltonian as

$$\hat{H} = E_0 + \frac{1}{2} \sum_{i,j,k} \hat{\mathbf{c}}_{i,k}^\dagger \hat{\mathbf{H}}_{ijk} \hat{\mathbf{c}}_{j,k} \quad (\text{A.9})$$

by considering the basis $\hat{\mathbf{c}}_{i,k}^\dagger = [\hat{c}_{i,k,\uparrow}^\dagger, \hat{c}_{i,k,\downarrow}^\dagger, \hat{c}_{i,k,\uparrow}, \hat{c}_{i,k,\downarrow}]$. The matrix $\hat{\mathbf{H}}_{ijk}$ can be explicitly written as

$$\hat{\mathbf{H}}_{ijk} = \begin{bmatrix} \xi_{ijk} + m_i^z \delta_{ij} & (m_i^x + im_i^y) \delta_{ij} & \Lambda_{ijk}^{\uparrow\uparrow} & \Lambda_{ji-k} \\ (m_i^x - im_i^y) \delta_{ij} & \xi_{ijk} - m_i^z \delta_{ij} & \Lambda_{ijk} & \Lambda_{ijk}^{\downarrow\downarrow} \\ \Lambda_{jik}^{\uparrow\uparrow*} & \Lambda_{jik}^* & -\xi_{ijk} - m_i^z \delta_{ij} & -(m_i^x - im_i^y) \delta_{ij} \\ \Lambda_{ijk}^* & \Lambda_{ijk}^{\downarrow\downarrow*} & -(m_i^x + im_i^y) \delta_{ij} & -\xi_{ijk} + m_i^z \delta_{ij} \end{bmatrix}, \quad (\text{A.10})$$

with

$$\xi_{ijk} = -2t (\cos(k) - \mu_i) \delta_{i,j} - t (\delta_{i,j+1} + \delta_{i,j-1}), \quad (\text{A.11})$$

$$\Lambda_{ijk} = V_i \left[F_j^{+\hat{x}} \delta_{i,j+1} + F_j^{-\hat{x}} \delta_{i,j-1} + (F_i^{+\hat{y}} e^{-ika} + F_i^{-\hat{y}} e^{ika}) \delta_{ij} \right], \quad (\text{A.12})$$

$$\Lambda_{ijk}^{\sigma\sigma} = V'_i \left[F_{j,\sigma\sigma}^{+\hat{x}} \delta_{i,j+1} + F_{j,\sigma\sigma}^{-\hat{x}} \delta_{i,j-1} - 2i \sin(ka) F_{i,\sigma\sigma}^{+\hat{y}} \delta_{ij} \right]. \quad (\text{A.13})$$

We can further compactify the problem by writing the creation and annihilation operators in Lattice \otimes Nambu \otimes Spin basis as $\check{\mathbf{c}}_k^\dagger = [\check{c}_{1,k}^\dagger, \check{c}_{2,k}^\dagger, \dots, \check{c}_{L_x,k}^\dagger]$. We can then write the Hamiltonian operator as

$$\hat{H} = E_0 + \frac{1}{2} \sum_k \check{\mathbf{c}}_k^\dagger \check{\mathbf{H}}_k \check{\mathbf{c}}_k. \quad (\text{A.14})$$

As before, we diagonalize $\check{\mathbf{H}}_k$ to obtain the Bogoliubov quasiparticle ladder operators, (γ, γ^\dagger) ,

$$\hat{H} = E_0 + \frac{1}{2} \sum_k \check{\gamma}_k^\dagger \check{D}_k \check{\gamma}_k = E_0 + \frac{1}{2} \sum_{n,k} E_{nk} \gamma_{n,k}^\dagger \gamma_{n,k} \quad (\text{A.15})$$

The Bogoliubov annihilation operator can be explicitly written as

$$\gamma_{n,k} = \sum_{i,\sigma} \left(u_{n,i,k,\sigma}^* \hat{c}_{i,k,\sigma} + v_{n,i,k,\sigma}^* \hat{c}_{i,k,\sigma}^\dagger \right), \quad (\text{A.16})$$

where $u_{n,i,k}$ is electron spinor and $v_{n,i,k}$ is hole spinor, and can be obtained from the eigenvectors of $\check{\mathbf{H}}_k$. As shown in Eq. (5.52), there is symmetry between particles and holes, as well as between quasiparticles with momentum $+k$ and $-k$ imposed by the Cooper pairs. Taking these symmetries into account, we split the sum over k in Eq. (A.15) in three parts: $k > 0$, $k < 0$ and $k = 0$. We then write

$$\hat{H} = E_0 + \sum_{n,k \geq 0} E_{nk} \left(\gamma_{n,k}^\dagger \gamma_{n,k} - \frac{1}{2} \right). \quad (\text{A.17})$$

We can now set up a self-consistent problem by defining the Δ_i , $F_j^{\pm\hat{x}(\hat{y})}$ and $F_{j,\sigma,\sigma}^{\pm\hat{x}(\hat{y})}$ in terms of the eigenvalues and eigenvectors of \hat{H} .

$$\Delta_i(T) = \frac{U_i}{L_y} \sum_{n,k \geq 0} (v_{n,i,k,\uparrow}^* u_{n,i,k,\downarrow} f(E_n; T) + u_{n,i,k,\uparrow} v_{n,i,k,\downarrow}^* [1 - f(E_n; T)]) \quad (\text{A.18})$$

$$F_i^{\pm\hat{x}}(T) = \sum_{n,k \geq 0} (u_{n,i,k,\uparrow} v_{n,i\pm\hat{x},k,\downarrow}^* [1 - f(E_n; T)] + v_{n,i,k,\uparrow}^* u_{n,i\pm\hat{x},k,\downarrow} f(E_n; T)), \quad (\text{A.19})$$

$$F_i^{\pm\hat{y}}(T) = \sum_{n,k \geq 0} (u_{n,i,k,\uparrow} v_{n,i,k,\downarrow}^* [1 - f(E_n; T)] e^{\pm ika} + v_{n,i,k,\uparrow}^* u_{n,i,k,\downarrow} f(E_n; T) e^{\mp ika}), \quad (\text{A.20})$$

$$F_{i,\sigma\sigma}^{\pm\hat{x}}(T) = \sum_{n,k \geq 0} (u_{n,i,k,\sigma} v_{n,i\pm\hat{x},k,\sigma}^* [1 - f(E_n; T)] + v_{n,i,k,\sigma}^* u_{n,i\pm\hat{x},k,\sigma} f(E_n; T)), \quad (\text{A.21})$$

$$F_{i,\sigma\sigma}^{\pm\hat{y}}(T) = \sum_{n,k \geq 0} (u_{n,i,k,\sigma} v_{n,i,k,\sigma}^* [1 - f(E_n; T)] e^{\pm ika} + v_{n,i,k,\sigma}^* u_{n,i,k,\sigma} f(E_n; T) e^{\mp ika}). \quad (\text{A.22})$$

B Bisection Algorithm for Critical Parameter Search

In many physical systems, the system undergoes a qualitative change when a parameter crosses a critical threshold. Examples include the onset of magnetization in ferromagnets at the Curie temperature, or the disappearance of the superconducting gap at the critical temperature T_c . The Bisection algorithm [103, 104] offers a robust and numerically efficient approach to find this critical value. It guarantees convergence provided that the initial bounds enclose the true critical point and the order parameter changes monotonically near some critical parameter value p_c . The algorithm relies on a simple iterative procedure to bracket this critical parameter within a predefined tolerance. The bisection algorithm provides a logarithmic speedup over linear search, since it runs in $O(\log n)$ time compared to $O(n)$ in the worst case for a linear search.

In a general setting, the algorithm can be applied to any system described by a Hamiltonian H that depends on a control parameter p —such as temperature, pressure, interaction strength, or external field. At each iteration, the system is evaluated at the midpoint value p_{half} using an appropriate solver (e.g., self-consistent field equations or Bogoliubov–de Gennes equations). The response of an order parameter Φ (for instance, the superconducting gap Δ , magnetization M , or density difference ρ) is then used to determine whether the system resides in one phase or another, and the parameter bounds are updated accordingly.

Algorithm 1 Critical Parameter Search via Bisection Method

GOAL: To find a solution to $f(p) = 0$ given the continuous function f on the interval $[a, b]$, where $f(p_{\min})$ and $f(p_{\max})$ have opposite signs:
INPUT: Parameter bounds p_{\min} and p_{\max} ; initial order parameter guess $\Phi_0 \ll 1$; tolerance tol , maximum iterations max_iter , system solver f
OUTPUT: Approximate solution p or failure

```

1:  $p_c \leftarrow 0$                                 ▷ Initialize critical parameter estimate
2: for  $n \leftarrow 1$  to  $\text{max\_iter}$  do
3:    $p_{\text{half}} \leftarrow (p_{\max} + p_{\min})/2$           ▷ Bisection midpoint
4:    $\Phi_{\text{new}} \leftarrow f(p_{\text{half}})$                 ▷ Evaluate order parameter at midpoint
5:   if  $\Phi_0 < \Phi_{\text{new}}$  then
6:      $p_{\min} \leftarrow p_{\text{half}}$                       ▷ Order parameter increases: search higher values.
7:   else
8:      $p_{\max} \leftarrow p_{\text{half}}$                       ▷ Order parameter decreases: search lower values.
9:   end if
10:  if  $|p_{\text{half}} - p_c| < \text{tol}$  then
11:     $p_c \leftarrow p_{\text{half}}$                           ▷ Convergence achieved
12:     $\text{success} \leftarrow \text{True}$ 
13:    break
14:  end if
15:   $p_c \leftarrow p_{\text{half}}$                           ▷ Update current best estimate
16: end for
17: if  $\text{success}$  then
18:   OUTPUT( $p_c$ )
19: else
20:   OUTPUT('Method failed after  $\{\text{max\_iter}\}$  iterations'.)
21: end if

```

The algorithm begins with an initial interval $[p_{\min}, p_{\max}]$ that brackets the expected critical value. The midpoint p_{half} is used to evaluate the system's order parameter. If the order parameter indicates the presence of the ordered phase (e.g., $\Phi_{\text{new}} > \Phi_0$), the lower bound is updated; otherwise, the upper bound is reduced. This iterative procedure continues until the estimated critical parameter p_c changes by less than the desired tolerance tol .

Bibliography

- [1] H. Kamerlingh Onnes. ‘Leiden Communications No. 120b, 122b, 124c’. In: *Communications from the Physical Laboratory of the University of Leiden* (1911).
- [2] Dirk van Delft and Peter Kes. *The Discovery of Superconductivity*. URL: https://www.lorentz.leidenuniv.nl/history/cold/DelftKes_HKO_PT.pdf.
- [3] W. Meissner and R. Ochsenfeld. ‘Ein neuer Effekt bei Eintritt der Supraleitfähigkeit’. In: *Die Naturwissenschaften* 21.44 (Nov. 1933), pp. 787–788. ISSN: 0028-1042, 1432-1904. DOI: 10.1007/BF01504252.
- [4] J. Bardeen, L. N. Cooper and J. R. Schrieffer. ‘Theory of Superconductivity’. In: *Physical Review* 108.5 (Dec. 1957), pp. 1175–1204. ISSN: 0031-899X. DOI: 10.1103/PhysRev.108.1175.
- [5] J. G. Bednorz and K. A. Müller. ‘Possible highT_c Superconductivity in the Ba-La-Cu-O System’. In: *Zeitschrift für Physik B Condensed Matter* 64.2 (June 1986), pp. 189–193. ISSN: 1431-584X. DOI: 10.1007/BF01303701.
- [6] K. Alex Müller and J. Georg Bednorz. ‘The Discovery of a Class of High-Temperature Superconductors’. In: *Science* 237.4819 (Sept. 1987), pp. 1133–1139. ISSN: 0036-8075, 1095-9203. DOI: 10.1126/science.237.4819.1133.
- [7] Zi-Kui Liu and Shun-Li Shang. ‘Revealing Symmetry-Broken Superconducting Configurations by Density Functional Theory’. In: *Superconductor Science and Technology* 38.7 (July 2025), p. 075021. ISSN: 0953-2048, 1361-6668. DOI: 10.1088/1361-6668/adedbc.
- [8] A. P. Drozdov et al. ‘Superconductivity at 250 K in Lanthanum Hydride under High Pressures’. In: *Nature* 569.7757 (May 2019), pp. 528–531. ISSN: 1476-4687. DOI: 10.1038/s41586-019-1201-8.
- [9] D. D. Osheroff, R. C. Richardson and D. M. Lee. ‘Evidence for a New Phase of Solid He 3’. In: *Physical Review Letters* 28.14 (Apr. 1972), pp. 885–888. ISSN: 0031-9007. DOI: 10.1103/PhysRevLett.28.885.
- [10] P. W. Anderson and W. F. Brinkman. ‘Anisotropic Superfluidity in He 3 : A Possible Interpretation of Its Stability as a Spin-Fluctuation Effect’. In: *Physical Review Letters* 30.22 (May 1973), pp. 1108–1111. ISSN: 0031-9007. DOI: 10.1103/PhysRevLett.30.1108.
- [11] M. C. Cross. ‘Orbital Dynamics of the Anderson-Brinkman-Morel Phase of superfluid 3He’. In: *Journal of Low Temperature Physics* 26.1-2 (Jan. 1977), pp. 165–191. ISSN: 0022-2291, 1573-7357. DOI: 10.1007/BF00654566.
- [12] D. Fay and J. Appel. ‘Coexistence of p -State Superconductivity and Itinerant Ferromagnetism’. In: *Physical Review B* 22.7 (Oct. 1980), pp. 3173–3182. ISSN: 0163-1829. DOI: 10.1103/PhysRevB.22.3173.
- [13] S. S. Saxena et al. ‘Superconductivity on the Border of Itinerant-Electron Ferromagnetism in UGe2’. In: *Nature* 406.6796 (Aug. 2000), pp. 587–592. ISSN: 0028-0836, 1476-4687. DOI: 10.1038/35020500.
- [14] Dai Aoki et al. ‘Coexistence of Superconductivity and Ferromagnetism in URhGe’. In: *Nature* 413.6856 (Oct. 2001), pp. 613–616. ISSN: 0028-0836, 1476-4687. DOI: 10.1038/35098048.
- [15] Dai Aoki et al. ‘Spin-Triplet Superconductivity in UTe₂ and Ferromagnetic Superconductors’. In: *Proceedings of the International Conference on Strongly Correlated Electron Systems (SCES2019)*. Okayama, Japan: Journal of the Physical Society of Japan, Mar. 2020. ISBN: 978-4-89027-142-9. DOI: 10.7566/JPSCP.30.011065.
- [16] Masatoshi Sato and Satoshi Fujimoto. ‘Majorana Fermions and Topology in Superconductors’. In: *Journal of the Physical Society of Japan* 85.7 (July 2016), p. 072001. ISSN: 0031-9015, 1347-4073. DOI: 10.7566/JPSJ.85.072001.
- [17] A. Y. Kitaev. ‘Unpaired Majorana Fermions in Quantum Wires’. In: *Physics-Uspekhi* 44.10S (Oct. 2001), pp. 131–136. ISSN: 1468-4780. DOI: 10.1070/1063-7869/44/10S/S29.

-
- [18] Y Tada, N Kawakami and S Fujimoto. ‘Pairing State at an Interface of Sr_2RuO_4 : Parity-Mixing, Restored Time-Reversal Symmetry and Topological Superconductivity’. In: *New Journal of Physics* 11.5 (May 2009), p. 055070. ISSN: 1367-2630. DOI: 10.1088/1367-2630/11/5/055070.
 - [19] Andrew Peter Mackenzie and Yoshiteru Maeno. ‘The Superconductivity of Sr_2RuO_4 and the Physics of Spin-Triplet Pairing’. In: *Reviews of Modern Physics* 75.2 (May 2003), pp. 657–712. ISSN: 0034-6861, 1539-0756. DOI: 10.1103/RevModPhys.75.657.
 - [20] Yoshiteru Maeno et al. ‘Evaluation of Spin-Triplet Superconductivity in Sr_2RuO_4 ’. In: *Journal of the Physical Society of Japan* 81.1 (Jan. 2012), p. 011009. ISSN: 0031-9015, 1347-4073. DOI: 10.1143/JPSJ.81.011009.
 - [21] Karen Michaeli and Liang Fu. ‘Spin-Orbit Locking as a Protection Mechanism of the Odd-Parity Superconducting State against Disorder’. In: *Physical Review Letters* 109.18 (Oct. 2012), p. 187003. ISSN: 0031-9007, 1079-7114. DOI: 10.1103/PhysRevLett.109.187003.
 - [22] A. A. Abrikosov and L. P. Gor’kov. ‘Contribution to the Theory of Superconducting Alloys with Paramagnetic Impurities’. In: *Zhur. Eksptl. i Teoret. Fiz.* Vol: 39 (Nov. 1960). URL: <https://www.osti.gov/biblio/4097498>.
 - [23] M. A. Ruderman and C. Kittel. ‘Indirect Exchange Coupling of Nuclear Magnetic Moments by Conduction Electrons’. In: *Physical Review* 96.1 (Oct. 1954), pp. 99–102. ISSN: 0031-899X. DOI: 10.1103/PhysRev.96.99.
 - [24] Tadao Kasuya. ‘A Theory of Metallic Ferro- and Antiferromagnetism on Zener’s Model’. In: *Progress of Theoretical Physics* 16.1 (July 1956), pp. 45–57. ISSN: 0033-068X. DOI: 10.1143/PTP.16.45.
 - [25] Kei Yosida. ‘Magnetic Properties of Cu-Mn Alloys’. In: *Physical Review* 106.5 (June 1957), pp. 893–898. ISSN: 0031-899X. DOI: 10.1103/PhysRev.106.893.
 - [26] Felix Küster et al. ‘Long Range and Highly Tunable Interaction between Local Spins Coupled to a Superconducting Condensate’. In: *Nature Communications* 12.1 (Nov. 2021), p. 6722. ISSN: 2041-1723. DOI: 10.1038/s41467-021-26802-x.
 - [27] Jaber Ali Ouassou, Takehito Yokoyama and Jacob Linder. ‘RKKY Interaction in Triplet Superconductors: Dzyaloshinskii-Moriya-type Interaction Mediated by Spin-Polarized Cooper Pairs’. In: *Physical Review B* 109.17 (May 2024), p. 174506. ISSN: 2469-9950, 2469-9969. DOI: 10.1103/PhysRevB.109.174506.
 - [28] A. F. Andreev. ‘Thermal Conductivity of the Intermediate State of Superconductors’. In: *Zh. Eksperim. i Teor. Fiz.* Vol: 46 (May 1964). URL: <https://www.osti.gov/biblio/4071988>.
 - [29] B.D. Josephson. ‘Possible New Effects in Superconductive Tunnelling’. In: *Physics Letters* 1.7 (July 1962), pp. 251–253. ISSN: 00319163. DOI: 10.1016/0031-9163(62)91369-0.
 - [30] P. W. Anderson and J. M. Rowell. ‘Probable Observation of the Josephson Superconducting Tunneling Effect’. In: *Physical Review Letters* 10.6 (Mar. 1963), pp. 230–232. ISSN: 0031-9007. DOI: 10.1103/PhysRevLett.10.230.
 - [31] A. A. Golubov, M. Yu. Kupriyanov and E. Il’ichev. ‘The Current-Phase Relation in Josephson Junctions’. In: *Reviews of Modern Physics* 76.2 (Apr. 2004), pp. 411–469. ISSN: 0034-6861, 1539-0756. DOI: 10.1103/RevModPhys.76.411.
 - [32] Matthias Eschrig. ‘Spin-Polarized Supercurrents for Spintronics’. In: *Physics Today* 64.1 (Jan. 2011), pp. 43–49. ISSN: 0031-9228, 1945-0699. DOI: 10.1063/1.3541944.
 - [33] Mary Eileen Farrell and Marilyn F. Bishop. ‘Proximity-Induced Superconducting Transition Temperature’. In: *Physical Review B* 40.16 (Dec. 1989), pp. 10786–10795. ISSN: 0163-1829. DOI: 10.1103/PhysRevB.40.10786.
 - [34] Guojing Hu et al. ‘Long-Range Skin Josephson Supercurrent across a van Der Waals Ferromagnet’. In: *Nature Communications* 14.1 (Mar. 2023), p. 1779. ISSN: 2041-1723. DOI: 10.1038/s41467-023-37603-9.
 - [35] Yao Junxiang et al. ‘Triplet Supercurrents in Lateral Josephson Junctions with a Half-Metallic Ferromagnet’. In: *Physical Review Research* 6.4 (Nov. 2024), p. 043114. ISSN: 2643-1564. DOI: 10.1103/PhysRevResearch.6.043114.
-

-
- [36] Linde A. B. Olde Olthof et al. ‘Controllable Enhancement of p -Wave Superconductivity via Magnetic Coupling to a Conventional Superconductor’. In: *Physical Review Letters* 127.26 (Dec. 2021), p. 267001. ISSN: 0031-9007, 1079-7114. DOI: 10.1103/PhysRevLett.127.267001.
 - [37] E.W. Fenton. ‘Absence of Proximity Effect between s-Wave and p-Wave Superconductors’. In: *Solid State Communications* 34.12 (June 1980), pp. 917–922. ISSN: 00381098. DOI: 10.1016/0038-1098(80)91098-4.
 - [38] P. M. R. Brydon et al. ‘Charge and Spin Supercurrents in Triplet Superconductor - Ferromagnet - Singlet Superconductor Josephson Junctions’. In: *Physical Review B* 88.5 (Aug. 2013), p. 054509. ISSN: 1098-0121, 1550-235X. DOI: 10.1103/PhysRevB.88.054509.
 - [39] Yasuhiro Asano et al. ‘Josephson Current in s -Wave-Superconductor/ Sr 2 RuO 4 Junctions’. In: *Physical Review B* 67.18 (May 2003), p. 184505. ISSN: 0163-1829, 1095-3795. DOI: 10.1103/PhysRevB.67.184505.
 - [40] Alexander Altland and Ben Simons. ‘Second Quantization’. In: *Condensed Matter Field Theory*. Second edition. Leiden: Cambridge University Press, 2010, pp. 39–83. ISBN: 978-0-511-78928-1 978-0-511-78782-9 978-0-511-78668-6 978-0-511-78998-4.
 - [41] Alexander Altland and Ben Simons. ‘Broken Symmetry and Collective Phenomena’. In: *Condensed Matter Field Theory*. Second edition. Leiden: Cambridge University Press, 2010, pp. 242–331. ISBN: 978-0-511-78928-1 978-0-511-78782-9 978-0-511-78668-6 978-0-511-78998-4.
 - [42] Jibir Ali Ouassou. ‘Bogoliubov–de Gennes Equations’. 2021. URL: <https://jabirali.github.io/notes/bdg-equations.pdf>.
 - [43] John Ove Fjærestad. *Tight-Binding Model for Electrons in a Crystal*. 2016. URL: <https://johnof.folk.ntnu.no/tight-binding-2016.pdf>.
 - [44] Jian-Xin Zhu. ‘2. BdG Equations in Tight-Binding Model’. In: *Bogoliubov-de Gennes Method and Its Applications*. Vol. 924. Lecture Notes in Physics. Springer International Publishing, 2016, pp. 37–64. ISBN: 978-3-319-31312-2 978-3-319-31314-6. DOI: 10.1007/978-3-319-31314-6.
 - [45] Mehran Kardar. ‘4. Classical Statistical Mechanics’. In: *Statistical Physics of Particles*. First published, 7th printing. Cambridge: Cambridge University Press, 2015, pp. 98–120. ISBN: 978-0-521-87342-0.
 - [46] Mehran Kardar. ‘7. Ideal Quantum Gases’. In: *Statistical Physics of Particles*. First published, 7th printing. Cambridge: Cambridge University Press, 2015, pp. 181–202. ISBN: 978-0-521-87342-0.
 - [47] Atousa Ghanbari, Vetle K. Risinggård and Jacob Linder. ‘Self-Consistent Solution for the Magnetic Exchange Interaction Mediated by a Superconductor’. In: *Scientific Reports* 11.1 (Mar. 2021), p. 5028. ISSN: 2045-2322. DOI: 10.1038/s41598-021-83620-3.
 - [48] John Hubbard. ‘Electron Correlations in Narrow Energy Bands’. In: *Proceedings of the Royal Society of London. Series A. Mathematical and Physical Sciences* 276.1365 (Nov. 1963), pp. 238–257. ISSN: 0080-4630, 2053-9169. DOI: 10.1098/rspa.1963.0204.
 - [49] Xin-Zhong Yan. ‘Theory of the Extended Hubbard Model at Half Filling’. In: *Physical Review B* 48.10 (Sept. 1993), pp. 7140–7147. ISSN: 0163-1829, 1095-3795. DOI: 10.1103/PhysRevB.48.7140.
 - [50] Y. Zhang and J. Callaway. ‘Extended Hubbard Model in Two Dimensions’. In: *Physical Review B* 39.13 (May 1989), pp. 9397–9404. ISSN: 0163-1829. DOI: 10.1103/PhysRevB.39.9397.
 - [51] Jonathan Keeling. *Quantum Magnetism*. URL: <https://www.st-andrews.ac.uk/~jmjk/keeling/teaching/magnetism-notes.pdf>.
 - [52] Daniel P. Arovas et al. ‘The Hubbard Model’. In: *Annual Review of Condensed Matter Physics* 13.1 (Mar. 2022), pp. 239–274. ISSN: 1947-5454, 1947-5462. DOI: 10.1146/annurev-conmatphys-031620-102024.
 - [53] Wolfgang Nolting and Anupuru Ramakanth. ‘Exchange Interaction’. In: *Quantum Theory of Magnetism*. Ed. by Wolfgang Nolting and Anupuru Ramakanth. Berlin, Heidelberg: Springer, 2009, pp. 175–231. ISBN: 978-3-540-85416-6. DOI: 10.1007/978-3-540-85416-6_5.
-

-
- [54] Baptiste Savoie. ‘A Rigorous Proof of the Bohr–van Leeuwen Theorem in the Semiclassical Limit’. In: *Reviews in Mathematical Physics* 27.08 (Sept. 2015), p. 1550019. ISSN: 0129-055X, 1793-6659. DOI: 10.1142/S0129055X15500191.
- [55] Jabir Ali Ouassou. ‘Full Proximity Effect in Spin-Textured Superconductor—Ferromagnet Bilayers’. NTNU, 2015. URL: <https://pvv.ntnu.no/~jabirali/academic/project.pdf>.
- [56] Andreas Halkjelsvik Mjøs. ‘Spontaneous Vortex Phase and Quantum Phase Diagram of Ferromagnetic Superconductors’. NTNU. URL: <https://ntnopen.ntnu.no/ntnu-xmlui/handle/11250/2785526>.
- [57] Konstantin B. Efetov et al. ‘Proximity Effects in Ferromagnet/Superconductor Heterostructures’. In: *Magnetic Heterostructures: Advances and Perspectives in Spinstructures and Spintransport*. Ed. by Hartmut Zabel and Samuel D. Bader. Berlin, Heidelberg: Springer, 2008, pp. 251–290. ISBN: 978-3-540-73462-8. DOI: 10.1007/978-3-540-73462-8-5.
- [58] John Ove Fjærrestad. *The Hubbard and Heisenberg Models, Spin-Wave Theory of Ferro- and Antiferromagnets, Broken Symmetry and Goldstone Modes*. 2016. URL: <https://johnof.folk.ntnu.no/magnetism-2016.pdf>.
- [59] Elliott H. Lieb and F. Y. Wu. ‘Absence of Mott Transition in an Exact Solution of the Short-Range, One-Band Model in One Dimension’. In: *Physical Review Letters* 20.25 (June 1968), pp. 1445–1448. ISSN: 0031-9007. DOI: 10.1103/PhysRevLett.20.1445.
- [60] Y Claveau, B Arnaud and S Di Matteo. ‘Mean-Field Solution of the Hubbard Model: The Magnetic Phase Diagram’. In: *European Journal of Physics* 35.3 (May 2014), p. 035023. ISSN: 0143-0807, 1361-6404. DOI: 10.1088/0143-0807/35/3/035023.
- [61] J. E. Hirsch. ‘Two-Dimensional Hubbard Model: Numerical Simulation Study’. In: *Physical Review B* 31.7 (Apr. 1985), pp. 4403–4419. ISSN: 0163-1829. DOI: 10.1103/PhysRevB.31.4403.
- [62] R. A. de Groot et al. ‘New Class of Materials: Half-Metallic Ferromagnets’. In: *Physical Review Letters* 50.25 (June 1983), pp. 2024–2027. ISSN: 0031-9007. DOI: 10.1103/PhysRevLett.50.2024.
- [63] Y. Ji et al. ‘Determination of the Spin Polarization of Half-Metallic CrO₂ by Point Contact Andreev Reflection’. In: *Physical Review Letters* 86.24 (June 2001), pp. 5585–5588. ISSN: 0031-9007, 1079-7114. DOI: 10.1103/PhysRevLett.86.5585.
- [64] G. H. Wannier. ‘Antiferromagnetism. The Triangular Ising Net’. In: *Physical Review* 79.2 (July 1950), pp. 357–364. ISSN: 0031-899X. DOI: 10.1103/PhysRev.79.357.
- [65] J Vannimeten and G Toulouse. ‘Theory of the Frustration Effect. II. Ising Spins on a Square Lattice’. In: *Journal of Physics C: Solid State Physics* 10.18 (Sept. 1977), pp. L537–L542. ISSN: 0022-3719. DOI: 10.1088/0022-3719/10/18/008.
- [66] C. Broholm et al. ‘Quantum Spin Liquids’. In: *Science* 367.6475 (Jan. 2020), eaay0668. ISSN: 0036-8075, 1095-9203. DOI: 10.1126/science.aay0668.
- [67] Leon Balents. ‘Spin Liquids in Frustrated Magnets’. In: *Nature* 464.7286 (Mar. 2010), pp. 199–208. ISSN: 0028-0836, 1476-4687. DOI: 10.1038/nature08917.
- [68] K. Binder and A. P. Young. ‘Spin Glasses: Experimental Facts, Theoretical Concepts, and Open Questions’. In: *Reviews of Modern Physics* 58.4 (Oct. 1986), pp. 801–976. ISSN: 0034-6861. DOI: 10.1103/RevModPhys.58.801.
- [69] Steven T. Bramwell and Michel J. P. Gingras. ‘Spin Ice State in Frustrated Magnetic Pyrochlore Materials’. In: *Science* 294.5546 (Nov. 2001), pp. 1495–1501. ISSN: 0036-8075, 1095-9203. DOI: 10.1126/science.1064761.
- [70] Kristian Fossheim and Asle Sudbø. ‘What Is Superconductivity? A Brief Overview. Fermi-liquids and Attractive Interactions. The Superconducting State – an Electronic Condensate’. In: *Superconductivity: Physics and Applications*. Chichester, GB: Wiley, 2004, pp. 1–27, 57–123. ISBN: 978-0-470-84452-6.
- [71] Vladimir P. Mineev and K. V. Samokhin. *Introduction to Unconventional Superconductivity*. Amsterdam, The Netherlands: Gordon and Breach Science Publishers, 1999. ISBN: 978-90-5699-209-5.

-
- [72] Manfred Sigrist and Kazuo Ueda. ‘Phenomenological Theory of Unconventional Superconductivity’. In: *Reviews of Modern Physics* 63.2 (Apr. 1991), pp. 239–311. ISSN: 0034-6861, 1539-0756. doi: 10.1103/RevModPhys.63.239.
- [73] Leon N. Cooper. ‘Bound Electron Pairs in a Degenerate Fermi Gas’. In: *Physical Review* 104.4 (Nov. 1956), pp. 1189–1190. ISSN: 0031-899X. doi: 10.1103/PhysRev.104.1189.
- [74] Damien Terrade. ‘Proximity Effects and Josephson Currents in Ferromagnet : Spin-Triplet Superconductors Junctions’. PhD thesis. 2015. doi: 10.18419/OPUS-6876.
- [75] Jian-Xin Zhu. ‘1. Bogoliubov-de Gennes Equations for Superconductors in the Continuum Model’. In: *Bogoliubov-de Gennes Method and Its Applications*. Vol. 924. Lecture Notes in Physics. Cham: Springer International Publishing, 2016, pp. 3–37. ISBN: 978-3-319-31312-2 978-3-319-31314-6. doi: 10.1007/978-3-319-31314-6.
- [76] Swagatam Nayak and Sanjeev Kumar. ‘Exotic Superconducting States in the Extended Attractive Hubbard Model’. In: *Journal of Physics: Condensed Matter* 30.13 (Apr. 2018), p. 135601. ISSN: 0953-8984, 1361-648X. doi: 10.1088/1361-648X/aaaefc.
- [77] Yang-Zhi Chou et al. ‘Correlation-Induced Triplet Pairing Superconductivity in Graphene-Based Moiré Systems’. In: *Physical Review Letters* 127.21 (Nov. 2021), p. 217001. ISSN: 0031-9007, 1079-7114. doi: 10.1103/PhysRevLett.127.217001.
- [78] Steven Allan Kivelson et al. ‘A Proposal for Reconciling Diverse Experiments on the Superconducting State in Sr₂RuO₄’. In: *npj Quantum Materials* 5.1 (June 2020), p. 43. ISSN: 2397-4648. doi: 10.1038/s41535-020-0245-1.
- [79] Jacob Linder and Alexander V. Balatsky. ‘Odd-Frequency Superconductivity’. In: *Reviews of Modern Physics* 91.4 (Dec. 2019), p. 045005. ISSN: 0034-6861, 1539-0756. doi: 10.1103/RevModPhys.91.045005.
- [80] V.L. Bezrezinskij. ‘New model of anisotropic phase of the superfluid He3’. In: *Pis’ma Zh. Ehksp. Teor. Fiz.* 20.9 (Nov. 1974), pp. 628–631.
- [81] Alex Aperis, Pablo Maldonado and Peter M. Oppeneer. ‘Ab Initio Theory of Magnetic-Field-Induced Odd-Frequency Two-Band Superconductivity in MgB₂’. In: *Physical Review B* 92.5 (Aug. 2015), p. 054516. ISSN: 1098-0121, 1550-235X. doi: 10.1103/PhysRevB.92.054516.
- [82] L. Komendová, A. V. Balatsky and A. M. Black-Schaffer. ‘Experimentally Observable Signatures of Odd-Frequency Pairing in Multiband Superconductors’. In: *Physical Review B* 92.9 (Sept. 2015), p. 094517. ISSN: 1098-0121, 1550-235X. doi: 10.1103/PhysRevB.92.094517.
- [83] Y. Tanaka, Y. Tanuma and A. A. Golubov. ‘Odd-Frequency Pairing in Normal-Metal/Superconductor Junctions’. In: *Physical Review B* 76.5 (Aug. 2007), p. 054522. ISSN: 1098-0121, 1550-235X. doi: 10.1103/PhysRevB.76.054522.
- [84] Christopher Triola and Alexander V. Balatsky. ‘Odd-Frequency Superconductivity in Driven Systems’. In: *Physical Review B* 94.9 (Sept. 2016), p. 094518. ISSN: 2469-9950, 2469-9969. doi: 10.1103/PhysRevB.94.094518.
- [85] Masashige Matsumoto and Manfred Sigrist. ‘Quasiparticle States near the Surface and the Domain Wall in a $p_x \pm ip_y$ -Wave Superconductor’. In: *Journal of the Physical Society of Japan* 68.9 (Sept. 1999), pp. 3120–3120. ISSN: 0031-9015, 1347-4073. doi: 10.1143/JPSJ.68.3120.
- [86] Kazuhiro Kuboki. ‘Proximity Effects near the Interface between d-Wave Superconductors and Ferro/Antiferromagnets’. In: *J. Phys. Soc. Jpn.* 284–288 (July 2000), pp. 505–506. ISSN: 09214526. doi: 10.1143/JPSJ.68.3150. arXiv: cond-mat/9906244.
- [87] Christopher J. Greenshields and Henry G. Weller. ‘5.6 Under-relaxation’. In: *Notes on Computational Fluid Dynamics: General Principles*. Reading, UK: CFD Direct Limited, 2022, p. 252. ISBN: 978-1-3999-2078-0.
- [88] Kazuhiro Kuboki. ‘Effect of Band Structure on the Symmetry of Superconducting States’. In: *Journal of the Physical Society of Japan* 70.9 (Sept. 2001), pp. 2698–2702. ISSN: 0031-9015, 1347-4073. doi: 10.1143/JPSJ.70.2698.
- [89] Finja Tietjen. ‘RKKY Interaction in Unconventional Superconductors’. NTNU, 2023. URL: <https://ntnuopen.ntnu.no/ntnu-xmlui/handle/11250/3078194?locale-attribute=no>.

-
- [90] Hiroshi Imamura, Patrick Bruno and Yasuhiro Utsumi. ‘Twisted Exchange Interaction between Localized Spins Embedded in a One- or Two-Dimensional Electron Gas with Rashba Spin-Orbit Coupling’. In: *Physical Review B* 69.12 (Mar. 2004), p. 121303. ISSN: 1098-0121, 1550-235X. doi: 10.1103/PhysRevB.69.121303.
 - [91] Tamás András Tóth. ‘Quadrupolar Ordering in Two-Dimensional Spin-One Systems’. PhD thesis. Lausanne, EPFL, 2011. doi: 10.5075/EPFL-THESIS-5037.
 - [92] Xiao-Gang Wen. ‘Choreographed Entanglement Dances: Topological States of Quantum Matter’. In: *Science* 363.6429 (Feb. 2019), eaal3099. ISSN: 0036-8075, 1095-9203. doi: 10.1126/science.aal3099.
 - [93] D. Sanchez-Manzano et al. ‘Long-Range Superconducting Proximity Effect in YBa₂Cu₃O₇/La_{0.7}Ca_{0.3}MnO₃ Weak-Link Arrays’. In: *Applied Physics Letters* 124.22 (2024), p. 222603. ISSN: 0003-6951, 1077-3118. doi: 10.1063/5.0189305.
 - [94] Leonid P. Rokhinson, Xinyu Liu and Jacek K. Furdyna. ‘The Fractional a.c. Josephson Effect in a Semiconductor-Superconductor Nanowire as a Signature of Majorana Particles’. In: *Nature Physics* 8.11 (Nov. 2012), pp. 795–799. ISSN: 1745-2473, 1745-2481. doi: 10.1038/nphys2429.
 - [95] Jian-Xin Zhu. ‘6. Transport Across Normal-Metal/Superconductor Junction’. In: *Bogoliubov-de Gennes Method and Its Applications*. Vol. 924. Lecture Notes in Physics. Cham: Springer International Publishing, 2016, pp. 141–166. ISBN: 978-3-319-31312-2 978-3-319-31314-6. doi: 10.1007/978-3-319-31314-6.
 - [96] Machiel Flokstra. ‘Proximity Effects in Superconducting Spin-Valve Structures’. PhD thesis. Leiden: Leiden University, 2010.
 - [97] Carsten Matthias Putzke. *Fermi Surface and Quantum Critical Phenomena in High - Temperature Superconductors*. Ed. by Carsten Matthias Putzke. Cham: Springer International Publishing, 2017. ISBN: 978-3-319-48646-8. doi: 10.1007/978-3-319-48646-8_2.
 - [98] T. M. Klapwijk. ‘Proximity Effect From an Andreev Perspective’. In: *Journal of Superconductivity* 17.5 (Oct. 2004), pp. 593–611. ISSN: 0896-1107, 1572-9605. doi: 10.1007/s10948-004-0773-0.
 - [99] E. A. Demler, G. B. Arnold and M. R. Beasley. ‘Superconducting Proximity Effects in Magnetic Metals’. In: *Physical Review B* 55.22 (June 1997), pp. 15174–15182. ISSN: 0163-1829, 1095-3795. doi: 10.1103/PhysRevB.55.15174.
 - [100] A. Bagrets, C. Lacroix and A. Vedyayev. ‘Theory of Proximity Effect in Superconductor/Ferromagnet Heterostructures’. In: *Physical Review B* 68.5 (Aug. 2003), p. 054532. ISSN: 0163-1829, 1095-3795. doi: 10.1103/PhysRevB.68.054532.
 - [101] F. S. Bergeret, A. F. Volkov and K. B. Efetov. ‘Long-Range Proximity Effects in Superconductor - Ferromagnet Structures’. In: *Physical Review Letters* 86.18 (Apr. 2001), pp. 4096–4099. ISSN: 0031-9007, 1079-7114. doi: 10.1103/PhysRevLett.86.4096.
 - [102] L. N. Bulaevskii, V. V. Kuzii and A. A. Sobyanin. ‘Superconducting system with weak coupling to the current in the ground state’. In: *JETP Lett.* 25.7 (1977), pp. 290–294. URL: http://jetpletters.ru/ps/1410/article_21163.pdf.
 - [103] Jaber Ali Ouassou. ‘Manipulating Superconductivity in Magnetic Nanostructures in and out of Equilibrium’. Doctoral Thesis. NTNU, 2019. ISBN: 9788232637195.
 - [104] Richard L. Burden, John Douglas Faires and Annette M. Burden. ‘2.1 The Bisection Algorithm’. In: *Numerical Analysis*. Tenth edition. Boston, MA: Cengage Learning, 2016. ISBN: 978-1-305-25366-7.